Diss. ETH No. 17965

MULTIPHASE FLOW IN MICROCHANNELS: HYDRODYNAMICS AND IMPLEMENTATION IN PROCESS ENGINEERING

A dissertation submitted to

ETH ZURICH

for the degree of

Doctor of Sciences

presented by

Donata Maria Fries
Dipl.-Ing.
(Dresden University of Technology)

born on March 10, 1981
in Dresden (Germany)

citizen of
Federal Republic of Germany

Accepted on the recommendation of

Prof. Dr., Dr. h.c. Philipp Rudolf von Rohr (ETH Zürich), examiner
Prof. Dr. Volker Hessel (Eindhoven University of Technology),
co-examiner

Zurich, 2008

© Donata Maria Fries, 2008

Nimm einen Ton aus einer Harmonie,
Nimm eine Farbe aus dem Regenbogen,
Und alles, was dir bleibt, ist nichts, solang
Das schöne All der Töne fehlt und Farben.

Friedrich Schiller

Danksagung

Die vorliegende Arbeit entstand während meiner Zeit als wissenschaftliche Mitarbeiterin am Institut für Verfahrenstechnik der Eidgenössischen Technischen Hochschule (ETH) Zürich zwischen Januar 2005 und August 2008. Finanziell unterstützt wurde sie von der Emil Barell Stiftung, Basel.

Meinem Doktorvater, Prof. Dr. Philipp Rudolf von Rohr, danke ich herzlich für das mir entgegengebrachte Vertrauen, sein Interesse an der Arbeit, die fachlichen, organisatorischen und motivierenden Ratschläge sowie für die Unterstützung zu einer selbstständigen Arbeitsweise.

Prof. Dr. Volker Hessel danke ich für die Übernahme des Koreferates, das dem Projekt entgegengebrachte Interesse sowie für seine hilfreichen und kritischen Fragen in den letzten Monaten.

Für die gute Zeit am Institut danke ich allen Institutsmitgliedern, besonders den aktuellen und ehemaligen Kollegen am LTR. Besonders erwähnen möchte ich Simon Kuhn und Carsten Wagner für ihre Unterstützung in Bezug auf eine kontinuierliche Illumination der Mikroreaktoren und Tobias Voitl für seine Anregungen und Hilfe bei der chemischen Analyse. Severin Wälchli und Franz Trachsel danke ich für die Diskussionen in- und außerhalb des Reinraums. Den aktuellen und zukünftigen ”micros” wünsche ich viel Freude, kreative Ideen und eine ruhige Hand.

Den Studenten Nina Laubacher, Andriu Bonnevie-Svendson, Robert Ernst und Tobias Muralt, die eine Semester- oder Bachelorarbeit unter meiner Betreuung schrieben, danke ich für ihr Engagement, ihre Fragen und Anregungen.

Ein besonderer Dank geht an Bruno Kramer und Peter Hoffmann für ihre

Hilfe bei allen mechanischen Fragen sowie an Silvia Christoffel und Silke Stubbe für die Unterstützung im administrativen und organisatorischen Bereich.

Dem Reinraumteam, insbesondere Stefan Blunier und Donat Scheiwiller, danke ich für die Unterstützung bezüglich der Reaktorfabrikation. Für die Einarbeitung in den SU-8 Prozess danke ich Gloria Romera Guereca. Andreas Schmid vom Institut für Energietechnik danke ich für die Unterstützung bei den Geschwindigkeitsmessungen mit der HighSpeed Camera.

Schließlich möchte ich allen, mit denen ich eine schöne Zeit in Zürich hatte, danken: Canto primo und dem Kirchenchor Herz-Jesu Oerlikon für die Musik; Agnes, Franz, Pädi und Tobi für ihre Versuche, mir das Skifahren näherzubringen; den akianern für viele schöne Stunden und allen, mit denen ich die Schönheiten der Schweizer Bergwelt erfahren durfte.

Meinen Eltern danke ich, dass sie mich das Staunen lehrten und mich stets ermutig(t)en, meinen Weg zu gehen.

Der größte Dank geht an meinen Mann Hans Thomsen Nikolaus: Danke, dass wir unsere Wege gemeinsam gehen.

Danke Спасибо Kiitos Thank You
GRAZIE Merci شُكراً Gratias

Zusammenfassung

In der vorliegenden Arbeit wird der Einfluss der Kanalgeometrie auf die Strömungsmechanik und den Stofftransport in Mikroreaktoren experimentell und theoretisch untersucht. Durch die Miniaturisierung der charakteristischen Abmessung in einem Rohrreaktor entsteht zum einen ein sehr großes Oberflächen-Volumen-Verhältnis, zum anderen dominieren Oberflächen- und Viskositätskräfte gegenüber Gravitations- und Trägheitskräften. Durch diese Besonderheiten sind Mikroreaktoren ein wichtiges Werkzeug in der Prozessintensivierung.

Diese Arbeit bietet hauptsächlich einen Beitrag zum Verständnis des komplexen Zusammenspiels zwischen Kanalgeometrie, ausgebildeter Strömung und erzieltem Stoffübergang. Es konnte gezeigt werden, dass für mehrphasige Mikroreaktoren der Stoffübergang und -transport durch die Strömung, welche wiederum von der Kanalgeometrie beeinflusst wird, intensiviert werden kann.

Die in dieser Arbeit verwendeten Mikroreaktoren hatten eine Kanalbreite von $w = 100...400\ \mu m$ und eine Kanalhöhe von $h = 120...360\ \mu m$. Die Länge des Mikrokanals variierte zwischen 30 mm und 2 m. Die Reaktoren bestanden aus PolyDiMethylSiloxan (PDMS)/Glas bzw. Silizium/Glas und wurden im Reinraum mittels photolithographischer Methoden gefertigt. Im Kanaldesign wurde die Einlassgeometrie, die Kanalführung und das Reaktorende inklusive Phasentrennung variiert. Als Modellreaktion diente die Absorption von CO_2 in eine basische Lösung und die Extraktion von Vanillin aus der wässrigen Phase.

Die experimentelle Untersuchung der Mehrphasenströmung erfolgte mittels optischer Messmethoden. Laserinduzierte Fluoreszenz wurde für die Charakterisierung der Strömungsregime und der Phasengrenzflächen genutzt. Das Geschwindigkeitsfeld in der flüssigen Phase wurde mittels μ-Particle-Image-Velocimetry bestimmt. Alle Messungen erfolgten in halber Kanalhöhe. Die Geschwindigkeitsprofile wurden zusätzlich numerisch ermittelt. Desweiteren wurde der Druckverlust über dem

gesamten Mikrokanal bestimmt. Die chemische Analyse der Produkte erfolgte durch die Messung des pH-Wertes (Absorption von CO_2), UV/Vis-Spektroskopie und GC/MS (Extraktion von Vanillin).
Die resultierende Strömung wird im Bereich der untersuchten Strömungsgeschwindigkeiten ($u = 1.1 \cdot 10^{-3}\ m/s ... 0.5\ m/s$) und Volumenstromverhältnisse ($V_1 : V_2 = 1 : 6 ... 1 : 1$) durch die Einlassgeometrie festgelegt. Während ein Y-förmiger Einlass bevorzugt Schichtenströmung bildet, kann durch eine T-förmige Injektion der dispersen Phase eine stabile Taylorströmung sowohl für gas-flüssig als auch für flüssig-flüssig Strömungen ausgebildet werden. Die resultierende Tropfengröße hängt nicht nur von den Geschwindigkeiten, sondern auch von der Kanalgeometrie ab: Wird die disperse Phase in Strömungsrichtung mit einem schmalen Einlass injiziert, erfolgt der Abriss relativ früh und es entstehen kleine Tropfen/Blasen. Große Gasblasen/Tropfen können durch Injektion entgegen der Strömungsrichtung erzeugt werden. In den Flüssigkeitssegmenten ist eine Erhöhung des Stofftransportes durch das Einfügen von Meandrierungen möglich. Dabei wird in der Kanalkrümmung der innere Wirbel in die äußere Hälfte gedrückt und leicht nach hinten verschoben. Der Wirbel in der äußeren Kanalhälfte wird geteilt und verschwindet bei hohen Geschwindigkeiten. Eine effektive Phasentrennung innerhalb des Mikroreaktors ist mit Hilfe von Kapillarkräften bzw. unterschiedlichen Benetzungseigenschaften möglich.
Eine Intensivierung des Stoffübergangs ist durch eine optimierte Strömung möglich. In Abhängigkeit der geforderten Durchsatzrate kann dies unterschiedliche Kanalgeometrien und Strömungsformen verlangen: Für kleine Durchsatzraten ($\approx 100\ \mu l/min$) ist die Schichtenströmung mit einer kleinen Kanalbreite ($< 200\ \mu m$) zu bevorzugen, da der Stofftransportwiderstand durch die kurzen Diffusionswege sehr klein wird. Zusätzlich kann die Trennung beider Phasen im Mikroreaktor realisiert werden. Für größere Durchsatzraten ist dieses Strömungsregime nicht optimal. Zum einen ist aufgrund des Druckverlustes der Kanalquerschnitt zu vergrößern, was zu einer signifikanten Erhöhung der Diffusionszeit führt, zum anderen ist die Phasentrennung bei hohen Geschwindigkeiten schwieriger. Eine Taylorströmung mit kleinen Tropfen ermöglicht bei hohen Durchsätzen sowohl eine große spezifische Austauschfläche als auch einen intensivierten Stofftransport. Der gesamte Stoffübergang kann im Fall einer Taylorströmung mit gekrümmten Kanälen durch eine beschleunigte Oberflächenerneuerung verbessert werden.

Abstract

In this thesis the influence of the channel geometry on hydrodynamic properties and on the mass transfer is investigated by experimental and numerical methods. Miniaturization of characteristic dimensions leads to a large surface-to-volume ratio. Surface and viscous forces dominate over gravitational and inertial forces. Due to these features microreactors are an important tool in process intensification.

This thesis mainly contributes to the understanding of the complex interplay between channel geometry, formed flow pattern and obtained mass transfer. For multiphase microfluidics we demonstrate the intensification of mass transfer and mass transport by optimizing the flow properties.

The microreactors had a channel width of $w = 100...400\ \mu m$ and a channel height of $h = 120...360\ \mu m$. The length of the microchannel was varied between 30 mm and 2 m. The reactors were made of PolyDiMethylSiloxane (PDMS)/glass and Si/glass respectively and were fabricated using photolithographic methods in the cleanroom. Inlet geometry, channel design and outlet geometry with phase separation were varied in the different experiments. As a model reaction the absorption of CO_2 into an alkaline solution as well as the extraction of vanillin from an aqueous solution were tested.

Experimental investigation of multiphase flow was carried out using optical methods. Laser Induced Fluorescence was applied to characterize the flow pattern and the interfacial area. The velocity field in the liquid phase was determined by μ-Particle-Image-Velocimetry. All measurements were performed at medium channel height. The velocity fields were identified numerically as well. Furthermore the pressure drop was determined over the complete microchannel. Chemical analysis was done using pH-analysis (in the case of CO_2-absorption), UV/Vis-spectroscopy and GC/MS (in the case of the vanillin extraction).

In the investigated velocity range ($u = 1.1 \cdot 10^{-3}\ m/s...0.5\ m/s$) and flow ratio ($V_1 : V_2 = 1 : 6...1 : 1$) the resulting flow pattern is influenced by the inlet geometry. While a Y-shaped design normally creates a stratified flow, a stable Taylor flow can be obtained by injecting the dispersed phase in a T-design. This applies gas-liquid and liquid-liquid flow. The resulting slug length depends not only on the velocities but also on the channel design: if the dispersed phase is injected in the main flow direction with a narrow inlet, small slugs/bubbles will be created. Large slugs/bubbles can be formed with the opposite injection direction. An enhancement of mass transfer within the liquid slugs by using meandering channels is feasible. Then the inner vortex in the bend moves to the outer half and is shifted back. The outer vortex is divided into two vortices and disappears at high velocities. An effective phase separation on the chip is possible by means of capillary forces and different wetting properties respectively. Changing fluid properties affect the hydrodynamic properties as well. This is most distinct for changes in surface tension and viscosity.

Optimized hydrodynamics favor an intensified mass transfer. Depending on the required flow rate different reactor designs are favored: For small flow rates ($\approx 100\ \mu l/min$) stratified flow at small channel width ($< 200\ \mu m$) may be preferred. Due to short diffusion paths the mass transfer resistance will be small. Additionally phase separation can be implemented on the chip easily. At higher flow rates this flow regime suffers from reduced mass transfer coefficients due to the increased cross section area and from poor phase separation. At higher flow rates, a large specific interfacial area and an intensified mass transfer is realized for Taylor flow with small slug lengths. The overall mass transfer in Taylor flow can be improved by meandering channels, providing fast surface renewal.

Contents

Danksagung I

Zusammenfassung III

Abstract V

Nomenclature XI

1 Introduction 1
- 1.1 Motivation for the presented work . . . 1
- 1.2 Thesis structure and objectives . . . 4

2 Theoretical Considerations and State of the Art 7
- 2.1 Introduction into microreactors . . . 7
  - 2.1.1 Benefits of microchannels . . . 7
  - 2.1.2 Dominating forces . . . 8
- 2.2 Multiphase flow . . . 10
  - 2.2.1 Flow pattern . . . 11
  - 2.2.2 Influence of pressure . . . 12
- 2.3 Taylor flow . . . 13
  - 2.3.1 Formation of Taylor bubbles . . . 13
  - 2.3.2 Gas bubble length . . . 15
  - 2.3.3 Liquid slug length . . . 15
  - 2.3.4 Film thickness in Taylor flow . . . 17
  - 2.3.5 Mixing in the liquid slugs . . . 18
  - 2.3.6 Pressure drop . . . 20
- 2.4 Mass transfer . . . 23

3 Experiments and Experimental Methods 27
3.1 Fabrication of the reactors 27
3.1.1 Channels made of PDMS 27
3.1.2 Channels made of silicon 30
3.2 Experimental setup 31
3.2.1 Used fluids 31
3.2.2 Flow scheme 31
3.3 Experimental methods and data analysis 33
3.3.1 Hydrodynamic characterization 33
3.3.2 Chemical analysis 38

4 Influence of Channel Design on Hydrodynamics 39
4.1 Impact on the inlet design 39
4.1.1 Specific experimental setup 39
4.1.2 Gas bubble length 40
4.1.3 Liquid slug length 45
4.1.4 Phase distribution and unit cell length 48
4.1.5 Pressure drop 50
4.2 Enhanced mixing by meandering channels 52
4.2.1 Specific reactor design 52
4.2.2 Mixing quality 53
4.2.3 Slug length 55
4.2.4 Pressure drop 57
4.2.5 Velocity profile 58
4.3 Phase separation on the chip 64
4.3.1 Capillary forces 64
4.3.2 Separation by different wetting properties 67
4.4 Summary 69

5 Influence of Fluid Properties on Hydrodynamics 73
5.1 Influence of the liquid viscosity 73
5.1.1 Specific experimental setup 73
5.1.2 Slug length 74
5.1.3 Bubble length 76
5.1.4 Pressure drop 79
5.1.5 Phase distribution 82
5.1.6 Velocities 83
5.2 Varying the gas density 85
5.2.1 Flow regimes 85

5.2.2 Gas bubble length 87
5.2.3 Slug length 89
5.2.4 Film thickness 90
5.2.5 Phase distribution 91
5.2.6 Bubble velocity 95
5.2.7 Pressure drop 95
5.3 Summary 96

6 Use of specified Flow Properties for intensified Mass Transfer 99
6.1 Absorption of CO_2 in alkaline solution 99
6.1.1 Specific literature review and fundamentals 100
6.1.2 Influence of flow pattern 102
6.1.3 Influence of mean residence time 103
6.2 Extraction of vanillin for different flow pattern 105
6.2.1 Specific literature review 105
6.2.2 Extraction solvent 107
6.2.3 Influence of flow pattern 108
6.2.4 High throughput extraction by bifurcation 114
6.2.5 Increased mass transfer by meandering channels . 116
6.3 Summary 119

7 Summary and Conclusions 123

8 Outlook 127
8.1 Hydrodynamic properties of Taylor flow 127
8.2 Hydrodynamic properties for packed bed 128
8.3 Multistage extraction 129

Bibliography 131

List of publications 143

Curriculum Vitae 145

Nomenclature

Roman Symbols

a	specific area	$\left[m^2/m^3\right]$
a	parameter in correlation	
A	area	$\left[m^2\right]$
A	parameter in correlation	
b	parameter in correlation	
B	parameter in correlation	
C	Lockhart-Martinelli factor	
c	concentration	$\left[kg/m^3,\, mol/m^3\right]$
$\bar{c}$	mean concentration	$\left[kg/m^3,\, mol/m^3\right]$
c	parameter in correlation	
d	diameter	$[m]$
d_h	hydraulic diameter	$[m]$
d_{Diff}	diffusion length	$[m]$
D	diffusion coefficient	$\left[m^2/s\right]$
D	distribution ratio	
E	extraction efficiency	
f	frequency	$[Hz]$
f	friction factor	
f	function of ()	
f	film thickness	$[m]$
g	gravitational constant	$\left[m/s^2\right]$
h	height	$[m]$
I	intensity	
j	superficial velocity	$[m/s]$
k	parameter in correlation	
k_L	overall mass transfer coefficient	$[m/s]$
k_La	volumetric mass transfer coefficient	$[1/s]$
$\dot{m}$	mass flux	$\left[kg/m^2s\right]$

L	length (flow properties)	$[m]$
l	length (construction)	$[m]$
l	parameter in correlation	
m	parameter in correlation	
n	number (of capillaries in separator)	
$\dot{n}$	molar flux	$[mol/s]$
n	parameter in correlation	
p	pressure	$[Pa]$
p_C	capillary pressure	$[Pa]$
p_L	Laplace pressure	$[Pa]$
P	permeability	$\left[m^2/sPa\right]$
q	parameter in correlation	
r	radius	$[m]$
r	parameter in correlation	
s	traveled distance	$[m]$
s	slip	
s	standard deviation	
s	parameter in correlation	
t	time	$[s]$
t_{Diff}	diffusion time	$[s]$
t_{Res}	residence time	$[s]$
u	intrinsic velocity	$[m/s]$
V	volume	$\left[m^3\right]$
$\dot{V}$	volumetric flow rate	$\left[m^3/s\right]$
w	width	$[m]$
W	parameter in correlation	
x	streamwise length coordinate	$[m]$
$\dot{x}$	mass transport fraction	
X	Lockhart-Martinelli parameter	

Greek Symbols

α	parameter in correlation	
α	(bend) angle	$[^\circ]$
β	parameter in correlation	
β	(inlet) angle	$[^\circ]$
γ	ratio of two characteristic lengths	

Δ	Difference between two values	
ε	volume fraction	$[-]$
ε^*	volume transport fraction	$[-]$
η	dynamic viscosity	$[Pas]$
λ	wavelength	$[m]$
ν	mass specific volume	$\left[m^3/kg\right]$
ρ	density	$\left[kg/m^3\right]$
σ	surface tension	$[N/m]$
τ	parameter in correlation	
Φ	Contact angle	$[^\circ]$
φ	inclination angle	$[^\circ]$
Ψ	two-phase multiplier	$[-]$

Dimensionless Numbers

Bo	Bond number	$\left[\frac{\Delta\rho g d_h^2}{\sigma}\right]$
Ca	Capillary number	$\left[\frac{\eta v}{\sigma}\right]$
Dn	Dean number	$\left[\sqrt{d_h/r}\right]$
Gz	Graetz number	$\left[\frac{L_R}{d_h Re Sc}\right]$
Pe	Peclet number	$\left[\frac{d_h u}{D}\right]$
Re	Reynolds number	$\left[\frac{\rho v d_h}{\eta}\right]$
Sc	Schmidt number	$\left[\frac{\eta}{\rho D}\right]$
Sh	Sherwood number	$\left[\frac{k_L d_h}{D}\right]$
We	Weber number	$\left[\frac{\rho u^2 d_h}{\sigma}\right]$

Abbreviations

CAD	Computer Aided Design
CCD	Charge Coupled Device
COV	Coefficient of Variation
DC	Direct Current
FOV	Field of view
GC	Gas Chromatograph
LIF	Laser Induced Fluorescence
LSM	Laser Scanning Microscopy
MS	Mass Spectroscopy
Nd:YAG	Neodynium: Yttrium Aluminium Garnet ($Y_3Al_5O_{12}$) Crystal
PDMS	Polydimethylsiloxane
PEEK	Polyetheretherketone
pH	potentia hydrogenii
PIV	Particle Image Velocimetry
PTFE	Polytetrafluorethylene
PTU	Precision Timing Unit
$\mu-$PIV	micro Particle Image Velocimetry
Si	Silicon
XTM	X-ray tomographic microscopy

Subscript and Superscript

acc	acceleration
aq	water
B	bubble
$bulk$	Bulk
C	capillary
eq	equilibrium
Exp	exposure
F	film
$fric$	friction
G	gaseous phase
$grav$	gravity
H	channel height (used as length scale)
i	compound

L	liquid phase
M	mixing
max	maximum
n	number of realizations
org	organic
R	reactor
S	slug
S	segregation
Sep	separator
tot	total
y	spanwise direction
1	first point
2	second point
2P	two phase

Chapter 1

Introduction

1.1 Motivation for the presented work

The use of microstructured devices in chemical engineering provides new ways. Miniaturization leads to an intensified mass- and heat transfer, enhanced process safety and increased production quality. Challenges are the fabrication of the channels, prevention from clogging, achievement of high mass flux rates, laminar flow and the interface to conventional production equipment. A rational implementation of microreactors for production and analytical application needs robust and multi-purpose microreactors. Intensive research for more than 10 years all over the world demonstrated the ability of microreactors for process intensification, chemical production and analysis.

Miniaturized components as micropumps (Shoji and Esashi; 1994), microgenerators (Williams and Yates; 1996) or even microrockets (Teasdale et al.; 2001) have been reported. Use of miniaturization for chemical purposes started in the 1990s, first application were reported few years later (Kreysa and DECHEMA; 1995; Lerou and Ng; 1996; Ehrfeld et al.; 1999; Haverkamp et al.; 1999).

Micro process engineering for conventional chemical processes will only be possible if cost effective fabrication techniques are applied. In the fine chemical industry microreactors allow intensified or even new processes. Hence microreactors are a valuable tool for specified application. In parallel with research on microreaction engineering, many suppliers of microsystems and platforms started business. Whereas industrial microreactors can be made out of metal or polymers, microreactors in research should preferentially provide an optical access to allow the characterization of the flow to investigate the flow properties and to perform in-situ measurements like Raman spectroscopy or UV/Vis-spectroscopy. Typical reactor materials for these research areas are glass, PDMS or PMMA.

Microreaction technologies are of great interest for industry and research in chemical engineering. The excellent heat and mass transfer properties, continuous operation mode, advanced reaction control and enhanced process safety enable microreactors as an efficient tool for the fine chemical industry and provide new possibilities in the performance of hazardous reactions (Jensen; 2001).

Lab on a chip

Since chemical engineers and chemists realized the advantages of microstructured devices, a ”Lab on a Chip”, combining all unit operations of one process in one microchip, is an ongoing vision. This includes conveying the fluids, mixing, reaction, separation and recycling. For more complex processes, these steps may be repeated in a multistage device.
Creating the flow in microstructures includes pressure driven flow (e.g. using a micropump) and electroosmotic flow. The latter requires high voltage, usually in the range of 1000 V/cm. Mixing in one phase flow is challenging due to the strong laminar profile. Different solutions as split-and-recombination units, hydrodynamic focusing, multilamination or chaotic advection were found (Hardt et al.; 2005; Nguyen and Wu; 2005; Schönfeld and Hardt; 2004; Hessel et al.; 2003).
Performance of reactions requires knowledge on the required residence time (Trachsel et al.; 2005), implementation of catalysts (Losey et al.; 2001), contacting principles for multiphase processes (Hessel et al.; 2005), mass transfer (Kreutzer, Kapteijn, Moulijn and Heiszwolf; 2005) and secondary flow characterization (Waelchli and Rudolf von Rohr; 2006).
Separation is still challenging: some solutions based on inertia were presented recently to separate particles from the liquid phase (Zhang et al.; 2006). For gas-liquid separation various designs based on the capillary forces were presented by Guenther, Jensen, Jhunjhunwala and Schmidt (2004); Gunther et al. (2005); Rebrov et al. (2007) whereas separation of liquid phases may be done by membranes (Kralj et al.; 2007) or by wetting properties (Kashid et al.; 2007).

Demands of chemical industry

Implementation of the well known and widely demonstrated advantages of microreaction engineering in production scale has been demonstrated by some companies (Benz et al.; 2001; Wille et al.; 2004; Roberge et al.;

2005; Kockmann; 2006; Brandner et al.; 2007). Nevertheless there are still some drawbacks as the robustness of reactors, the development costs and the reliability. It would be advantageous to create a reactor which can be used within a certain window of flow rates, fluid properties and reaction conditions. Problems like reliable distribution for internal numbering up, phase separation and clogging have to be solved.

Contributions of research

To realize these demands and to use microreactors effectively, fundamental knowledge of the processes and their intensification in the microscale is needed.

The falling film reactor for example which had been developed in the late 1990s at the IMM, demonstrates the interplay between research and industry: In cooperation with different research institutes the falling film microreactor was designed and optimized. Challenging research projects were e.g. the stable falling film, large interfacial areas, equal distribution of the phases and a narrow residence time distribution. The optimized falling film reactor demonstrated its ability for process intensification for different reactions. For the fluorination of toluene an increase of the space-time yield by a factor of 1000...5000 and an increase of the reactor efficiency by a factor of 2...8 compared to conventional bubble columns was reported (Jähnisch et al.; 2000). Expanding the application area for highly effective microreactors from liquid flow rates below 1 *ml/min* to higher throughput values is the focus of research activities as well. Strategies to increase the flow rate based on fundamental knowledge were recently presented for the falling film microreactor (Vankayala et al.; 2007).

More general, the dominant influence of the wall and of the wetting properties leads to specific phenomena, which are not known for conventional processes. Only a detailed and holistic characterization of processes (pressure drop, residence time, interfacial area or stability of flow) within microchannels allows a generalization. Therefore a specific research is the basis to find general solution for the challenges described above. This thesis contributes fundamentals on the interplay between channel design and fluid properties on flow characteristics and mass transfer for multiphase flow.

1.2 Thesis structure and objectives

In this study, we are interested in the major coherence between design parameters and fluid properties on hydrodynamic properties and the relation between hydrodynamics and mass transfer for both, gas-liquid and liquid-liquid processes. In other words, we want to figure out fundamental knowledge in terms of process engineering to provide precise tools for process intensification in the specific field of two-phase flow in microchannels. The detailed goals are the following:

- Description of gas-bubble breakup at different inlet geometries.
- Characterization of mixing in the liquid slug by meandering channels.
- Specification of the influence of liquid viscosity on gas-liquid two-phase flow.
- Depiction of gas-liquid two-phase flow at high pressure values.
- Demonstration of enhanced mass transfer in optimized microchannels.

This works starts with an overview of the state of the art: after a summary of the benefits of microreactors the differences of microsystems compared to conventional (batch) systems are discussed. An overview over fundamentals in multiphase flow with the focus on the most promising flow regime in microchannels regarding interfacial mass transfer, the Taylor flow, is given. An introduction on mass transfer mechanisms within one phase and across a phase boundary concludes chapter 2. Chapter 3 presents the experimental setup and measurement methods. Experimental results concerning the influence of the channel geometry (gas inlet, meandering structure) are given in chapter 4. In chapter 5 the influence of the liquid viscosity and gas density on hydrodynamic properties at an optimized channel design is discussed. The increase of mass transfer by miniaturizing and optimizing the flow properties is demonstrated in chapter 6. The results are finally summarized in chapter 7 and ideas for future work are discussed in chapter 8.

A scheme of this work is depicted in Fig. 1.1. Starting with designing new reactors and fabricating them (see chapter 3), the influence of the design (chapter 4) and fluid properties was investigated (chapter 5).

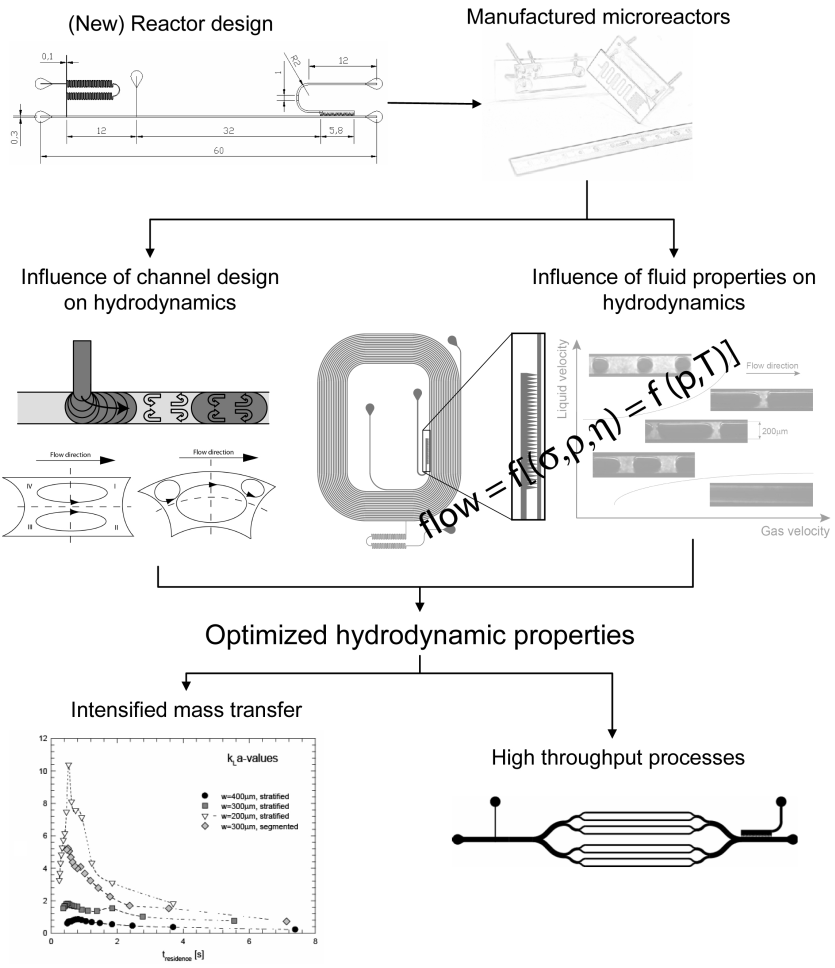
(New) Reactor design
0,1
R2
12
1
0,3
12
32
5,8
60
Manufactured microreactors
Influence of channel design on hydrodynamics
Influence of fluid properties on hydrodynamics
Flow direction
IV
I
III
II
Flow direction
flow = f[(σ,ρ,η) = f (p,T)]
Liquid velocity
Gas velocity
Flow direction
200μm
Optimized hydrodynamic properties
Intensified mass transfer
kLa-values
w=400μm, stratified
w=300μm, stratified
w=200μm, stratified
w=300μm, segmented
t residence [s]
0
2
4
6
8
10
12
High throughput processes

Figure 1.1: Scheme of this work

With this knowledge, enhancement of mass transfer for specific processes was demonstrated (chapter 6).

Chapter 2

Theoretical Considerations and State of the Art

2.1 Introduction into microreactors

Advances in the microfabrication enabled the precise manufacturing of microstructured devices for use in process engineering. In the field of chemical engineering these microstructured devices are the basis for microchannels or microreactors. In this work, the terms ”microchannel” and ”microreactor” will by used as synonyms for channels with cross section of $d_h < 1\ mm$, usually in the range of $d_h = 100...400\ \mu m$ and an arbitrary length.

2.1.1 Benefits of microchannels

Compared to conventional (batch)-reaction systems with larger sizes, microchannels provide different advantages which are mainly based on the decrease of length scales:

- *Enhanced surface-to-volume ratio:* Decreasing the characteristic length scale results consequently in an enhanced surface-to-volume ratio. Increasing the specific surface is one major parameter in increasing mass and heat transfer. Specific surfaces in the range of $a = 5'000...50'000\ m^2/m^3$ were reported for microchannels, whereas conventional production vessels are in the range of $a = 100\ m^2/m^3$. The enhanced heat transfer avoids hot spots at highly exothermic reactions. (Ehrfeld et al.; 2000)

- *Decreased diffusion paths:* According to Fick’s first law, which can be expressed as $t_{Diff}^2 \sim d_{Diff}/D$, molecular diffusion and heat exchange will be enhanced significantly by reduced channel sizes.

- *Small volumes:* Microreactors contain only few μl of chemicals, leading to an enhanced process safety. Additionally the residence times are usually very short. Narrow residence time distributions are feasible, which is advantageous in chemical engineering.
- *"Lab on a chip":* In microscale, sensors and actuators may be implemented directly on the chip allowing in-situ monitoring. Such sophisticated reactors may provide future analytical tools. (Jensen; 1999)
- *Numbering up:* Higher flow rates can be achieved by operating many devices in parallel. Problems of scaling up are therefore avoided. Nevertheless the precise distribution of the chemicals to the channels is still challenging.

Further advantages are the fast implementation of research results into production, smaller plants and production on site, flexible production according market demands and process intensification. Potential application of microchannels are beside the analytical industry the fine chemical industry and, due to the increased selectivity, reactors for highly exothermic and complex reactions.

2.1.2 Dominating forces

Reducing the dimensions has an impact on the dominating forces. In general, the interfacial forces get a more dominant influence compared to large scale applications. To compare the gravity, viscous and inertia forces with the interfacial force, dimensionless numbers will be used. The ratio of gravity to interfacial forces, the Bond number Bo is defined as:

$$Bo = \frac{\text{gravity}}{\text{interfacial forces}} = \frac{\Delta \rho g d_h^2}{\sigma} \tag{2.1}$$

Analytical solution showed that gravity has no effect on multiphase flow in capillaries for $Bo < 3.37$ (Bretherton; 1961). In microchannels, interfacial forces often dominate the gravitation ($Bo < 1$). This means, that for gas-liquid two-phase flow the flow pattern will be the same for a vertical and a horizontal channel alignment. Another important force in fluid

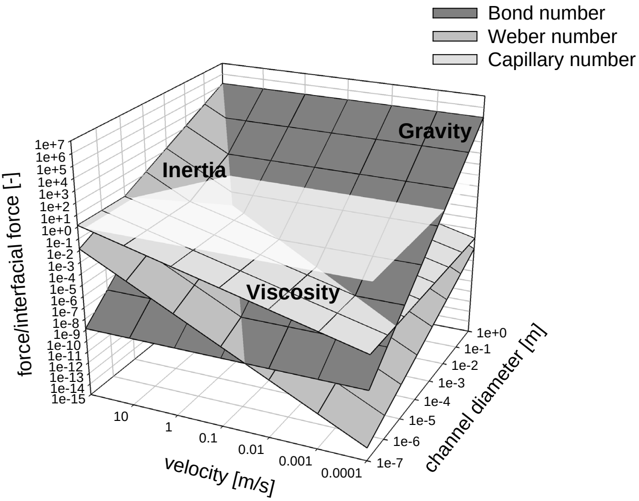

Figure 2.1: Influence on channel diameter and velocity on gravity, inertia and viscosity with respect to the surface tension. The transparent plane indicates parity.

mechanics is inertia. The ratio to interfacial forces is expressed by the Weber number We:

$$We_i = \frac{\text{inertia}}{\text{interfacial forces}} = \frac{\rho_i u_i^2 d_h}{\sigma} \tag{2.2}$$

In multiphase flow We can be calculated for each phase. Depending on the velocity, We in microchannels achieves values of $We < 1$. Finally the viscous forces are compared to the interfacial forces by the Capillary number Ca:

$$Ca = \frac{\text{viscous forces}}{\text{interfacial forces}} = \frac{\eta u}{\sigma} \tag{2.3}$$

This number is often used in multiphase microfluidics. In fluid mechanics, the ratio of viscous to inertial forces, expressed in the Reynolds number Re, is a common value:

$$Re_i = \frac{\text{inertia}}{\text{viscous forces}} = \frac{We}{Ca} = \frac{\rho_i u_i d_h}{\eta_i} \tag{2.4}$$

For microfluidic one- and multiphase flow $Re < 1000$ indicates a laminar flow profile. It should be noted that the transition to turbulence occurs at smaller Re than in large scale channels. The transition depends mainly on the wall properties (Hao et al.; 2006; Li, Tao, Li and Yu; 2006; Hao et al.; 2007). Since *Re* is often in the range from 1...100, inertia has an impact on the flow.
In Fig.2.1 *Ca*, *We*, and *Bo* are plotted versus the channel size and the velocity. The forces were calculated for water-nitrogen flow at 25°C and atmospheric pressure. Obviously the interfacial forces dominate the gravity, inertia and viscosity. This leads to special effects in multiphase flow. The properties of the wall (roughness, surface etc.) can not be neglected. Small changes in the wall will influence the flow properties significantly.

2.2 Multiphase flow

Multiphase flow is an important aspect in chemical engineering. Many reactions and processes take place in the presence of a gas phase: Hydrogenations, rectification, absorption... Beside the dimensionless numbers introduced above the following numbers are used in this work to characterize multiphase flow:
Volume fraction (holdup) of phase *i*:

$$\varepsilon_i = \frac{V_i}{\sum_{i=1}^{i=n} V_i} \tag{2.5}$$

Volume transport fraction (theoretical holdup):

$$\varepsilon_i^* = \frac{\dot{V}_i}{\sum_{i=1}^{i=n} \dot{V}_i} \tag{2.6}$$

Due to different intrinsic velocities of the phases, the volume fraction is not equal to the volume transport fraction. In two-phase flow, the ratio between both velocities is expressed by the phase slip:

$$s = \frac{u_1}{u_2} = \frac{\dot{V}_1 \varepsilon_2}{\dot{V}_2 \varepsilon_1} \tag{2.7}$$

The slip depends mainly on the flow pattern and, for Taylor flow, on the film thickness.

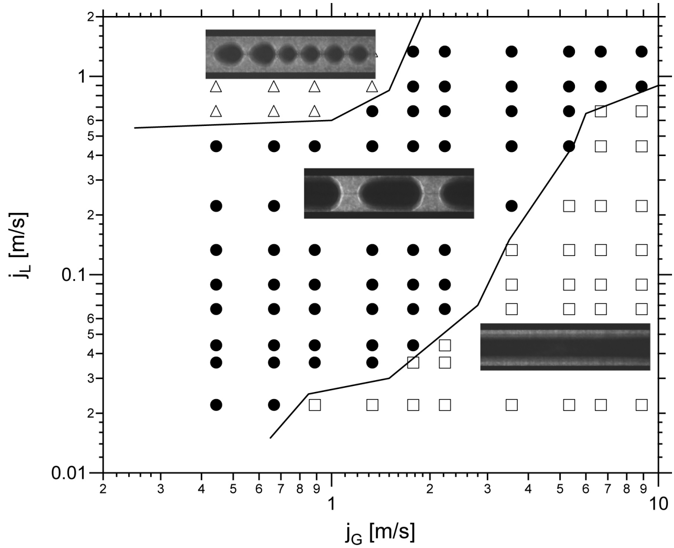

Figure 2.2: Exemplary flow pattern map for water-nitrogen in rectangular microchannels (Waelchli; 2005).

2.2.1 Flow pattern

In multiphase flow, different flow pattern have been observed. The resulting flow pattern depends on the superficial phase velocities, the wall properties, the cross section (shape and size), the inlet and the fluid properties. For gas-liquid two-phase flow in microchannels, mainly three different flow patterns were observed: the bubbly flow regime, the segmented flow regime and the annular flow regime (Waelchli; 2005; Haverkamp et al.; 2006). Additionally churn flow (de Mas et al.; 2003) and stratified flow (Coleman and Garimella; 1999) were reported for specific cases. The flow pattern vary in their phase distribution, pressure drop, interfacial area, slip and residence times. An exemplary flow pattern map for water-nitrogen flow is depicted in Fig.2.2.

The bubble flow regime was observed for low gas flow rates and high liquid flow rates. The liquid phase is the continuous one, interrupted by spherical bubbles with a diameter significantly smaller than the channel diameter. This flow pattern has a low gas holdup. The interfacial area achieves medium values. Usually this flow pattern can be found at the

channel end for gas-consuming processes.
At high gas flow rates and low liquid flow rates annular flow occurs. This flow pattern is characterized by two continuous phases: The gas core exists in the channel center and the liquid layer covers the wall. If the liquid does not wet the wall, this flow pattern might change to stratified flow. The intrinsic velocities of the phases differ significantly.
At a moderate ratio of the gas and liquid flow rate the Taylor flow regime was observed. In literature the terms segmented flow regime, intermittent flow regime or plug flow regime are used as synonyms for Taylor flow. The liquid phase is the continuous one, interrupted by gas bubbles filling nearly the complete cross section. The length of these bubbles is in the range of $L_B = 2...20\ d_h$. The liquid slugs have a length of $L_S \approx d_h$. A liquid film separates the bubbles from the wall. Within the liquid slugs, an axial symmetric recirculation was observed (Waelchli and Rudolf von Rohr; 2006).

2.2.2 Influence of pressure

To our knowledge, the influence of the pressure on these flow regimes had not been investigated as yet. Some investigations from the macroscale are interesting and may be adapted to microchannels. For trickle-bed-reactors, which are characterized by a cocurrent gas-liquid downflow across a packed bed, two major flow patterns are known: the trickle regime, characterized by thin liquid films and the pulsing regime, characterized by alternating liquid rich and gas rich zones ("pulses") which pass the bed. Also no direct comparison between these regimes and the flow patterns in a microchannel can be made, some considerations are interesting, because the trickle bed reactor can be considered as a randomly amount of many parallel microreactors. Wammes et al. (1990) investigated the transition of the trickle regime to the pulsing regime at elevated pressures (0.2...2.0 MPa) for water-nitrogen. At a constant gas flow rate and therefore at a constant superficial gas velocity, the transition between the trickle and the pulsing flow was found to shift towards higher liquid flow rates at elevated pressure.
(Guo and Al-Dahhan; 2004) investigated the liquid holdup and pressure drop for different pressure values between 0.8 MPa and 2.2 MPa in trickle bed reactors for small velocities. At increasing pressure, they observed a decrease of the liquid holdup and supposed as explanation a decrease in the film thickness due to higher drag force at the gas-liquid interphase.

2.3 Taylor flow

In microreactors, the so called Taylor flow is one of the most often used flow patterns. Important parameters influencing the mass transfer are the length of both, the gas bubbles (L_B) and the liquid slugs (L_S) as well as the thickness of the liquid film at the wall. A detailed review of the hydrodynamic properties and mass transfer characteristics of Taylor flow was given by Kreutzer, Kapteijn, Moulijn, Kleijn and Heiszwolf (2005). The most fascinating properties of Taylor flow in microchannels are the segmentation of the gas and the liquid phase, resulting in a narrow residence time distribution (Trachsel et al.; 2005), the film thickness between the gas bubble and the wall (Bretherton; 1961) and the recirculation inside the slugs (Taylor; 1961), providing efficient mixing in each liquid segment. This recirculation movement is symmetrical to the channel center line and depends on the liquid properties (Waelchli and Rudolf von Rohr; 2006) and on the liquid slug length (Kreutzer et al.; 2003).

2.3.1 Formation of Taylor bubbles

The defined formation of Taylor flow in microchannels is in the focus of recent research projects. Defined hydrodynamic properties are required for intensified processing. The break up mechanism was studied by Garstecki et al. (2006): Assuming a pressure balance of the continuous (liquid) and the discontinuous phase (gas) demonstrated a strong influence of the Laplace pressure

$$\Delta p_L = \sigma(\frac{1}{r_1} + \frac{1}{r_2}) \tag{2.8}$$

with r_1 equal to the half of the gas bubble height and r_2 the observed radius at the neck. A schematic overview is given in Fig.2.3. At the beginning, the liquid phase is flowing and no gas enters the main channel. The gas phase has to overcome the resistance of the gas-liquid interface and of the liquid flow resistance. Therefore, the pressure in the gas phase increases. At a certain threshold value, depending on the system pressure, the gas phase enters the main channel. First, it has a spherical form, but as soon as the diameter of the gas circle is close to the channel width, the gas bubble ”grows” towards the reactor outlet. During this procedure, the liquid phase cannot flow and is dammed, i.e. the liquid pressure increases. Due to this pressure, the elongated gas bubble will be

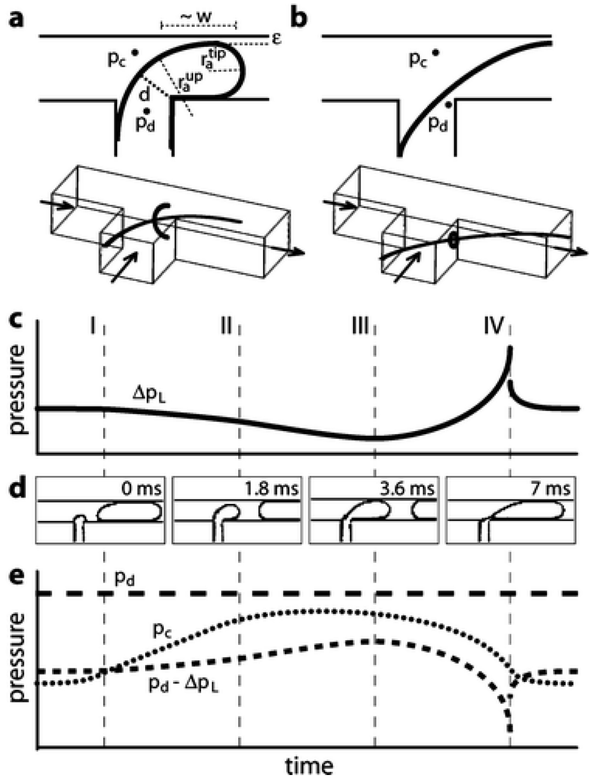
a
~ w
ε
p_c
r_a^{tip}
r_a^{up}
d
p_d
b
p_c
p_d
c
I
II
III
IV
pressure
Δp_L
d
0 ms
1.8 ms
3.6 ms
7 ms
e
p_d
pressure
p_c
$p_d - \Delta p_L$
time

Figure 2.3: Scheme of the growing bubble (a), the bubble breakup (b), the Laplace pressure versus the time (c), the bubble formation (d) and the pressure balance for the continuous phase p_c, the dispersed phase p_d and the Laplace pressure over the time (e) (Garstecki et al.; 2006).

shortened on the neck so that less gas flows. At a certain neck thickness (i.e. a maximum of the Laplace pressure), the gas flow is interrupted and the liquid flows again. This process is repeated continuously.
The formation of bubbles at the T-junction was characterized by μ-PIV-measurements by Xiong et al. (2007) and van Steijn et al. (2007). The results gave important information in understanding the bubble formation process. Crucial assumptions as the liquid blockage when the gas bubble sweeps the main channel could be verified in these papers. Kumar et al. (2007) investigated the formation of two-phase flow theoretically,

focused on the resulting gas bubble and liquid slug length. The inlet design was found to be a crucial parameter for resulting flow pattern and slug length values.

2.3.2 Gas bubble length

First work was done using capillaries in the miniscale. In the correlation of Laborie et al. (1999), see eq.2.9 in table 2.1, important physical parameters as the inertia forces, viscosity forces and gravity forces as well as the channel diameter play a significant role. The geometry of the gas inlet has not been considered. As in microscale the gravity can be neglected, eq.2.9 had to be modified. Zheng and Che (2006) observed in a circular vertical pipe that increasing the superficial gas velocity as well as decreasing the superficial liquid velocity results in an increased gas bubble length and a shorter liquid slug length. Garstecki et al. (2006) investigated the droplet length for liquid - liquid flow as well as for gas-liquid flow in microchannels depending on the flow rates. In this study the dependence of the breakup of the gas bubbles and thus of the gas bubble length via the pressure equilibrium was pronounced. As characteristic length they used the droplet length divided by the main channel width. Using a simple scaling law leads resulted in eq.2.10. This model did not fit for gas-liquid flow at higher gas flow rates ($\dot{V}_G > \dot{V}_L$), independent of the channel width. The scope of these correlations is given in table 2.1.

2.3.3 Liquid slug length

In this context the liquid slug length in microchannels is of special interest: Since a strong recirculation occurs in these slugs (Waelchli and Rudolf von Rohr; 2006; King et al.; 2007), short slugs are advantageous for a strong mass transfer and mixing. Furthermore, Bercic and Pintar (1997) demonstrated that short slugs result in a higher interfacial area, which is also advantageous for enhanced mass transfer. For capillaries, Laborie et al. (1999) found eq.2.11 in table 2.1 to fit the measured data best. Heiszwolf et al. (2001) correlated the dimensionless slug length L_S/d_h in a monolithic structure to the unit cell $(L_S + L_B)/d_h$ length via the liquid holdup ε_L, see eq.2.12. They observed a constant dimensionless liquid slug length of $L_S/d_h \approx 2$ for typical holdup values in the range of $\varepsilon_L = 0.2...0.5$. Based on the results, they obtained the correlation

Table 2.1: Correlations to describe the Taylor flow.

Reference	tube	correlation	comments
Correlations for the gas bubble length L_B:			
Laborie et al. (1999)	$d_h = 1...4\ mm$	$\frac{L_B}{d_h} = 0.0878 \left(\frac{Re_L(u_B)}{Bo^2} \right)^{0.63}$ (2.9)	water - nitrogen, $\varepsilon_G^* = 0.17...0.67$, $Re = 55...2000$
Garstecki et al. (2006)	$d_h = 40...90\ \mu m$	$\frac{L_B}{w} = 1 + \alpha \frac{\dot{V}_{disp}}{\dot{V}_{cont}}, \alpha \approx 1$ (2.10)	water - oil and water - nitrogen, $\frac{\dot{V}_{cont}}{\dot{V}_{disp}} = 0.02...10$
Correlations for the liquid slug length L_S:			
Laborie et al. (1999)	$d_h = 1...4\ mm$	$\frac{L_S}{d_h} = 3451 \left(\frac{1}{Re_L(j_G)\ Bo} \right)^{1.2688}$ (2.11)	water-nitrogen, $\varepsilon_G^* = 0.17...0.67$, $Re = 55...2000$
Heiszwolf et al. (2001)	$d_h = 1.56\ mm$	$\frac{L_S}{d_h} = \varepsilon_L \frac{L_S + L_B}{d_h}$ (2.12)	$\varepsilon_L = 0.08...0.98$, $u = 0.02...0.65\ m/s$
Kreutzer, Kapteijn, Moulijn, Kleijn and Heiszwolf (2005)	$d_h = 2.3\ mm$	$\frac{L_S}{d_h} = \frac{\varepsilon_L}{-0.00141 - 1.556\varepsilon_L^2 ln(\varepsilon_L)}$ (2.13)	
Liu et al. (2005)	$d_h = 0.9...3\ mm$	$L_S = \left[\frac{j_L + j_G}{0.088\ Re_G^{0.72}\ Re_L^{0.19}} \right]^2$ (2.14)	$Re = 10...1300$, $\varepsilon_L^* = 0.01...0.98$
Akbar and Ghiaasiaan (2006)		$\frac{(u_{2P})^{-1/3}}{\sqrt{L_S}} = 142.6\varepsilon_G^{0.56} \left(\frac{d_h}{L_S + L_B} \right) Re_G^{-0.252}$ (2.15)	numerical results

described in eq.2.13. The effect of the channel size for monolithic reactors has been investigated by Yawalkar et al. (2005), demonstrating that larger capillaries lead to elongated slugs. Tice et al. (2003) showed that in a rectangular microreactor for liquid-liquid two phase flow the unit cell length as well as the droplet length is independent from the total flow velocity but depends strongly on the flow rates of both phases. In their experiments, the droplet length fitted well with eq.2.12, using the volumetric transport ratio ε_L^*. They also found that mixing within the slug is faster for short slug lengths. Liu et al. (2005) pointed out that for given flow rates the resulting liquid slug length in a circular or rectangular capillary depends also on the inlet geometry. Eq.2.14 fitted the results for the specific nozzle geometry best. The volume of fluid method to predict the liquid slug length in circular capillaries was applied by Akbar and Ghiaasiaan (2006). The obtained correlation, see eq.2.15 in table 2.1 was compared the results with experimental data and gave good agreement.

Note that eq.2.14 and eq.2.12 require knowledge of the unit cell length $L_S + L_B$ to predict the slug length.

2.3.4 Film thickness in Taylor flow

The thickness of the liquid film had been investigated for capillaries filled with different media. Fairbrother and Stubbs (1935) investigated the bubble movement in a round capillary with a diameter of $d = 2.25\ mm$. The volume of the liquid, drained by a gas bubble with a length larger than 1.5 d, had been investigated. Together with the bubble length and some assumptions (gravity negligible, axisymmetrical shape of the bubble), they found the following empirical correlation:

$$f = \frac{d}{4}\sqrt{Ca} \tag{2.16}$$

Marchessault and Mason (1960) confirmed the dependence of the film thickness to $\sqrt{Ca}$ by conductivity measurements in a capillary with $d = 1.542\ mm$ and $d = 2.86\ mm$ respectively. They found the following empirical correlation:

$$f = \frac{D}{2}\sqrt{\frac{\eta}{\sigma}}\left[A + B\sqrt{Ca}\right] \tag{2.17}$$

whereas the parameters $A = -0.05$ and $B = 0.89$ depend on the experimental setup (reactor diameter, bubble length, used fluids). Bretherton

(1961) investigated theoretically and experimentally the pressure drop of a long gas bubble moving in a liquid filled round glass capillary with a diameter of $d = 1\ mm$. The gas bubble was found to move by factor W faster compared to the average velocity. Using the force balances and assuming a negligible gravity and inertia, W was calculated by:

$$W = 1.23\,(3Ca)^{2/3} \tag{2.18}$$

Further integration led to

$$f = 0.3215d\,(3Ca)^{2/3} \tag{2.19}$$

Experiments did not confirm this factor for very small Ca ($Ca < 10^{-5}$). Later investigations, as those of Wong et al. (1995) and Irandoust and Andersson (1989), confirmed the dependence of the Capillary number, whereas the exponent and the factor are still influenced by the used channel and the used fluids. These investigations had been performed under the following conditions:

- inertial forces are negligible $We < 1$ ($1 \gg \rho d u^2/\sigma$).
- No significant influence of gravity $Bo < 1$ ($1 \gg \rho d^2 g/\sigma$).

2.3.5 Mixing in the liquid slugs

Mixing in microreactors is of essential interest in process and chemical engineering. Since the flow is due to the small dimensions strictly laminar ($Re < 100$), mixing occurs mainly by diffusion. Therefore long mixing lengths and times are expected.

In the liquid slugs, a recirculating motion divides the slug into two halves. Strong mixing occurs within each of these halves but the mass transfer across the channel center line is limited to diffusion. The recirculation in slug flow had been proposed by Taylor (1961). Experimental validation for the miniscale ($d = 1...5\ mm$) at monolithic reactors was done by Thulasidas et al. (1997). The flow was found to be symmetric to the capillary center line. The radial center of these vortices and the recirculation time of the vortices were found to be important parameters for the mass transfer and axial mixing in and between these slugs. A characterization of the recirculation by numerical and experimental methods for liquid-liquid slug flow in microchannels was done by Kashid et al. (2005), where the experimental results confirmed the numerical data qualitatively. The

velocity of the flow was found to influence the position of the vortex center. King et al. (2007) pointed out, that the occurrence of recirculation depends on the slug length and on the velocity: at very low velocities, the shear force is too low to create a significant velocity gradient in the slugs. In the slug flow, the residence time distribution of the liquid phase is very narrow due to limited mass transfer between the slugs (Trachsel et al.; 2005). The flow pattern and flow characteristics for gas-liquid two-phase flow, focused on the segmented flow pattern in straight microchannels for different liquids, had been investigated by Waelchli and Rudolf von Rohr (2006). The recirculation is symmetrical to the channel center line. The vortex center of the counter rotating eddies was found to be close to the channel wall for both vortices. Confocal μ-PIV was demonstrated by Kinoshita et al. (2007) as a promising approach to overcome the 2-D limitation. First results indicated experimentally that the vortices in the slug are complex three-dimensional movements. These secondary recirculating movements within the laminar flow are able to enhance the mass transfer within the slug. Nevertheless they observed a significant symmetrical flow characteristic to the channel center line.
An application of defined recirculation is given in Matsuyama et al. (2007), where the Villermaux-Dushman reaction had been performed in the slug flow regime. Using different inlet designs, they compared slug flow where the slug is divided first into two radial shapes (left and right) and second into two axial halves (front and back). Faster mixing rates at constant Peclet numbers were observed for the axial arrangements, since the recirculation area has two different concentration fields. The corresponding simulation was presented by Tanthapanichakoon et al. (2006). Since experimental realization of the axial arrangement is hard to achieve, validation of the numerical results was done for only one case. Khan et al. (2004) used the recirculation and therefore the enhanced mass transfer and diminished axial distribution for the synthesis of colloidal silica particles.
Guenther, Khan, Thalmann, Trachsel and Jensen (2004) and Gunther et al. (2005) investigated the influence of channel bending on mixing of miscible liquids in gas-liquid segmented flow. For straight channels, they obtained a recirculation inside the liquid slug symmetrical to the channel center line. In a channel bend, this recirculation was observed to be a non-symmetric one. Inside the recirculating liquid elements, velocities normal to the channel wall of approximately 30% of the bulk liquid velocity were observed. Mixing experiments demonstrated a decreased

mixing length (ratio of the channel length to achieve a standard deviation of the intensity equal to 10% of the original value and the hydraulic diameter of the channel) of factor 5 by use of the meandering channels compared to a straight channel. They operated at low Capillary numbers of $Ca < 0.02$ and very low superficial velocities by the gaseous and the liquid phase. A more detailed study on the recirculation pattern in the bend was done by Waelchli (2005). In silicone-glass microreactors instantaneous velocity fields were obtained for different positions of the slug in the bend. The vortex movement across the channel center line led to the assumption of increased mass transfer by the bend.

The liquid slug length has a major impact on the mass transfer within the slugs. The Sherwood number Sh, characterizing the total mass transfer versus the mass transfer due to diffusion, increases by a factor of 1.5 with decreasing the dimensionless liquid slug length from 2 to 0.8. The following correlation was found by Kreutzer, Kapteijn, Moulijn and Heiszwolf (2005):

$$Sh \equiv \frac{k_L\, d}{D} = \sqrt{\alpha^2 + \frac{\beta}{Gz}} \tag{2.20}$$

with

$$\begin{aligned} \alpha &= 40\left(1 + 0.28\,(L_S/d)^{-4/3}\right) \\ \beta &= 90 + 104\,(L_S/d)^{-4/3} \\ Gz &= L_R/(d_h\; Re\; Sc) \end{aligned}$$

According to this correlation, Sh can be increased in the case of ethanol-nitrogen flow by a factor of 1.6 due to changes in the dimensionless slug length L_s/d from 2 to 0.5.

2.3.6 Pressure drop

The total pressure drop in gas-liquid flow consists of the pressure drop caused by the friction, pressure drop due to acceleration, caused by gravity and by the shape of the bubbles.

$$(\Delta p)_{tot} = (\Delta p)_{fric} + (\Delta p)_{acc} + (\Delta p)_{grav} + (\Delta p)_B \tag{2.21}$$

The pressure drop due to friction can be considered as the dominant part. The pressure drop caused by acceleration can be neglected for small pressure drop values. Friedel (1978) stated, that this is the case for $\frac{\Delta p}{p} < 0.2$. Otherwise the increase in the gas holdup and therefore in the volumetric flow rate due to the pressure drop will lead to an increase in the velocities. In this case the pressure drop due to acceleration has to be calculated by the separated flow model:

$$\Delta p_{acc} = \dot{m}^2 \left(\left[\frac{\dot{x}_G^2}{\rho_G \ \varepsilon_G} + \frac{\dot{x}_L^2}{\rho_L \ \varepsilon_L} \right]_{L=L_R} - \left[\frac{\dot{x}_G^2}{\rho_G \ \varepsilon_G} + \frac{\dot{x}_L^2}{\rho_L \ \varepsilon_L} \right]_{L=0} \right) \tag{2.22}$$

Δp_{acc} is the pressure drop due to acceleration, $\dot{m}$ is the mass flux, L_R is the reactor length, ε is the holdup, ρ the density and $\dot{x}$ stands for the mass transport fraction. The subscript G characterizes the gas phase, L denotes the liquid phase. The pressure drop due to gravity, $\left(\frac{\Delta p}{\Delta L}\right)_{Grav}$, defined by

$$\left(\frac{\Delta p}{\Delta L}\right)_{Grav} = (\varepsilon_G \rho_G + \varepsilon_L \rho_L) \ g \ sin\varphi \tag{2.23}$$

can be neglected in horizontal pipes, as the inclination angle φ will be 0. Additionally the gravitational pressure drop has no effect in microchannels, since the gravitational forces do not effect the flow pattern.

The pressure drop over a moving bubble due to the different shape of the bubble front and bubble tail, caused by surface tension effects, was found by (Bretherton; 1961) to be

$$\Delta p_B = 7.16 \ \frac{\sigma}{d} \ \sqrt[3]{9 \ Ca^2} \tag{2.24}$$

For Ca calculation, the total superficial velocity was used. The model had been validated experimentally in a circular glass tube with a length of 1 m and an inner diameter of $d_h = 1 \ mm$.

The frictional pressure drop can be calculated by:

$$\left(\frac{\Delta p}{L_R}\right)_{fric} = f \ \rho_L \ j^2 \ \frac{2}{d_h} \ \varepsilon_L \tag{2.25}$$

For one-phase flow, the holdup ε_L equals 1. In the case of two-phase flow, the velocity j is the sum of the superficial velocity of both phases. Different correlations for Taylor flow for the friction factor f can be found in literature. They are summarized in table 2.2. Since the liquid phase is the continuous one, the liquid fluid properties as well as the velocity of the slug has to be used.

Table 2.2: Correlations for the pressure drop in two-phase flow.

Reference	tube	correlation	comment
Friction factor f in the one-phase approach:			
one phase laminar flow	circular tube	$f = \frac{16}{Re}$ (2.26)	independent of wall roughness
Bretherton (1961)		$f = \frac{16}{Re}\left[1 + 0.465\,\frac{d_h}{L_S}\left(\frac{1}{Ca}\right)^{0.33}\right]$ (2.27)	analytical solution
Kreutzer, Kapteijn, Moulijn, Kleijn and Heiszwolf (2005)	$d_h = 2.3\ mm$	$f = \frac{16}{Re}\left[1 + 0.17\frac{d_h}{l_S}\left(\frac{Re}{Ca}\right)^{0.33}\right]$ (2.28)	numerical, validated with experiments in a circular capillary for $Re < 50$
Factor C in the Lockhart-Martinelli model:			
Chisholm (1967)	circular tube, $d_h = 0.001 ... 0.025\ m$	$C = 5$ (2.29)	both phases laminar
Mishima and Hibiki (1996)	circular tube, $d_h = 1 ... 4\ mm$	$C = 21\left[1 - e^{(-0.349 d_h)}\right]$ (2.30)	
Lee and Lee (2001)	circular tube, $d_h = 1 ... 4\ mm$	$C = A \cdot {\frac{\eta_L^2}{\rho_L \sigma d_h}}^{q}\ Ca^r Re_{Lo}^s$ (2.31)	modification of Mishima and Hibiki (1996)

In all these experiments, the observed bubble velocity was slightly increased compared to the superficial velocity, indicating a liquid film surrounding the gas bubble.
Lockhart and Martinelli (1949) proposed for conventional diameters, that the pressure drop of two phase flow will be correlated to the equivalent pressure drop in one phase flow by the two-phase multiplier Ψ^2:

$$\left(\frac{\Delta p}{L}\right)_{2P,fric} = \Psi_L^2 \left(\frac{\Delta p}{L}\right)_{L,fric} = \Psi_G^2 \left(\frac{\Delta p}{L}\right)_{G,fric} \tag{2.32}$$

Chisholm (1967) stated the dependence of Ψ^2 from the so called Lockhart-Martinelli-Parameter X and a factor C:

$$X = \sqrt{\frac{(\Delta p/L)_L}{(\Delta p/L)_G}} \tag{2.33}$$

$$\Psi_L^2 = 1 + \frac{C}{X} + \frac{1}{X^2} \ , \ \Psi_G^2 = 1 + CX + X^2 \tag{2.34}$$

In the past, various correlations for the factor C were proposed. They are summarized in the bottom part of table 2.2.

2.4 Mass transfer

In Taylor flow (see section 2.3), mass transfer consists of different steps which are illustrated for a heterogeneous catalysis (including mass transfer to the wall) in Fig.2.4. For molecules of the gas phase, 6 steps occur:

1. Mass transfer within the gas bubble,
2. Transport of the gas molecule from the gas bubble into the liquid slug over the circular interfacial area,
3. Transport of the gas molecule from the gas bubble into the liquid film close to the channel wall,
4. Transport of the gas molecule from the liquid slug into the liquid film close to the channel wall and
5. Transport from the liquid film to the channel wall

For the transport of the liquid phase molecules, the following steps exist:

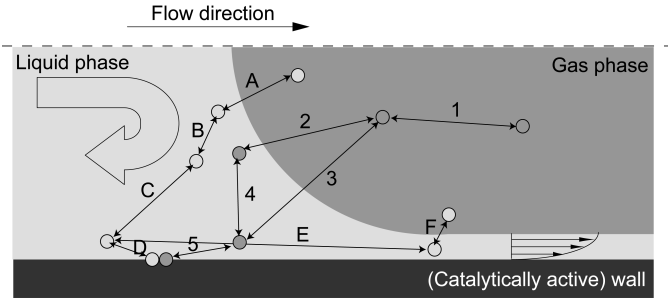

Figure 2.4: Detailed scheme of mass transfer mechanism in Taylor flow.

A. Mass transfer across the interfacial area from the liquid slug into the gas bubble,

B. Mass transfer within the liquid slug,

C. Transport from the liquid slug to the liquid film,

D. Transport from the liquid film to the channel wall,

E. Mass transfer within the liquid film and

F. Transport between the liquid film and the gas bubble

For the mass transfer over the liquid and the gas phase (2 and 4 for the gas molecules and A and F for the liquid molecules) the difference between the mass transfer bubble - slug and bubble - film is within the velocities and the interfacial area: The specific interfacial area is smaller for step 2 and A, but the surface renewing occurs faster. The transport mechanism for liquid material within the liquid phase (B, C and E) the difference lies within the velocity profile: Mass transfer within the slug is enhanced by the recirculation, whereas mass transfer within the film occurs at lower velocities in a parabolic profile. All steps may occur in both directions. Depending on the physical and chemical properties the mass transfer varies for the different steps. For liquid-liquid extraction and gas-liquid absorption (see chapter 6), the mass transport to the channel wall is not required. The dominating steps are those where the gas-liquid interface is crossed (in Fig.2.4 steps A, F, 2 and 3). These mass transfer steps are a combination of convective and diffusive mass

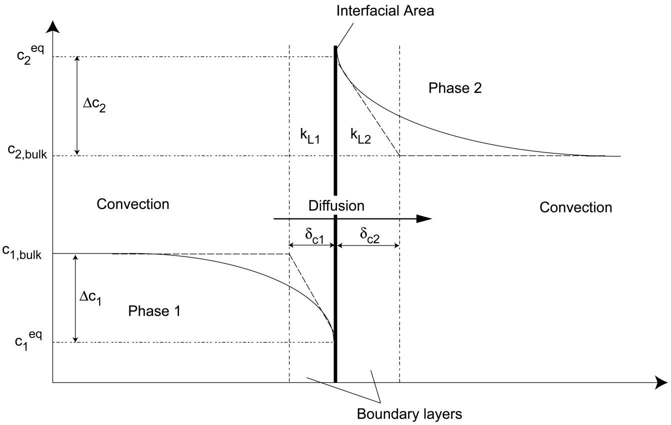
Interfacial Area
c_2^{eq}
Δc_2
$c_{2,bulk}$
Phase 2
k_{L1}
k_{L2}
Convection
Diffusion
Convection
δ_{c1}
δ_{c2}
$c_{1,bulk}$
Δc_1
Phase 1
c_1^{eq}
Boundary layers

Figure 2.5: Detailed scheme of mass transfer over interfacial area. Straight lines in concentration profile indicate the real profile, dotted lines are ideal modeled.

transfer. In the bulk of phase 1 the convective mass transfer is dominating. Close to the interfacial area are the boundary layers of both phases. In these layers mass transfer is mainly diffusion based. At the interfacial area equilibrium is assumed. In the boundary layers the concentration changes with increasing distance to the interfacial area to the concentration in the bulk. A schematic view is depicted in Fig.2.5. The mass transfer over the interfacial boundary can be described as follows:

$$\dot{n} = -k_{L1} \cdot A \cdot \left(c_1^{eq} - c_{1,bulk}\right) = -k_{L2} \cdot A \cdot \left(c_{2,bulk} - c_2^{eq}\right) \tag{2.35}$$

Based on these mass transfer coefficients for each phase, the overall mass transfer coefficent can be determined by

$$\frac{1}{k_L} = \frac{1}{k_{L1}} + \frac{1}{k_{L2}} \tag{2.36}$$

It is often important to know which amount is transported from one phase to another per volumetric unit and per time. The overall mass transfer coefficient is therefore multiplied with the specific interfacial area. The determination of the $k_L a$-value out of experimental values is described below:

To characterize the efficiency of the mass transfer, e.g. for an extraction, the ratio of the transferred material to the maximum amount which can be transferred is used:

$$E = \frac{c^{in} - c^{out}}{c^{eq} - c^{in}} \tag{2.37}$$

An extraction efficiency of $E = 1$ is identical with achieved equilibrium. The efficiency can be improved by increasing residence times and by optimized mass transfer due to increasing the interfacial area or enhanced transport mechanism. Kashid et al. (2007) demonstrated that for capillaries with decreasing diameter the efficiency increases at given velocities. The influence of the residence time had been pointed out in this study as well. The mass transfer coefficient strongly depends on the residence time and the interfacial area. Optimizing this parameter for a given system of fluids is the major challenge in process intensification. For a well defined interfacial area, the overall mass transfer coefficient can be calculated by:

$$k_L = \frac{1}{a \cdot t} ln \left(\frac{c^{eq} - c^{in}}{c^{eq} - c^{out}} \right) \tag{2.38}$$

If the equilibrium is not achieved, the mass transfer coefficient $k_L a$ increases with increasing residence times, indicating an increase in the efficiency. If equilibrium is achieved or if only marginal changes in efficiency can be detected, the $k_L a$-value decreases with increasing contact times. The maximum is an indicator for the optimal operation parameters.

Chapter 3

Experiments and Experimental Methods

3.1 Fabrication of the reactors

The microchannels used in this work were made of Polydimethylsiloxane (PDMS)-glass or of silicon-glass. For both channel types the design was defined via a CAD-programme (AutoCAD®). Based on this design, a photolithographic mask was printed on transparency (Grossensatz, resolution: 2400 *dpi*). The structure was manufactured in the cleanrooms at ETH.

3.1.1 Channels made of PDMS

Since the concept of soft lithography was introduced by McDonald et al. (2000), various research groups used the advantages of microstructures made of PDMS:

- fast and cheap prototyping
- easy manufacturing
- transparency.

PDMS's characteristics provide some properties, which might be a disadvantage for certain applications, e.g. swelling in contact with organic solvents (Lee et al.; 2003) and gas permeability (Merkel et al.; 2000). These are discussed in more detail on page 29. To create a mold of PDMS, a matrix of the structure is needed. In this work SU-8 layers on silicon wafers (one side polished, 100 mm in diameter, 525 μm thickness, SiMat) were used.

Manufacturing SU-8 structures

1. *Dehydration:* Since the used photoresist is very hydrophobic, a dehydration step is required to achieve a homogeneous layer of photoresist. To eliminate all traces of humidity, the wafer is placed on a hot plate at 200 °*C* for at least 30 *min*.

2. *Spin Coating:* The spin speed and spin time have major effect on the layer thickness and therefore on the channel depth. The wafer is placed centered on the spin coater. 4 *ml* of photoresist (SU8-50, MicroChem) were distributed at the wafer center. The spin coating was performed in two steps: first the photoresist was spread over the whole wafer at low spin speeds (15 *s*, 400 *rpm* with an acceleration of 200 *rpm*/*s*) whereas skidding was done in a second step at higher spin speeds thus adjusting layer thickness and homogeneity. To achieve homogenous thickness, multi-layer coating was executed. Obtained layer thicknesses for different layers, spin speeds and spin times are given in table 3.1. The acceleration of the second spin coating step was in every experiment 300 *rpm*/*s*.

Table 3.1: Measured SU-8 layer thickness at different spin coating parameters.

Number of layers [−]	spin speed [*rpm*]	spin time [*s*]	thickness [μm]	standard deviation [μm]
1	1000	30	120.4	±10.5
1	1250	30	95.8	±7.6
1	1500	30	68.5	±3.2
1	1750	30	57.2	±2.3
2	900	30	328.2	±22.3
2	1000	30	293.4	±19.2
2	1250	30	221.4	±15.3
2	1500	30	180.2	±10.8
2	900	50	250.3	±12.8
2	1500	50	140.8	±4.5

3. *Drying:* To diminish surface tension forced thickening at the wafer boundary, the wafer was placed for 10 *min* at a leveled plate.

4. *Pre-exposure bake:* Solvent evaporation and film densification is

achieved by heating the coated wafer on a leveled hot plate for 80 *min* at 100 °*C*. To avoid thermal stresses, the initial temperature is set to 30 °*C* and was slightly increased.

5. *Exposure:* All wafers were exposed with a masc aligner (Karl Süss, MA6). Exposure time was calculated based on the estimated thickness and the lamp intensity. To avoid heating of the photoresist layer, multiexposure with 10 *s* of exposure and 10 *s* of waiting time was applied.

6. *Post-exposure bake:* Selective cross linking of the exposed photoresist occurs while the exposed wafer is heated at 95 °*C* for 45 *min*. A two step heating, starting at 65 °*C*, is required to minimize thermal stress, resist cracking and wafer bowing.

7. *Developing:* The unexposed photoresist was dissolved in the developer.

8. *Hard baking:* To increase the mechanical stability, the wafer was heated to 150 °*C* and left there for 5 *min*. This process step was not mandatory.

PDMS-channels

The patterned silicon wafer was used as matrix for the PDMS channels. PDMS (Sylgard 184) compounds A and B were mixed in a ratio of 10:1 and degassed. To protect the SU-8 layer a thin film of silane (Trichloro(1H,1H,2H,2H-perfluorooctyl)silane, 97%, Aldrich) was evaporated. The liquid PDMS was molded over the wafer. After curing (70 °*C* for 4 *h*) the cross-linked PDMS was peeled off, cut into the predrawn reactor pieces, and the inlet/outlet holes were punched. After cleaning the surfaces were exposed to an oxygen plasma (Harrick Plasma) for 45 *s*. Bringing the activated surfaces in contact led to an irreversible bond between the PDMS and the glass. Cleaned PEEK-tubings (Upchurch) were placed into the holes and fixed with epoxy glue (Devcon, 5 Minute fast drying Epoxy). A scheme of these manufacturing steps is given in Fig.3.1 (McDonald et al.; 2000).

As mentioned above, PDMS can be used as a membrane for gases and swells in contact with organic solvents. The gas phase may penetrate through the PDMS at the gas inlet. For Taylor flow, the liquid film

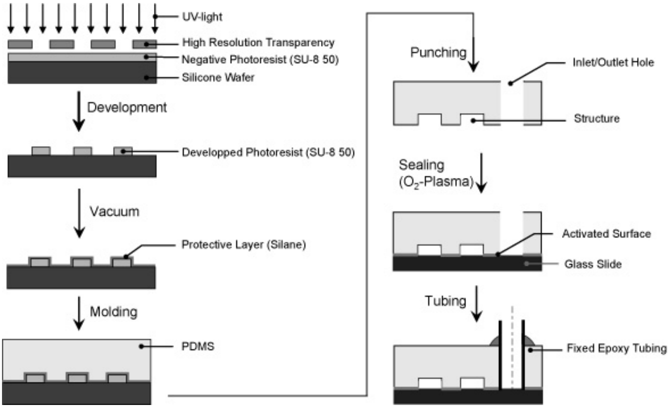
UV-light
High Resolution Transparency
Negative Photoresist (SU-8 50)
Silicone Wafer
Development
Developped Photoresist (SU-8 50)
Vacuum
Protective Layer (Silane)
Molding
PDMS
Punching
Inlet/Outlet Hole
Structure
Sealing
(O2-Plasma)
Activated Surface
Glass Slide
Tubing
Fixed Epoxy Tubing

Figure 3.1: Scheme of manufacturing microchannels made of PDMS.

which covers the wall acts as penetration barrier. As soon as the multiphase flow is established, the liquid film acts as diffusion barrier. The gas volume penetrating through the PDMS can be calculated by

$$V_G^{PDMS} = P_G \frac{A \cdot t \cdot \Delta p}{h_{PDMS}} \tag{3.1}$$

The permeability had been determined experimentally by Merkel et al. (2000) with $P_{N_2} = 3 \cdot 10^{-13}\ \frac{m^2}{s\ Pa}$ and $P_{CO_2} = 2.8 \cdot 10^{-12}\ \frac{m^2}{s\ Pa}$. For the given gas inlet design and used volumetric flow rates the penetrating gas is $< 1\%$ of the total gas flow. Therefore the effect of gas permeability can be neglected.

The influence of swelling behavior in the presence of organic solvents (see Lee et al. (2003)) was analyzed by velocity measurements: Ethanol seeded with fluorescent particles was injected at a given volumetric flow rate. The velocity profile was analyzed by μ-PIV, see chapter 3.3.1. Then the channel was flooded with toluene at the same flow rate for 3 *h*. After this swelling time, the flow profile was measured again. No significant differences were detected.

3.1.2 Channels made of silicon

Experiments at high pressure values were conducted in channels made of Si/glass. A detailed description of the manufacturing process is given in (Waelchli; 2005) and (Trachsel; 2008). Briefly summarized, double-side polished Si-wafers were covered with photoresist (AZ 4562, Clariant). After exposure and devolvement the channels were etched (Deep Reactive-Ion Etching). The same procedure was repeated at the wafer backside to create the inlet/outlet holes. To close the channels, the wafer was finally anodically bonded to a glass wafer to provide optical access. The processed wafer was cut into reactor pieces by a dicing saw. Connections to the tubing was realized either by soldered capillaries (Trachsel; 2008) or by self-fabricated connection ports of PEEK. These ports contained a screw inside for connection and were glued on the channel back side.

3.2 Experimental setup

3.2.1 Used fluids

In this work, different gases and liquids were used. For the two-phase flow characterization nitrogen was used as gaseous phase. As liquid phase ethanol, toluene, water or glycerol in aqueous solution of different concentration was used. The absorption experiments were performed with CO_2 as gas and a 0.1 M solution of sodium hydroxide. The physical properties of all fluids used are given in table 3.2. The pressure dependent properties of nitrogen and water are described in 3.3.
Traces of rhodamine B (c=$5 \cdot 10^{-5}$ mol/l, Fluka), vanillin ($c = 1$ g/l, Sigma Aldrich) and sodium hydroxide ($c = 0.1$ M, Schweizerhall) where added to the liquid phase to investigate the hydrodynamics or mass transfer. Since the concentration of these additives was very small, an influence on the physical properties of the fluid can be neglected.
The contact angles of these fluids on reactor material surfaces were analyzed by the sessile drop method (Krüss DSA 10).

3.2.2 Flow scheme

The gas phase, nitrogen or CO_2, was delivered from a gas cylinder (PanGas). The volumetric flow rate was controlled via a mass flow controller (Bronkhorst, accuracy ±0.5% of reading plus ±0.1% full scale). Three different sized mass flow controllers were used: $\dot{V_G}^{max} = 1$ ml/min, $\dot{V_G}^{max} = 8$ ml/min and $\dot{V_G}^{max} = 400$ ml/min. The liquid was delivered and controlled by a syringe pump (Havard Apparatus, accuracy within

Table 3.2: Physical properties of used fluids at 20°C and atmospheric pressure, Yaws (1999)

Fluid	Density $[kg/m^3]$	Surface Tension $[10^{-3}\ N/m]$	Viscosity $[mPa\ s]$
Ethanol	789.4	21.97	1.074
Toluene	869.4	28.52	0.5805
Water	998.3	74.54	1.025
20 wt% Glycerol in water	1050	70.2	1.76
40 wt% Glycerol in water	1103	68.2	3.72
60 wt% Glycerol in water	1155	66.9	10.8
Nitrogen	1.25		0.0173
CO_2	1.98		0.0148

Table 3.3: Properties of nitrogen and water at different pressure values.

		30bar	60bar	90bar	120bar
Nitrogen					
$\rho\ \left[\frac{kg}{m^3}\right]$	Kao and Kobayashi (1967)	34.76	69.57	89.63	137.52
$\eta\ \left[10^{-6}\frac{kg}{m\cdot s}\right]$	Kao and Kobayashi (1967)	1.837	1.894	1.989	2.058
Water					
$v\ \left[10^{-3}\frac{m^3}{kg}\right]$	Wagner et al. (2000)	1.000	0.999	0.998	0.996
$\eta\ \left[10^{-6}\frac{kg}{m\cdot s}\right]$	Wagner et al. (2000)	1000.39	999.19	998.06	996.99
$\sigma\ \left[\frac{mN}{m}\right]$	Slowinski et al. (1957)	69.972	67.953	65.934	63.915

0.35% and reproducibility within 0.05%). One-way syringes (B.Braun) of $V = 10\ ml$, $V = 20\ ml$ and $V = 50\ ml$ were used. For experiments with liquid-liquid flow, the gas cylinder was removed and a second syringe was installed. The connections to and from the microreactor were established using PEEK-capillaries ($d_i = 250\ \mu m$, Upchurch). The pressure was measured via pressure transducers (Endress and Hauser, accuracy ±0.5% of full scale) at the inlet and the outlet of the reactor to obtain the pressure drop of the reactor. A flow scheme is depicted in Fig.3.2. For the high pressure experiments the liquid was stored and delivered in a syringe pump (Isco). The pressure of both phases was measured individually (Endress & Hauser) and was recorded by LabView®. Via PEEK-capillaries the fluids were brought to and removed from the microreactor. After passing a filter the pressure was controlled by a back pressure regulator (Jasco). The outlet pressure of the two-phase flow was measured in front of the filter.

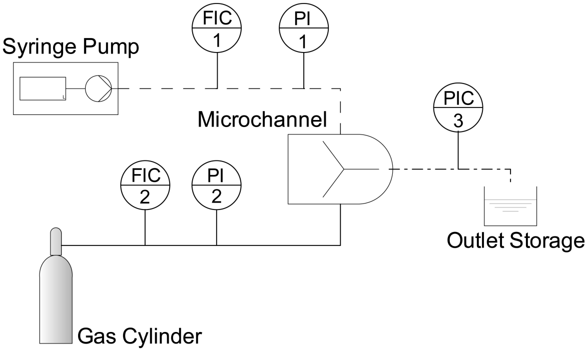

Figure 3.2: Scheme of the experimental setup.

3.3 Experimental methods and data analysis

3.3.1 Hydrodynamic characterization

Flow visualization in microchannels is challenging due to the optical resolution and refraction effects. Laser Induced Fluorescence (LIF) and μ-PIV (Particle Image Velocimetry) are common methods to overcome these challenges. A review of different flow visualization techniques was given by Sinton (2004). First PIV-measurements in microchannels had been performed for one-phase flow by Santiago et al. (1998) and Meinhart et al. (1999). Depending on the particle size and the optical resolution, the spatial resolution of the calculated velocity profile approaches values below 1 μm. The accuracy of the measurements corresponds with a tolerance of 2% of analytical solutions. $\mu-$PIV-measurements had also been used to investigate the onset of turbulence in microchannels (Natrajan and Christensen; 2007). Fujisawa et al. (2006) demonstrated the use of μ-PIV to determine the pressure field μ-T-junctions.

For two-phase flow with a non-steady-state flow, Guenther, Khan, Thalmann, Trachsel and Jensen (2004), Waelchli and Rudolf von Rohr (2006) and Fries et al. (2008) presented experimental results on the velocity field using μ-PIV. The challenge of $\mu-$PIV in instationary flow is the averaging: to decrease the measurement uncertainties many pictures need to be averaged. The area of interest, in this case the complete liquid slug, has to be selected first. The used method is described detailed in Waelchli and Rudolf von Rohr (2006). The liquid phase (rhodamine B-colored (Fluka) ethanol), was delivered by a syringe pump (Harvard Apparatus, PHD 2000). The gas phase(nitrogen), taken from gas cylinders, was controlled via mass flow controllers (Bronkhorst).

In this work, optical characterization of the flow was done by Laser Induced Fluorescence (LIF) and μ-Particle Image Velocimetry (μ-PIV). A scheme of the process is depicted in Fig.3.3.

An inverted microscope (Zeiss) and a standard fluorescence system (rho-

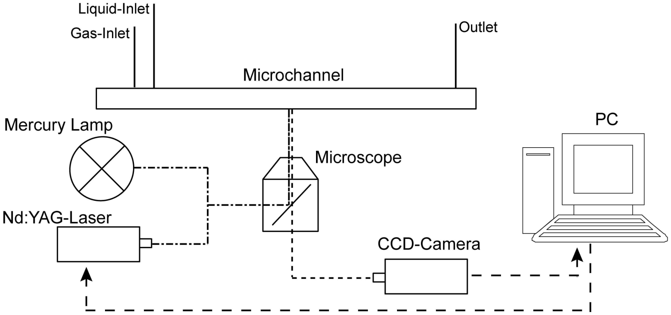

Figure 3.3: Scheme of the optical measurements.

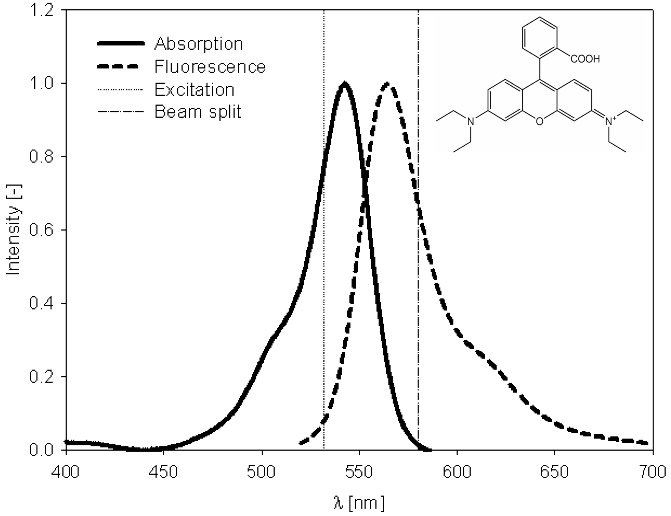

Figure 3.4: Absorption,fluorescence spectra and chemical structure of rhodamine B.

damine B filter set) were used. The illumination was achieved by a double-pulsed Nd:YAG - Laser (NewWave) or by a mercury lamp (Zeiss, HBO 100) at a wavelength of $\lambda = 532$ *nm*. The absorbtion and fluorescence spectra of rhodamine are illustrated in Fig.3.4. The emitted light passed a beam splitter (FS14, Zeiss) and was detected by the camera. Measurement errors due to reflection and refraction were diminished by the calibration. The synchronization of the laser shots and the camera was done by PTU 9 (LaVision).

The double-framed, double-exposed photos, taken by the CCD-camera, were analyzed by a Matlab®-programme. The liquid slug length L_S and the gas bubble length L_B were analyzed directly from the first frame. The velocity of the gas phase (which corresponds the velocity of the two-phase flow) was determined by using the second frame. Fig.3.5 illustrates the principle of this programme and defines the used symbols. For statistical reasons at least 200 pictures were analyzed. For the flow pattern investigation at high pressure values, 200 photographs for each velocity pair were recorded. Investigation of the slug lengths, of bubble lengths and of the film thickness was limited to Taylor flow regime.

For the mixing experiments, a DC mercury lamp was used. The reac-

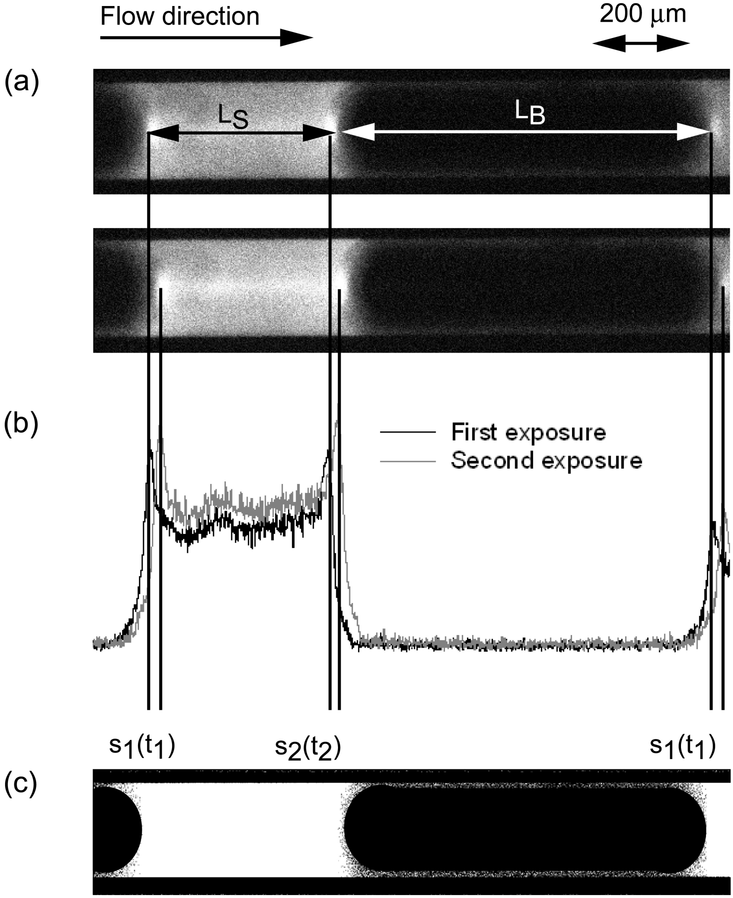

Figure 3.5: Characterization of the hydrodynamics. (a) Double-framed, double-exposed photograph. (b) Intensity profiles at the channel center. (c) Binarized first frame.

tor design was adapted to obtain two liquid inlets: one for the uncolored ethanol and one for the colored ethanol. The colored ethanol was injected at the liquid inlet 1 as illustrated in Fig.3.2. The uncolored ethanol was injected via inlet 2. The exposure time varied, depending on the velocity, between $t_{Exp} = 500\ \mu s$ and $t_{Exp} = 1000\ \mu s$, the sampling frequency of the camera was $f = 5\ Hz$. The mixing quality was determined with the intensity of segregation as presented by Danckwerts (1952). The intensity of segregation for a system of two miscible fluids is defined by

$$I_S = \frac{s_1^2}{\bar{c_1} \cdot \bar{c_2}} = \frac{s_2^2}{\bar{c_1} \cdot \bar{c_2}} \tag{3.2}$$

whereas $\bar{c}$ is the mean concentration of species 1 and 2 and s is the standard deviation. If the segregation is complete, meaning the concentration of both species at every point is either 1 or 0, I_S is equal to 1. The value of I_S decreases during the mixing process, until I_S is reduced to 0, where the complete homogenization is achieved. An equivalent measure is the intensity of mixing, defined as

$$I_M = 1 - \sqrt{I_S} \tag{3.3}$$

If $I_M > 0.95$, both fluids are supposed to be completely homogenized. The mixing length l_M is the channel length the two phase flow has to pass to achieve $I_M > 0.95$.

To characterize the liquid holdup, standard thresholding techniques in Matlab® were used for binarization of the single-framed, single-exposed LIF-pictures. Analyzing the recirculation in the liquid slugs was done by μ-PIV. As for the LIF-measurements, the double-pulsed Nd:YAG-laser was triggered by the PTU. With this system, double-framed, double-exposed pictures with a short time delay between both exposures ($\Delta t =$ 50...300 μs) were recorded. By seeding the liquid phase with fluorescent microspheres ($d_{Sphere} = 2\ \mu m$, Duke scientific), the liquid velocity profile in the channel center plane can be determined using the cross correlation algorithm. Optical distortions, such as reflection or refraction, were corrected in a calibration. The velocity field was analyzed based on the average of 200 pictures. Therefore, a postprocessing step for identification and extraction of the slugs at the correct position was added.

3.3.2 Chemical analysis

The organic phase was analyzed by a GC/MS system (Fisons Instruments GC8000/MD800), which was equipped with an Rtx-5MS (Restek) capillary column ($30\ m \times 0.25\ mm \times 0.25\ \mu m$). Split injections ($1\ \mu l$) were done with an autosampler (GC Pal) at a split ratio of 25 : 1 using helium as a carrier. The column was initially kept at $100°C$ for $5\ min$, and then ramped at $10\ K/min$ to $280°C$, where it was kept for $5\ min$. 4- ethylresorcinol (Alfa Aesar, 98%) in chloroform (Fluka, $> 99.8\%$) was used as internal standard.
Analysis of the aqueous phase was done via UV/Vis (Lambda 35, Perkin Elmer). The absorption was measured in a range of $\lambda = 190 - 500\ nm$. The vanillin characteristic absorption maximum at $\lambda = 280\ nm$ was compared with an external calibration. The pH-value was determined by a pH-meter (ProMinent, ±0.5% full scale).

Chapter 4

Influence of Channel Design on Hydrodynamics

4.1 Impact on the inlet design

The formation of bubbles at a T-junction was summarized in chapter 2.3. The mechanism of the bubble breakup is governed by the Laplace pressure. Since the Laplace pressure depends on geometrical parameters, we focused on the influence of the inlet design on the flow properties.

4.1.1 Specific experimental setup

The microchannels were made of PDMS, see chapter 3.1.1. 24 reactor designs, varying in the channel width $w = 200$, 300, 400 μm, gas inlet angle $\beta = 45°$, 90°, 135° and the ratio between the gas inlet and the channel diameter $\gamma = w_{Gas} : w = 1:1$, $1:2$, $1:3$ were used, see Fig.4.1. In table 4.1 all reactors are characterized and named with the term used in the following text. Whereas an inlet angle of $\beta = 90°$ inlet is

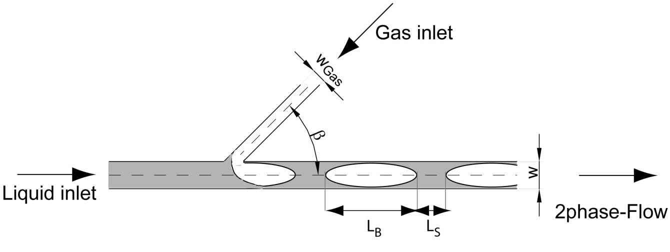

Figure 4.1: Scheme of the used microreactors.

Table 4.1: Design parameters of the used reactors

β	γ	$w = 200\ \mu m$ $h = 150\ \mu m$	$w = 300\ \mu m$ $h = 160\ \mu m$	$w = 400\ \mu m$ $h = 230\ \mu m$
90°	1 : 1	90-200-1	90-300-1	90-400-1
	1 : 2	90-200-2	90-300-2	90-400-2
	1 : 3	90-200-3	90-300-3	90-400-3
45°	1 : 1	45-200-1	45-300-1	45-400-1
	1 : 2	45-200-2	45-300-2	45-400-2
	1 : 3	45-200-3	45-300-3	45-400-3
135°	1 : 1	135-200-1	135-300-1	-
	1 : 2	135-200-2	135-300-2	-
	1 : 3	135-200-3	135-300-3	-

a commonly used design, the other angles had been chosen arbitrarily. The experimental setup and the optical characterization were realized according to chapter 3.

4.1.2 Gas bubble length

The gas bubble length for a constant superficial gas velocity at varying liquid velocities depends on the ratio of the flow rates as well as on the inlet design. In Fig.4.2, the measured gas bubble lengths as well as their distribution are plotted versus the volume transport fraction ε_L^* for all configurations with an 90°-inlet. In order to compare the values of different reactor widths, we divided the gas bubble length by the corresponding reactor width. For statistical reasons, at least 50 gas bubbles had to be taken into account. Note that gas bubbles with a length of more than 1300 μm exceeded the FOV and could not be detected by our optical system. For this case, no bubbles were detected and analyzed.

In general, increasing the liquid flow rate at constant gas flow rates leads to shorter gas bubbles. The dimensionless gas bubble length L_B/w is constant within the measurement uncertainties at constant flow rates. If the gas inlet diameter is smaller than the main channel, the gas bubbles are shorter compared to a ratio of $\gamma = 1$. Furthermore, the gas bubble length has less variation in length in this case for $\gamma > 1$, which is indicated by a significantly smaller standard deviation. The COV (standard deviation / mean value) never exceeds 10% of the gas bubble length and is in the

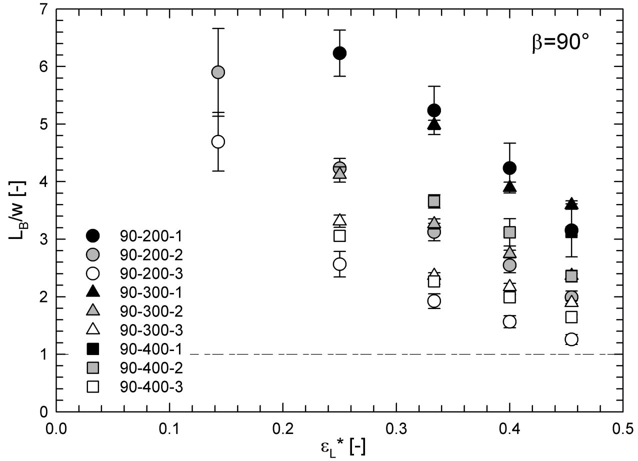

Figure 4.2: Measured gas bubble lengths for all 90°-inlet configurations versus the volumetric flow ratio. The line indicates a bubble length equal to the channel width.

range of 5% for 90% of all measurements performed in this study. Increasing the inlet angle leads to decreased gas bubble lengths. For constant flow rates, the influence of the inlet angle is less important compared to the influence of the inlet ratio. Furthermore, the stability is affected by the inlet angle: At a constant ratio $\gamma = 1$, inlet angles of 90° result in a more constant gas bubble length than inlet ratios of 45° and 135°. This effect diminishes if the width of the gas inlet is significantly smaller compared to the width of the main channel. Same tendencies were observed for 45° and 135°.

Fig.4.3 illustrates the measured gas bubble lengths depending on the volumetric flow ratios ε_L^* for different inlet ratios γ and inlet angles β. The values obtained for a reactor width of 300 μm and 400 μm lead to the same results. For a better visualization of the results the standard deviation, which has the same values as described above, is not plotted in Fig.4.3.

The reason for the decreasing gas bubble lengths at increasing inlet angles β might be caused by the interfacial pressure: As pointed out by Garstecki et al. (2006), the neck of the dispersed phase diminishes to a minimal value where the breakup occurs. Since the interfacial pressure

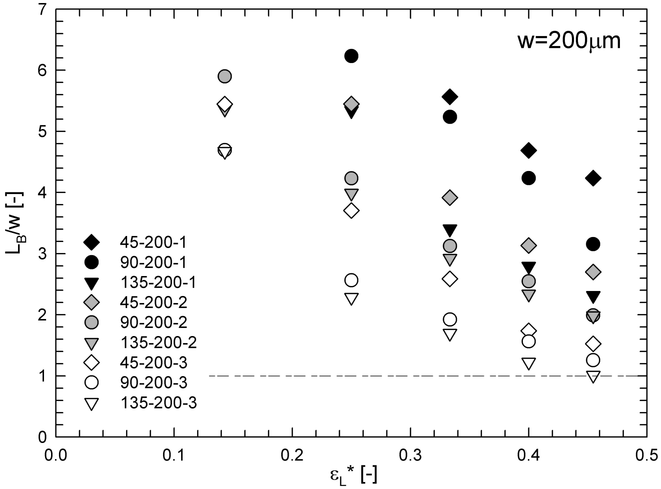

Figure 4.3: Measured gas bubble lengths for a width of 200 μm. The line indicates a bubble length equal to the channel width.

increases with decreasing radii, a faster thinning of the neck results in a faster breakup. This thinning was documented in Garstecki et al. (2006) for $\beta = 90°$: At the beginning, the width is equal to the width of the gas inlet. When the incoming gas covers the complete channel width, the gas bubble is deflected in the main channel in flow direction due to the incoming liquid. The width of the neck decreases approximately to the half of the inlet width and remains at this value for a while. As the pressure due to the incoming liquid increases, the width finally decreases sharply till the breakup occurs and the gas flow is interrupted.

In Fig.4.4 instantaneous images of the gas bubble formation are given for $\beta = 135°$ and $\beta = 45°$. For $\beta < 90°$ the gas flows towards the liquid inlet. Due to the initial flow direction of the gas phase, the initial width at the neck will be larger than for a $\beta = 90°$ inlet, the interfacial pressure is smaller. Since the neck width reaches its critical value for the breaking off later, the gas bubbles are longer. The opposite effect occurs for $\beta > 90°$: Since the gas flow has the same direction as the incoming liquid, the gas bubble moves toward the flow direction. The thinnest position of the gas bubble moves into the main channel, resulting in a faster breakup ("shearing") and therefore in shorter gas bubbles. This

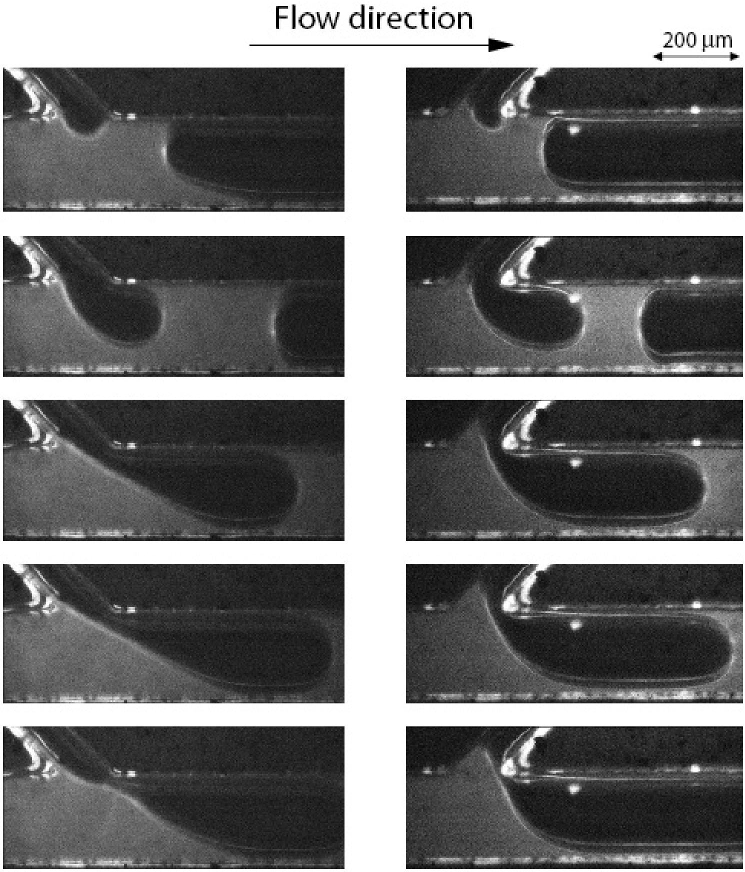

(a) Reactor 135-200-3 (b) Reactor 45-200-3

Figure 4.4: Gas bubble breakup for different inlet angles. Volumetric gas flow rate = 0.3 ml/min, volumetric liquid flow rate = 0.1 ml/min.

breakup mechanism also explains the decreased gas bubble length for increased γ. Since the initial total width at the neck is smaller, the critical width is achieved within a shorter time. This causes a faster breakup. In order to predict the gas bubble length, we have modified eq.2.10. Based on literature, α is assumed to be close to one. Since α strongly depends on the inlet geometry, we need to find a correlation to fit this

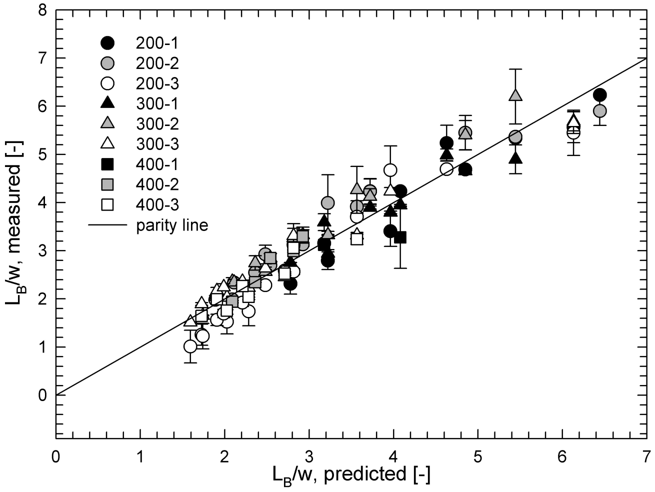

Figure 4.5: Dimensionless gas bubble length: model of eq.4.1 versus experiment.

geometrical value. Starting with

$$\alpha = f(\gamma,\beta) = a\ \gamma^b\ \beta^c \tag{4.1}$$

and using the least square fit method, we obtained the following values with a correlation coefficient of 0.96:

$$a = 17.2131$$
$$b = -1$$
$$c = -0.5$$

Using the geometrical design parameters from Garstecki et al. (2006), α can be calculated to $\alpha = 0.91$, which is close to the assumed value of $\alpha = 1$. The discrepancy might be caused by different aspect ratios and the measurement uncertainties.

In Fig.4.5 the measured values for the dimensionless gas bubble length are plotted versus the ones predicted by eq.4.1. Taking the measurement uncertainties into account, we state that the model matches the experimental results quite well. Therefore, at a constant geometry, the gas bubble length increases with an increasing ratio of gas to liquid flow rate.

4.1.3 Liquid slug length

Since pressure drop and mass transfer strongly depend on the liquid slug length, detailed knowledge on the resulting slug length is mandatory. In Fig.4.6, the measured dimensionless slug lengths are plotted versus the volume transport fraction ε_L^* for all inlets with $\beta = 90°$. The volumetric flow rates were kept constant so that the corresponding velocities of the flow are higher for small channels.

As for the dimensionless gas bubble length, the dimensionless liquid slug length depends for a constant inlet angle of $\beta = 90°$ on ε_L^* as well as on the inlet ratio γ. Increasing the liquid flow rate compared to the total flow rate results in an increase of the liquid slug length, which corresponds to literature results (Laborie et al.; 1999; Liu et al.; 2005). If the width of the gas inlet is smaller than the width of the main channel, the liquid slug length decreases. This is the same trend as it was observed for the gas bubble length: For a given inlet angle and flow rate, an inlet design with increasing γ leads to decreasing unit cell lengths.

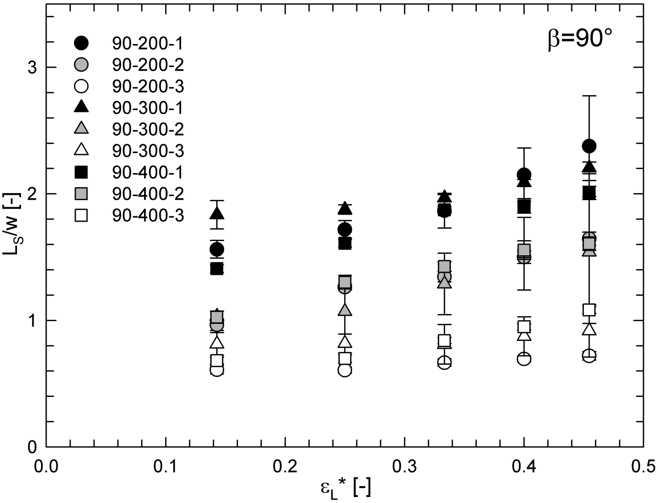

Figure 4.6: Dimensionless slug length for all reactors with a 90°-inlet.

In Fig.4.7 the influence of the inlet angle for a given channel width and different inlet ratios is plotted versus the volumetric flow ratio. For illus-

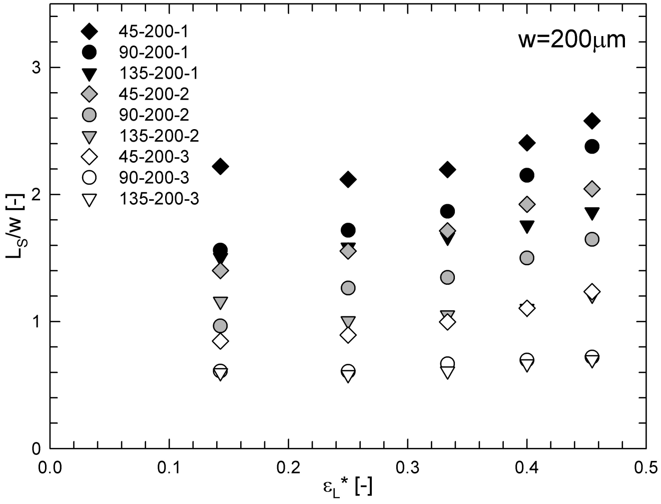

Figure 4.7: Dimensionless slug length for all reactors with $w = 200$ μm.

tration reasons the standard deviation was left out. Note that in most experiments the measured standard deviation is below 5%. For all inlet ratios and ε_L^*, increasing β results in decreasing liquid slug lengths, whereas this effect overlaps with the influence of γ. The reason for this observed effect can be found in the interfacial pressure. As described above, inertia of the inflowing gas affects the width of the gas bubble at the neck and thus the breakup mechanism: If the gas bubbles are short due to the geometry at given flowrates, less liquid is hindered to flow into the channel and thus the liquid pressure is not as high as for long gas bubbles. Hence the momentum of the flowing liquid is smaller resulting in a slower initial velocity and thus in shorter liquid slug lengths.

For all geometries, an increase of the liquid flow rate (and therefore of ε_L^*) results in an increase of the liquid slug length. If the ratio of the main channel to the gas inlet channel width increases, the liquid slug length decreases. The standard deviation of the liquid slug length is affected by the inlet ratio γ; small values of γ lead to greater deviations in the liquid slug length. If $\gamma = 1$, the dimensionless liquid slug length is in the range of 2...3 for all investigated channel diameters. For $\gamma = 2$, the slug length is 1 to 2 times of the hydraulic diameter, whereas for $\gamma = 3$ slug lengths in the range of the hydraulic diameter were observed.

Based on Fig.4.6 and Fig.4.7, the dimensionless liquid slug length depends on ε_L^*, β and γ. As known from literature (Kreutzer, Kapteijn, Moulijn, Kleijn and Heiszwolf; 2005), the surface, viscous and inertia forces, expressed by

$$\frac{Re}{Ca} = \frac{\text{inertia forces} \times \text{surface forces}}{(\text{viscous forces})^2} \tag{4.2}$$

have a significant influence on the liquid slug length. Correlating

$$\frac{L_S}{w} = k \cdot ln\left[\left(\frac{Re}{Ca}\right)^{0.33} \frac{\varepsilon_L^*}{\gamma^l\ \beta^m}\right] + n \tag{4.3}$$

and using the least square method for all 120 experiments, we obtained

$$\begin{aligned} k &= 0.369 \\ l &= 2.5 \\ m &= 1 \\ n &= 3.15 \end{aligned}$$

The measured dimensionless liquid slug lengths as well as the results of eq.4.3 are plotted in Fig.4.8. The correlation coefficient between the measured and the predicted data is 0.94. Taking the measurement uncertainties into accout, the correlation describes the experimental data for the investigated range of $\varepsilon_L^* = 0.1...0.5$ well.

Obviously, an increase of ε_L^* (while keeping all other parameters constant) results in an elevated slug length by factor $l \cdot n(\varepsilon_L^*)$. Since ε_L^* takes values between 0 and 1, the increase due to changes in ε_L^* can be assumed to be linear. Changes of γ are also very significant: increasing γ from 1 to 2 leads to a decrease of the dimensionless slug length by 33%. In our experiment the factor Re/Ca was in the order of 1000 and influenced the slug length: Increasing inertia forces caused by increased flow rates or the density of the liquid used leads to increased liquid slug lengths. A decrease of the surface tension forces which can be realized using surfactants or other liquids results in a decreased liquid slug length. Increasing the viscosity while keeping all other parameters constant leads to decreasing liquid slug lengths.

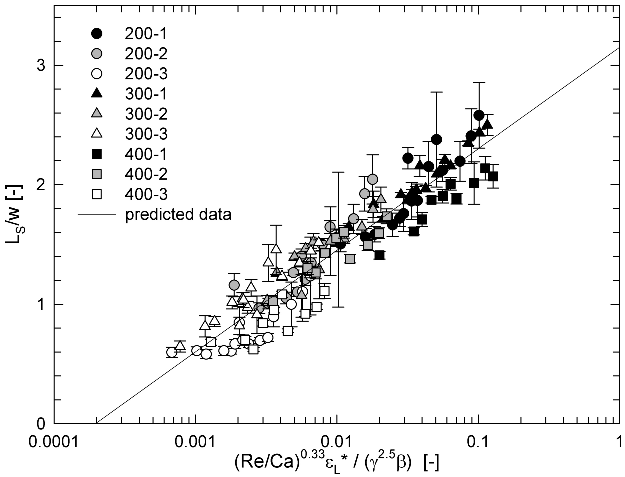

Figure 4.8: Dimensionless slug length for all reactors versus $(Re/Ca)^{0.33}\ \varepsilon_L^*/(\gamma^{2.5}\ \beta)$.

4.1.4 Phase distribution and unit cell length

An important parameter of Taylor flow is the dimensionless unit cell length $(L_S + L_B)/w$. The liquid slug length defines, together with the velocity, the frequency of gas - liquid flow. It had been shown for packed bed reactors, that the optimal frequency of two-phase flow increases the conversion, selectivity and yield (Wu et al.; 1995). In Fig.4.9 the dimensionless unit cell length is plotted for all designs with a 90°-inlet versus ε_L^*. The unit cell length increases with decreasing ε_L^* and increases proportionally with the channel width. A decrease of the unit cell length and thus enhanced mass transfer can be achieved by decreasing the gas inlet width at a constant channel width.

The influence of the inlet angle is not plotted, but according to the results above we state the following: if the gas flow is injected into the main channel in the same direction as the two-phase flow occurs, the unit cell length decreases.

The ratio of gas bubble to liquid slug length versus ε_L^* is plotted in Fig.4.10 for all inlet configurations with $\beta = 90°$. The ratio is enhanced compared to the ratio of the corresponding flow rates, which is most

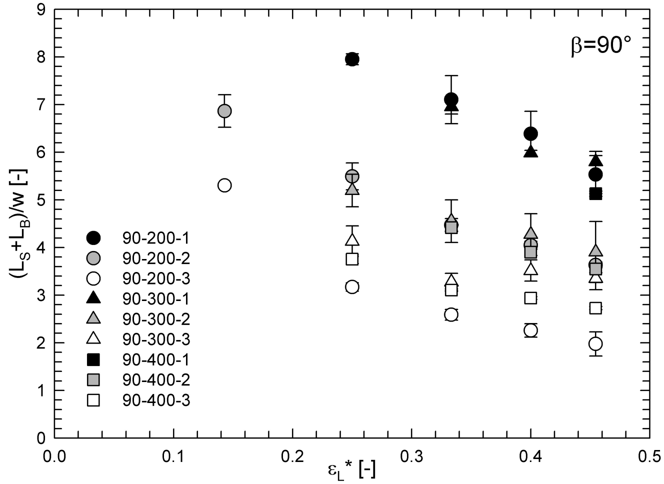

Figure 4.9: Dimensionless unit cell length for $\beta = 90°$. Ratio of the flow rates is presented by the line.

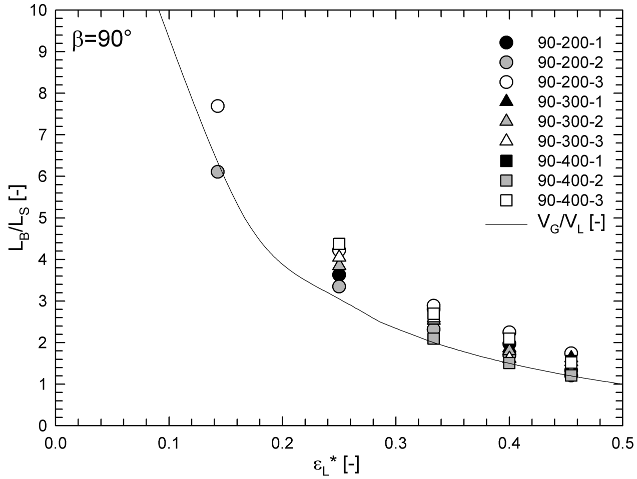

Figure 4.10: Dimensionless unit cell length for $\beta = 90°$.

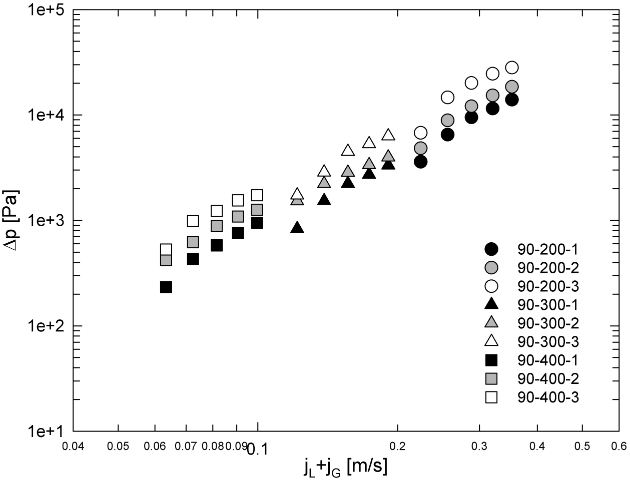

Figure 4.11: Measured pressure drop for all 90°-designs versus the total superficial velocity.

pronounced for a channel width of $w = 400\ \mu m$ and less important for $w = 200\ \mu m$. This is due to the 2-dimensional analysis of a 3-dimensional shape: Since the bubble front as well as the bubble tail consist of a ellipsoid-like shape, the detailed volume of which is difficult to determine (starting with a circular cross section at the front to a rectangular cross section), we plotted only the maximum bubble length and minimum slug length.

4.1.5 Pressure drop

In Fig.4.11 the measured pressure drop for the 90° designs is plotted versus the sum of the liquid and gas superficial velocity. The pressure drop is influenced by the superficial velocity and the ratio of the gas inlet β. The influence of the channel width can be neglected, since all measured data points show a straight line for all investigated channel widths at the corresponding gas inlet. Due to an increase in Re, the pressure drop increases with increasing total superficial velocity. For the same volumetric flow rates in the gas and in the liquid phase, the pressure drop increases with decreasing channel width and thus an in-

creasing Re. Note that the design of the gas inlet influences the pressure drop: $\Delta p_{\gamma=1} < \Delta p_{\gamma=2} < \Delta p_{\gamma=3}$. This is caused by the resulting liquid slug length.
The gas-liquid pressure drop in microchannels consists mainly of a frictional pressure drop (see section 2.3) and can be calculated by eq.4.4.

$$\Delta p_{fric} = f\ \rho_L\ (j_L + j_G)^2\ \frac{2}{d_h}\ \varepsilon_L\ L_R \tag{4.4}$$

whereas the friction factor f is determined by Kreutzer, Kapteijn, Moulijn, Kleijn and Heiszwolf (2005) as

$$f = \frac{16}{Re}\left[1 + a\ \frac{d_h}{L_S}\left(\frac{Re}{Ca}\right)^{0.33}\right] \tag{4.5}$$

The parameter a was found to be dependent on the flow conditions and was found to be $a = 0.17$ for a circular capillary with $d_h = 2.3\ mm$ and $Re < 50$. In our case (rectangular PDMS-glass microchannels), the least square method gave $a = 0.225$ for $w = 200\ \mu m$, $a = 0.21$ for $w = 300\ \mu m$ and $a = 0.185$ for $w = 400\ \mu m$. The decrease of a for an increasing channel width corresponds to the influence of the wall effects. The correlation coefficient amounts 0.98. In Fig.4.12 the pressure drop is plotted versus the dimensionless slug length for all reactor designs. For the experimental data, f was calculated from the measured pressured drop using eq.4.4. With the adapted a for different channel widths a dependence of the friction factor on the liquid slug length is visible. Liquid slug lengths in the range of 2...3 d_h, obtained by $\gamma = 1$, result in a small frictional pressure drop compared to short liquid slug lengths in the range of d_h and less. This is valid for all channel widths. Note that $f \cdot Re$ depends only on L_S/d_h, independent of the geometry. Since all experiments were performed at the same flow rates, L_S/d_h obviously depends only on the flow rate and on β. According to Kreutzer, Kapteijn, Moulijn, Kleijn and Heiszwolf (2005) the single phase limit of $f \cdot Re = 16$ is obtained asymptotically for $L_S/d_h > 20$. Since we never obtained such large liquid slug length in our experiments, we cannot validate this value experimentally; nevertheless extrapolating our measurements results support this information.

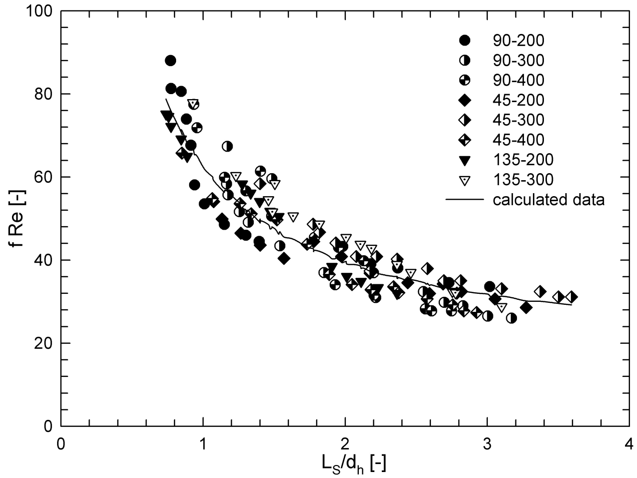

Figure 4.12: ($f\ Re$) as a function of the dimensionless slug length for all designs. Points are the measured values, the dotted represents the calculated friction factor according to eq.4.4.

4.2 Enhanced mixing by meandering channels

As mentioned in chapter 2.3, the liquid slug is divided into two axially symmetric rotation areas. Whereas the mass transfer within these halves is very good, mixing between both halves is diffusion based and therefore slow. To increase the mass transfer between these halves, meandering channels as passive mixers were investigated. To our knowledge, nothing has been reported on the influence of active mixers like ultrasound or microwaves on mixing in Taylor flow.

4.2.1 Specific reactor design

The channel width was 200 μm and 400 μm, the height was 180 μm. A straight channel was compared with different meandering channels. The radii were varied between 1 *mm* and 2 *mm*. Fig.4.13 shows the used designs, table 4.2 gives the design parameters. For the mixing experiments according section 3.3.1, two liquid inlets and one gas inlet as described in section 4.1 were used.

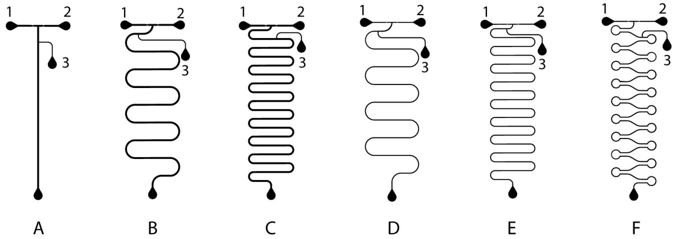

Figure 4.13: Illustration of the analyzed reactor designs. Inlet 1 and 2 are the liquid inlets, 3 is the gas inlet.

Table 4.2: Geometrical characterization of the analyzed channel designs

Reactor [−]	Channel width *w* [μm]	turning radius *r* [mm]	turning angle α [°]
A	400	-	-
B	400	2	180
C	400	1	180
D	200	2	180
E	200	1	180
F	200	1	320

4.2.2 Mixing quality

To compare the mixing efficiency, we evaluated the mixing length based on the intensity measurements for an intensity of mixing at $I_M = 0.95$. Note, that the values for the straight channel are extrapolated from the measurements, assuming linear behavior. The mixing lengths versus the sum of the superficial velocities are illustrated in Fig.4.14. Obviously it takes a long time until homogenization of the two liquid slug halves is achieved in a straight microchannel. The reason for this is the symmetrical recirculation. Diffusion is the only mechanism providing mass transfer between both halves.

Use of a meandering channel reduces the mixing length by factor 2.4 (Reactor B) up to 8 (Reactor F). Based on the experimental results small curve radii ($r = 1$ mm, see Reactor C, E and F) provide enhanced mixing compared to larger curve radii ($r = 2$ mm, Reactor B and D). This can

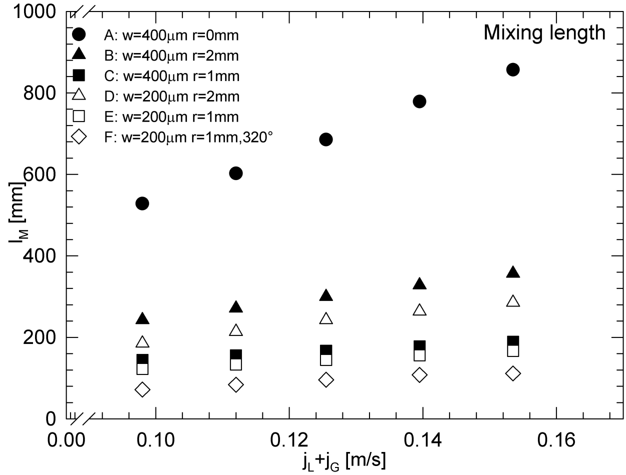

Figure 4.14: Mixing length for different reactor designs and superficial velocities.

be explained by centrifugal forces, which are reversed proportional to the radii (reducing the radius by 50% results in a doubled centrifugal force), and geometrical consideration: The slug itself is bent stronger for smaller radii. For $L_S/w = 1$, the bending angle of the slug is 19° for Reactor C, 10° for Reactor B and E and 5° for Reactor D.

Taking these phenomena into account, the experimental results can be explained as follows: for the meandering geometries, Reactor B ($w = 400\ \mu m$, $r = 2\ mm$) provides the worst mass transfer across the channel center line. Compared to Reactor D ($w = 200\ \mu m$, $r = 2\ mm$), where the centrifugal forces are in the same range, mixing is limited due to the longer total slug length. Another reason is the larger channel width, resulting in a longer mixing time. For a given channel width, reducing the curve radius gives shorter mixing times as well, compare Reactor B and C or Reactor D and E. Based on these results, an extrapolation towards mini-reactors should lead to efficient mixing. The Taylor flow regime with its characteristic recirculation appears in millimeter-sized capillaries (Taylor; 1961; Thulasidas et al.; 1997). Since the formation of the recirculation occurs by the shearing forces close to the wall, the effect

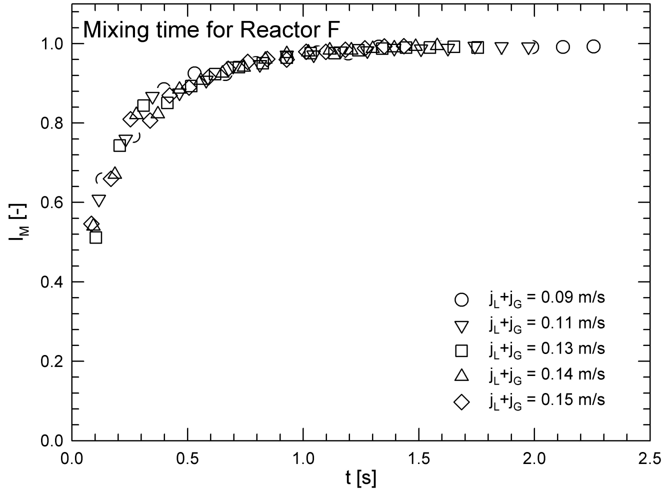

Figure 4.15: Mixing time for one reactor design at different velocities. The ratio of j_G to j_L was varied between 1.2 and 6.

of meandering channels on the flow profile in millimeter-sized capillaries will be similar to the situation in microreactors. At constant velocities and given curve radii, the mixing length will slightly increase at increasing channel diameter. The mixing length per mixed volume will decrease at increasing diameter. Regarding Fig.4.14 it is important to note that the extrapolation of all measured points would lead to the origin, indicating a constant mixing time for a given geometrical configuration. A velocity close to zero would require a very short mixing length, but the time is the same as for higher velocities. This is illustrated more detailed for Reactor F ($w = 200\ \mu m$, $r = 1\ mm$, $\alpha = 320°$) in Fig.4.15. For the investigated range (Taylor flow) no influence of the sum of the superficial velocities ($j_L + j_G$) can be seen. This is only valid, if the same mechanism of mixing occurs.

4.2.3 Slug length

Since the liquid flow rate was varied at a constant gas flow rate, increasing the liquid and the gas superficial velocity $j_L + j_G$ values means not only decreased residence times but also a shorter liquid slug length which is an important parameter for the mass transfer. In order to compare the slug lengths for different channel widths, the ratio L_S/w is the common parameter. The results are plotted versus the sum of the superficial velocities in Fig.4.16. Since the superficial gas velocity was kept constant, an increase of the two-phase velocity corresponds with an increase of the liquid volume transport fraction ε_L^*.

We demonstrated in section 4.1.3 the dependence of the liquid slug length on the channel width, the fluid properties and the inlet configuration, which can be stated for the current case:

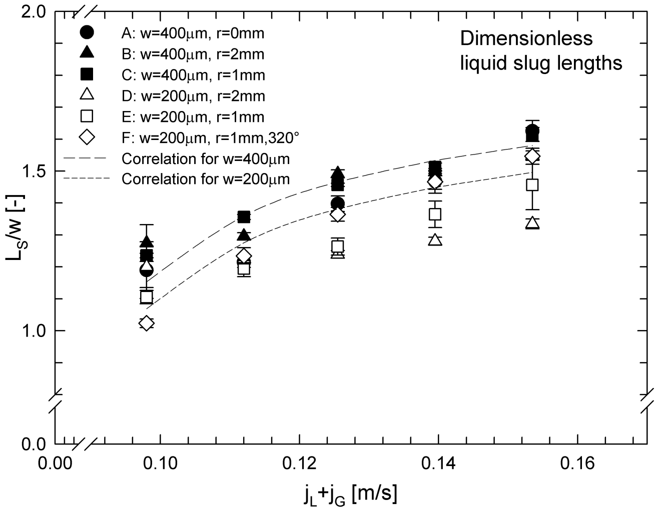

Figure 4.16: Dimensionless liquid slug lengths for all reactor designs at different superficial velocities.

$$\frac{L_S}{w} = 0.369l \cdot n \left[\left(\frac{Re}{Ca} \right)^{0.33} \frac{\varepsilon_L^*}{509.12} \right] + 3.15 \tag{4.6}$$

The corresponding values are plotted as lines in Fig.4.16. The predicted values are verified by the measured dimensionless slug lengths. Although the liquid slug lengths vary with ε_L^*, all observed liquid slug lengths were in the range from 1.1...1.6 times the channel width. As had been pointed out by Kreutzer, Kapteijn, Moulijn, Kleijn and Heiszwolf (2005), the increase of the Sherwood-number Sh due to changes in the liquid slug length is below 15% of the *Sh*. For a straight channel, the changes in the slug length will not affect the mass transfer significantly. For meandering channel designs, longer slug lengths provide an enhanced mass transfer due to the bending angle of the slug: shorter slugs have a smaller turning angle than longer slugs, providing an enhanced asymmetrical flow pattern. The optimal slug length for fast mixing depends on the bend geometry.

4.2.4 Pressure drop

The pressure drop had been measured as the difference between the pressure at the liquid inlet and the two-phase outlet. Hence the pressure drop consist of the resistance during the formation of the gas bubble and the two-phase frictional pressure drop. The pressure drop at the gas inlet was estimated according to Garstecki et al. (2006) with the Hagen-Poiseuille equation:

$$\Delta p = 32\frac{\dot{V}_L \eta_L L_G}{hf^3} \tag{4.7}$$

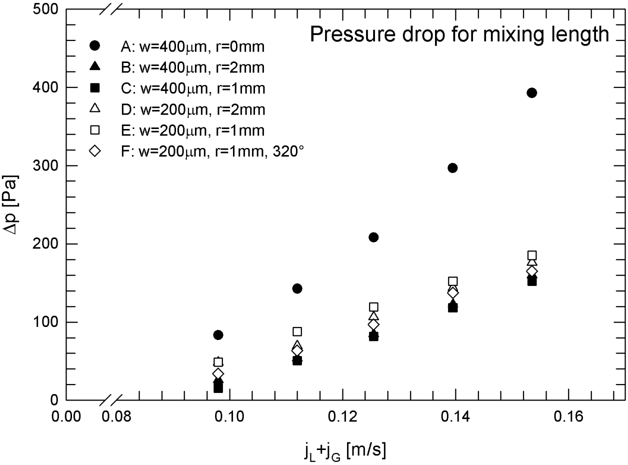

Figure 4.17: Pressure drop for mixing length. The pressure drop for the bubble formation has been subtracted.

Assuming the film thickness between the growing gas bubble and the wall $f \approx 0.04w$ and the length of the growing gas bubble with $L_G = 0.5\ L_B$ results in pressure drop values for the formation of gas bubbles between 10...15 *Pa*. This estimated value had been subtracted from the measured pressure drop over the reactor length. The pressure drop per reactor length increases with decreasing channel curve radius and channel width. As these parameters enhance the mixing intensity, we plotted the pressure drop for the mixing length versus the sum of the superficial velocities in Fig. 4.17. The pressure drop per mixing length increases for all reactor geometries with increasing total superficial velocity, which is mainly due to the enhanced mixing length for these values. Comparing the reactor designs, meandering channels will enhance the mixing efficiency per pressure drop. Note, that all meandering reactors produce approximately the same pressure drop for the required mixing length. In other words, the enhanced pressured drop leads solely to enhanced mixing. This indicates that the vorticity effects, resulting in an enhanced mixing, linearly increase the pressure drop. The enhanced total pressure drop results directly in the mixing efficiency and has no other effects as friction. The differences between the pressure drop per mixing length for the meandering channels are to small compared to the measurement uncertainty to allow a serious discussion. However, it seems that the microchannels with the larger cross section provide a slightly lower pressure drop per mixing length.

4.2.5 Velocity profile

The velocity profiles were analyzed experimentally by μ-PIV measurements and numerically. Therefore the recirculation inside the slug had been calculated in Comsol® 3.3. The geometry of the slug (slug length and the shape of the front and tail) in the bend was given by the experimental results. All simulations were done in two-dimensional mode. For convergence reasons the unstructured trigonal mesh consisted of at least 10,000 elements. The wall was set as no slip with a velocity in x-direction (streamwise) according to the bubble velocity. The slug front and tail were set as no slip with no velocity. As fluid properties in the subdomain those of ethanol were chosen. The Navier-Stokes-Equations were solved with the standard solver of Comsol®. Convergence was obtained within 500 iterations. The velocity profile was extracted and compared with the experimental results.

To explain the enhanced mixing by meandering channels we were interested in the velocity profile. The measured velocity profile as well as the simulated one is shown for different bend geometries in Fig.4.18 for a slug velocity of $j_L + j_G = 0.16\ m/s$. The experimental data verify the simulated values. Independent of the geometry, the vortex on the bend inner side moves towards the channel outer half and shifts slightly back. The outer vortex is divided into two parts, one in the slug front and one in the slug tail area. This effect is less pronounced for the reactor configuration with a bend diameter of $r = 2\ mm$ and a channel width of $w = 200\ \mu m$, see Fig.4.18 (4). According to the simulation, the outer vortex had not been divided into two independent vortices. In the experiment, one inner and one outer vortex, similar to the situation in a straight channel, were observed. Comparing the influence of the channel diameter at different bend radii (Fig.4.18. (1) - Fig.4.18. (2) and Fig.4.18. (3) - Fig.4.18. (4)) indicate splitting of the outer vortex. The movement of the inner vortex to the channel outer half is more pronounced for a smaller bend radius. This corresponds to the mixing results described above, where

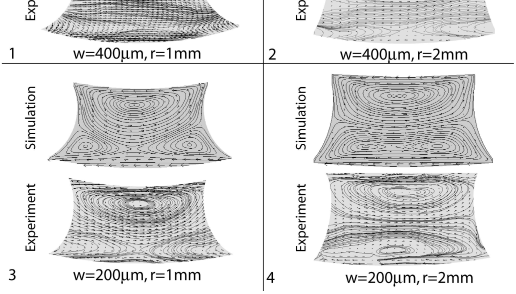

Figure 4.18: Recirculation in the bend: comparison of the simulation and experiments. $j_L + j_G = 0.16\ m/s$ had been subtracted from the bulk velocity for all cases. Simulated data are at the top, experimental results at the bottom of each quarter.

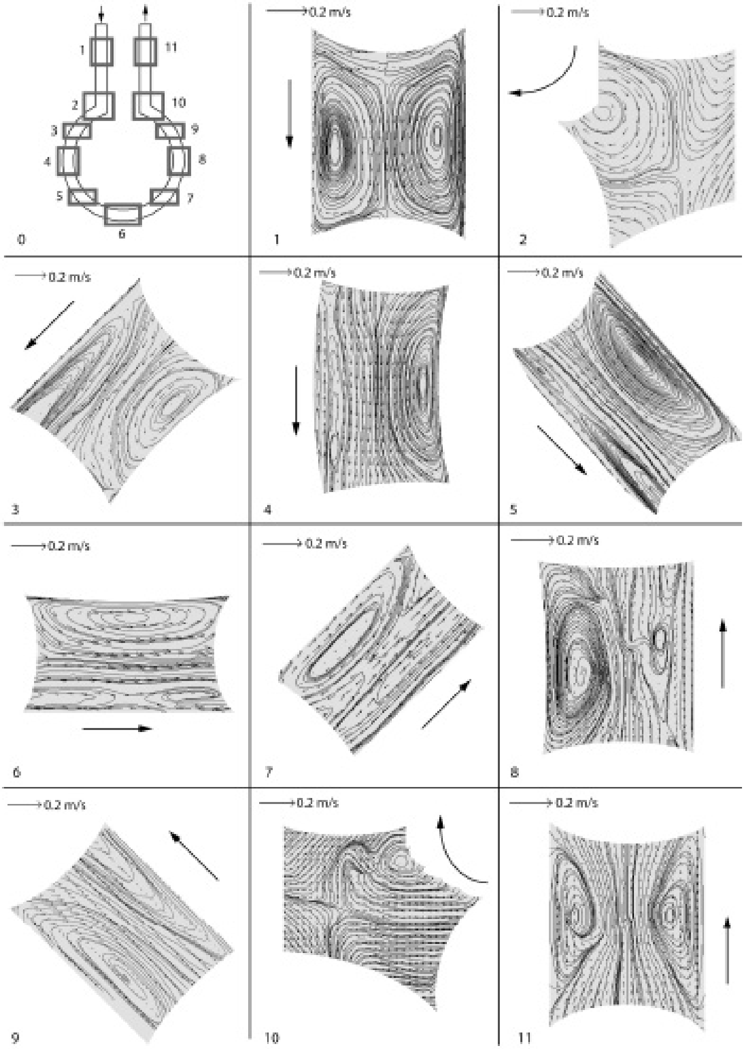

Figure 4.19: Velocity profiles for Reactor F obtained from the experiments. The bulk velocity, taken from the measurements, was subtracted.

shorter mixing times were obtained at smaller radii. The influence of the channel diameter at a constant bend radius (Fig.4.18. (1) - Fig.4.18. (3) and Fig.4.18. (2) - Fig.4.18. (4)) indicates that changes in flow pattern compared to the straight channel are stronger for the larger channel width. This is due to the more pronounced influence of the wall at the smaller channel. Since the mass transfer depends on the channel width, the smaller channel mix faster although the velocity profile led to another assumption.

To explain the enhanced mixing of Reactor F with the 320°-bend the measured velocity profiles for the movement relative to the slug velocity are plotted for Reactor F at different positions in the bend in Fig.4.19. Before the slug enters the bend, see Fig.4.19.(1), the recirculation is symmetrical to the channel center and equal to that what is known for straight channels. To achieve the 320°-bend, a kink, interrupting the round bend shape, had been placed. At this kink, see Fig.4.19.(2), the velocity profile is interrupted. The vortex at the kink inner side reaches the outer side and divides the outer vortex into two regions. This short interruption in the velocity profile certainly enhances mixing effectively, see Fig.4.14. As soon as the bend with a regular curve is achieved (Fig.4.19.(3) - Fig.4.19.(9)), the vortex at the inner side is shifted to the slug end and covers slightly the outer half, whereas the outer vortex is shifted to the front. The vortex at the outer half covers a larger area than the vortex at the inner half. By passing the bend, the vortices finally divide the channel diagonally. At the kink, see Fig.4.19.(10), the same phenomenon as in Fig.4.19.(2) occurs. Finally, when the slug is in a straight channel again, the symmetrical profile, see Fig.4.19.(11), is formed. It should be noted, that for all observed velocities the measured profile gives the same trend which corresponds to the simulation results discussed below.

The influence of the slug velocity on fluid flow across the channel center line was investigated numerically and is shown in Fig.4.20. The velocity component in y-direction (orthogonal to the flow direction) divided by the slug velocity is plotted versus the dimensionless liquid slug length. Negative values characterize a movement towards the channel outer wall. For a straight channel design, $u_y/(j_L + j_G)$ across the channel center line is zero. For all four investigated geometry configurations an increase of the slug velocity results in a more asymmetrical velocity profile. Three different general velocity fields were observed: For $j_L + j_G < 0.64\ m/s$ the vortex of the inner half crosses the channel center line at the slug

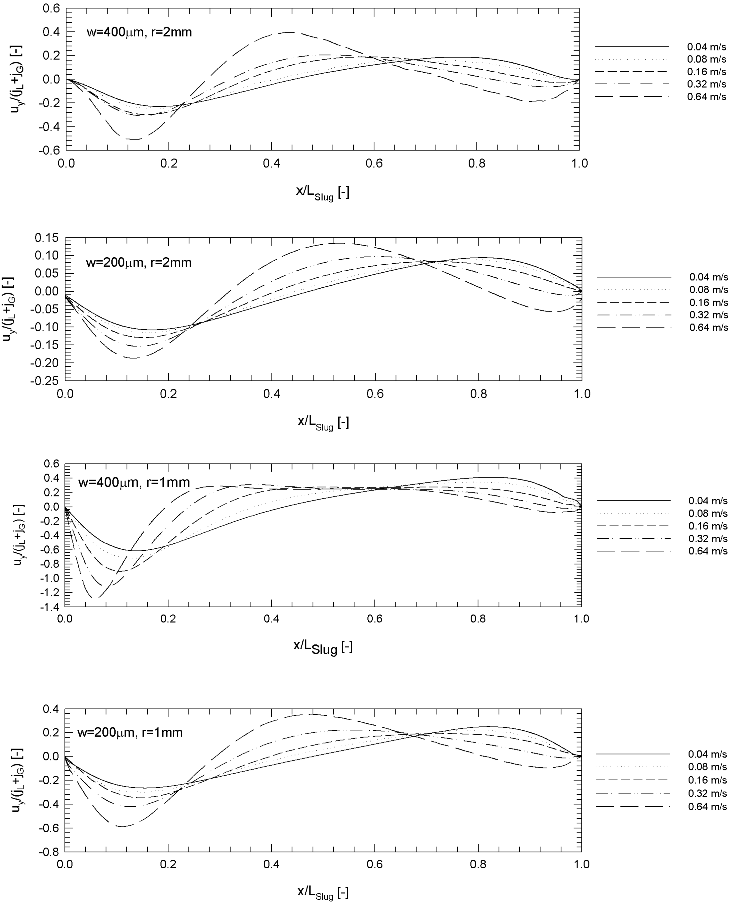

Figure 4.20: Simulated wall normal velocity profiles at the channel center line. Slug length had been normalized. Wall normal velocity component was divided by the bulk velocity.

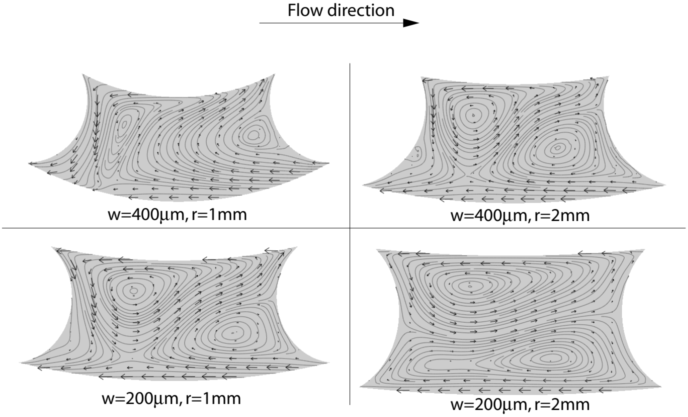

Figure 4.21: Stationary recirculation in the bend: results from the simulation for $j_L + j_G = 0.64\ m/s$.

back ($x/L_S < 0.5$) and the vortex at the channel outer half covers the channel center line at the slug front ($x/L_S > 0.5$). This corresponds to the observations from Fig.4.18. The absolute velocity in y-direction over the channel center line relative to the slug velocity reaches higher values for increasing slug velocities. Since at higher velocities Re increases, this indicates the influence of inertia. For very small velocities inertia is negligible ($Re \rightarrow 0$) and the mass transfer over the channel center line is close to 0.

For high velocities ($j_L + j_G = 0.64\ m/s$), different flow patterns depending on the geometry were observed, see Fig.4.21: For all geometries except ($w = 400\ \mu m$, $r = 1\ mm$) the inner vortex is strongly shifted to the back whereas the outer vortex moves diagonally to the front with a strong mass transfer over the channel centerline. Since the velocity profile is different to those at lower velocity rates an intensification of the mixing mechanism can be expected. For the bend design with $w = 400\ \mu m$ and $r = 1\ mm$ a new flow profile occurs. Except for a small region close to the wall, the complete slug shows one vortex over both halves with the center in the back. This velocity profile is expected to be the most efficient for fast mixing in the slug.

4.3 Phase separation on the chip

To guarantee a defined residence time or to add further process steps to one phase at the microreactor, effective phase separation on the chip is an important issue. Since separation due to gravitation will fail in microscale (see section 2.1.2), new concepts are required. As the influence of the surface tension is significant in microscale, separation should be performed by surface tension dependent forces. In the following the use of capillary forces and of different wetting properties will be discussed.

4.3.1 Capillary forces

The capillary pressure as a force leading liquid into a capillary depends on the wetting properties and the capillary sizes.

$$p_C = 2\frac{\sigma cos\Phi}{r} \tag{4.8}$$

The contact angles were first analyzed as follows: To guarantee a separation based on capillary forces, the capillary pressure must be higher than the pressure drop of the liquid flowing through the capillary. The corresponding flow rates were calculated according to Gunther et al. (2005).

Table 4.3: Measured contact angles at 20°C and atmospheric pressure

Fluid	Φ_{Si}	Φ_{PDMS}
Ethanol	30.8°	5.2°
Toluene	28.3°	10.5°
Water	110°	34.8°
20 wt% Glycerol in water	105°	42.4°
40 wt% Glycerol in water	108°	49.3°
60 wt% Glycerol in water	103°	55.4°

$$p_C > \left|\Delta p_{Sep}\right| \Longrightarrow 4\frac{\sigma cos\Phi}{d_C} > \left|-32\frac{u_C l_C \eta n}{d_C^2} - 32\frac{u_{out2} l_{out2} \eta}{d_h^2}\right| \tag{4.9}$$

with n as the number of capillaries in the separator. Increasing the capillary diameter results in decreasing capillary pressure. The pressure drop itself decreases as well. The maximum flow rate, defined at $p_C = \Delta p_{Sep}$,

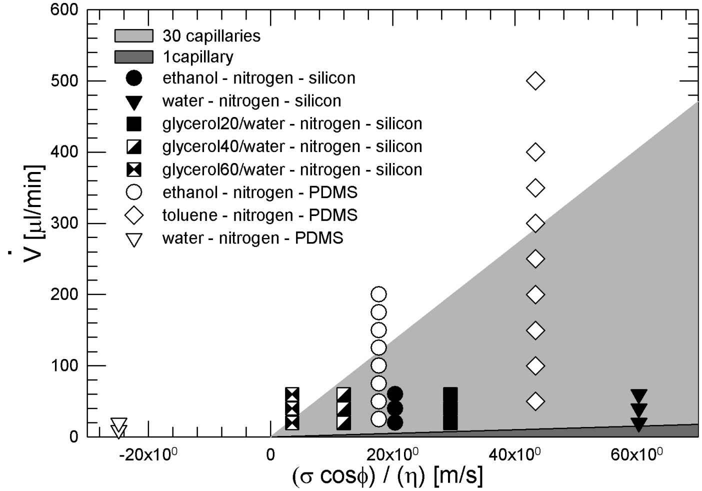

Figure 4.22: Operating capacity of the separator used (grey area) and experiments (dots).

is plotted versus fluid properties in Fig.4.22. Geometrical parameters were kept constant and are implemented in the slope.
Phase separation for the performed gas-liquid experiments in silicone reactors is (except for the very viscous 60 wt% glyerol in water) within the calculated operating capacity and worked well. In PDMS-reactors the separator worked well for organic solvents at moderate flow rates. At higher flow rates ($\dot{V}_{org} > 120\ \mu l/min$) a small amount of organic material passed the main channel exit. This agrees with the operating capacity limit as well. Differences at the breaking point for the separator occur due to measurement uncertainties of the contact angle and due to the trapezoid shape of the separating capillaries. For water-nitrogen flow in PDMS channels, the separator failed completely. This is based on the strong hydrophobic behavior of the wall material and had been predicted by the calculated capillary pressure, see Fig.4.22. The grey areas indicate the calculated working range for a separator with 1 and 30 capillaries respectively. Due to the reduced pressure drop an increase of capillaries lead to an increase of working range. The different experiments are indicated by the dots: Depending on the fluid pair and wall properties,

the separator worked either very well (water-nitrogen in Si-reactors) or failed (water-nitrogen in PDMS-reactors. The experimental observation agreed with the prediction: Whereas e.g. the ethanol-nitrogen flow was separated completely in PDMS-reactors at liquid flow rates below 100 $\mu l/min$, a significant amount of nitrogen at the liquid outlet was observed at higher flow rates.

For liquid-liquid flow separation each resistance (capillary pressure, pressure drop by flowing through the capillary, pressure drop in the channel) was calculated individually. Complete flow separation was assumed with one phase flow in each outlet. For both liquids the capillary pressure and pressure drop for each outlet was calculated. The pressure drop as resistance was calculated according to eq.4.9. The fluid passes the separator for $p_{Sep} > p_{main\ Channel}$. The results for the used design with 30 trapezoidal capillaries is plotted in Fig.4.23. The separator works acceptably well for flow rates below $\dot{V}_{org} \overset{<}{\approx} 1000\ \mu l/min$. In the experiments, 5-10% of the water was found in the organic outlet and 10% of the organic material left the reactor at the main channel outlet. Remarkably the error was about 10% higher for very low flow rates $\dot{V}_{org} \approx 20\ \mu l/min$ and diminished for intermediate flow rates. For liquid flow rates in the range of $\dot{V}_{org} > 1000\ \mu l/min$ the resistance of the separator is higher than the resistance of the main channel outlet. Experiments confirmed this prediction: at these flow rates a large amount of organic material was found at the main channel outlet. For higher flow rates ($\dot{V}_{org} > 1500\ \mu l/min$) both phases left the reactor by both exits, the separator failed totally. This also corresponds with the force balance: the pressure drop of the toluene passing the separator exit is equal to the pressure drop of the water in the main channel.

One limiting factor was pointed out above: High volumetric flow rates limit the operation area of this separation principle. Let us now consider some geometrical aspects; the diameter of the main channel and the capillary size at the separator. Increasing both parameters is advantageous for higher flow rates. If the size of the main channel increases the capillary forces and the pressure drop of the main channel exit will diminish. Both phases preferentially wet the main channel. For low flow rates some organic material passes the separator. For flow rates $\dot{V}_{org} > 1000\ \mu l/min$ the separator fails. Increasing the capillary size to decrease the pressure drop leads to negligible capillary forces, the selectivity of the separator disappears. Separation based on capillary forces works only for flow rates below $\dot{V}_{org} \overset{<}{\approx} 1000\ \mu l/min$. Continuous separa-

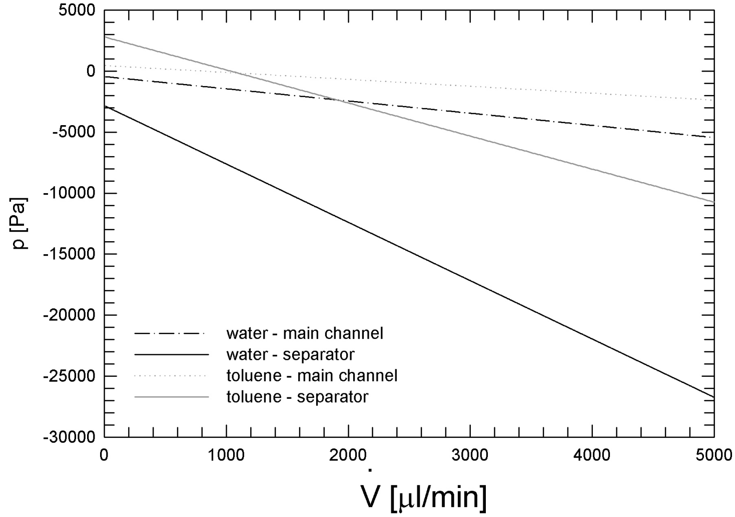

Figure 4.23: Sum of capillary pressure and pressure drop for each outlet versus different flow rates for the designed separator in PDMS for toluene-water.

tion of higher flow rates needs a different mechanism. Additionally this separation mechanism is limited to Taylor flow: if the flow is unstable and the organic material flows on the opposite side of the separator, no separation will occur.

4.3.2 Separation by different wetting properties

Since separation based on capillary forces has its limits, we want to discuss the use of selective wetting for continuous liquid separation on chip. Kashid et al. (2007) demonstrated the use of different capillaries at the outlet for an effective phase separation of Taylor flow. This mechanism, based on surface tension forces, works mainly in the microscale. As soon as gravitational forces get an impact ($Bo > 1$), flow separation by splitting will fail. For a flow ratio of $\dot{V}_{org} = \dot{V}_{aq}$ the organic outlet was free from aqueous material whereas a small amount (approximately 5...10 %) of organic material was found at the aqueous outlet. This was independent of the flow rates. An error of $\approx 10\%$ had been observed for different

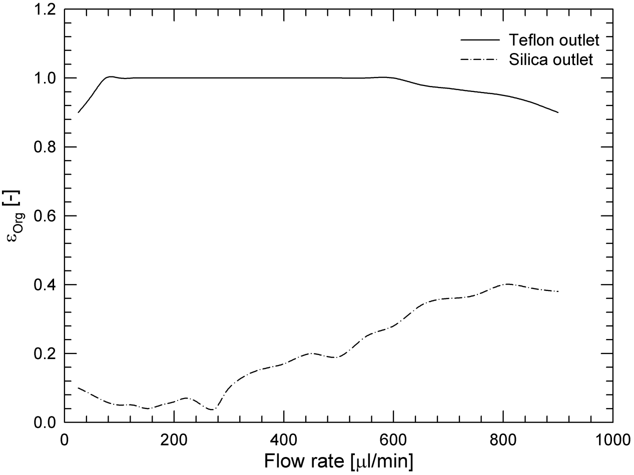

Figure 4.24: Volume fraction of organic material (toluene) in the teflon capillary and the silica capillary outlet. Flow ratio of both phases was 1.

flow rates.

To separate a liquid-liquid two-phase (Taylor) flow we used capillaries made of fused silica ($\sigma \approx 46\ mN/m$) and teflon ($\sigma \approx 18\ mN/m$). A Y-shaped exit was designed. The channel width was equal to the channel height $w = h \approx 300\ \mu m$. The capillaries with an outer diameter of $d = 360\ \mu m$ were inserted manually to the junction and fixed with epoxy. If the capillaries were inserted in a correct way (see below), phase separation was reasonably good, see Fig.4.24. Volumetric flow rates of $\dot{V}_{org} = \dot{V}_{aq} = 25...900\ \mu l/min$ were chosen. For very low flow rates of approximately 10% of organic material passed the silica outlet. Approximately the same amount of water was collected at the teflon outlet. For intermediate flow rates ($\approx 75...300\ \mu l/min$) separation was almost perfect. At higher flow rates some organic material left through the silica outlet whereas no water passed the teflon outlet. For flow rates $> 600\ \mu l/min$ a small amount of water ($\approx 10\%$) was collected in the teflon outlet.

As mentioned above, the correct placement of the capillaries is essential. Reasons for an inaccurate placement and therefore a deficient separation are:

- One capillary is placed directly at the junction and blocks the second capillary.
- The capillaries are placed at a different distance to the junction.
- The length of the capillaries is not equal thus leading to a different pressure drop.
- The cut at the capillary endings is not precise resulting in a diminished cross section.
- Due to capillary forces some glue, used to fix the capillaries, crept into the channel.

The challenges in manufacturing an outlet with different capillaries turn this separation way to a solution limited to laboratories scale.

4.4 Summary

In this chapter the influence of channel design on hydrodynamic properties was investigated. The reactor inlet as well as the channel shape and the reactor outlet were discussed.

In section 4.1 we discussed the influence of the gas inlet on gas-liquid flow characteristics in rectangular microchannels. Varying the ratio of the gas inlet width compared to the main channel width as well as changing the angle of the gas inlet showed different characteristics of the gas-liquid flow. While the gas-slug ratio is not affected by the geometry at a given volumetric flow ratio, the lengths of the gas bubble as well as of the liquid slug and thus the pressure drop change with the geometry. We observed variations of the unit cell length for a given flow ratio of factor 4.

If the gas phase is injected in the flow direction of the liquid phase ($\beta < 90^\circ$), gas bubbles are shorter than in the opposite case. This observation can be explained using the interfacial pressure at the breakup-point. Decreasing the gas inlet width at a constant main channel width also results in decreased gas bubble lengths.

The liquid slug length was found to increase with increasing liquid flow rates at constant gas flow rates. If the gas inlet has a smaller width than the main channel, the liquid slug length will be shorter compared to a gas inlet with the same width as the main channel. At a constant flow rate and constant γ, the liquid slug length divided by the channel diameter is constant.

Increasing Re either by increasing the flowrate and/or by decreasing the channel diameter results in an increasing pressure drop. Due to the recirculation in the slug, the pressure drop is also correlated to the slug length. Since the liquid slug length varies with the inlet geometry, the pressure drop increases with smaller gas inlets.

This study demonstrates that enhanced mass transfer within the liquid slugs by a short slug length ($Sh = f(L_S/w)$) can be obtained by injecting the gas phase in the flow direction of the main channel and to build a gas inlet with a smaller channel width than the one of the main channel.

Mixing in the liquid slug for gas-liquid two-phase flow was discussed in section 4.2. The mixing length could be decreased by geometrical adaptions down to 12% compared to the straight reactor design. Enhancement of the radial mass transfer in gas-liquid microreactors was achieved by introducing regular bends. For a given channel width, a smaller bend radius provides a more efficient mass transfer over the channel center line. This effect is minimized for diminishing inertia, which can be achieved by small velocity values and significant smaller channel diameters. Due to the enhanced lamellae width (and therefore diffusion times) and mixing volumes, increasing the channel width in the investigated range ($w = 200 \rightarrow 400\ \mu m$) resulted in a slightly increased mixing length. The velocity field was analyzed experimentally and theoretically. An interruption of the symmetrical recirculating profile, which is characteristic for Taylor flow, has been observed. Increase of inertia forces led to a more pronounced asymmetrical velocity profile. The inner vortex moves to the back of the slug and crosses the channel center line, while the outer vortex is splitted into two smaller vortices. Pressure drop measurements indicate a reduction of the pressure drop per mixing length of 70%.

Finally the phase separation on the chip was discussed in section 4.4. Two approaches, based on capillary forces and different wetting properties, were examined. In both cases separation efficiency strongly depends on the selected materials and on the flow rates.

If capillary forces are used, only one reactor material will be required. Manufacturing causes no problems. If a suitable combination of reactor material and fluid pairs is found, phases will be separated over a wide range of flow rates. The capacity can be increased by numbering up the individual capillaries. This mechanism fails for larger dimensions since in the range of millimeters the capillary pressure has no impact.

If $Bo < 1$, separation based on wetting properties is feasible. Using different wall properties at the outlet provides efficient separation of liquid-liquid Taylor flow. Although manufacturing is challenging, an efficient separation for a wider range of flow rates was observed. This separation principle should work in the millimeter range as well.

Chapter 5

Influence of Fluid Properties on Hydrodynamics

5.1 Influence of the liquid viscosity

The viscosity of the liquid phase is not in any case a matter of choice. Since hydrodynamic properties, such as pressure drop or velocity profile, depend on the viscosity, knowledge about its impact on the flow properties is essential for process intensification. Multiphase flow with viscous liquids occurs for liquid-liquid processes e.g. in the extraction of highly viscous oil and bitumen or extraction processes in the food industry. Typical gas-liquid processes with viscous liquids are the functionalization of polymers with reactive gases or the hydrogenation of heavy oil fraction. Additional the viscosity depends mainly on the temperature. Knowledge on multiphase flow for different viscosities can therefore be extrapolated to multiphase flow at different temperatures. This section reports on experiments done with varying viscosity in the range of $\eta = 1...10$ *mPas* by using an aqueous solution of glycerol.

5.1.1 Specific experimental setup

To guarantee a stable Taylor flow avoiding the effects of manifolds and to achieve residence times up to one minute, a new reactor based on the results presented above was needed. The microfluidic channel device consists of a 2 *m* long single channel made of silicon and glass and had been manufactured as described in section 3.1.2. The surface roughness of the dry etched channels was 0.15 ± 0.02 μm. A scheme of the microreactor is shown in Fig.5.1.

The microreactor was designed to guarantee a continuous and stable gas injection and an enhanced stable two-phase flow (Kreutzer et al.; 2006).

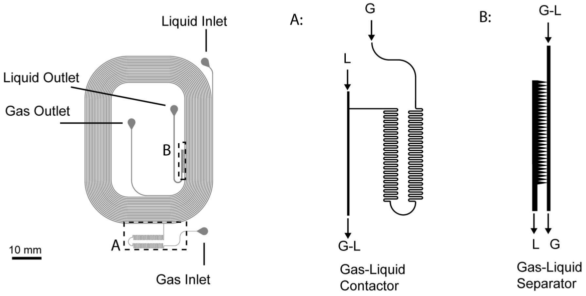

Figure 5.1: Scheme of the used reactor, in which the gas-liquid contactor and the separator provide a stable two-phase flow.

The gas inlet (Fig.5.1, detail A) with a channel width of 100 μm allows a continuous and stable injection of the gas in the liquid stream and a uniform formation of the segmented gas-liquid flow, see section 4.1. A scheme of the gas inlet is illustrated in Fig.5.1, detail B. Before the gas (nitrogen) enters the main channel via a T-junction an inlet zone of meandering channels increases the pressure drop and creates a stable gas injection. The microfluidic channel has a length of $l_R = 2\ m$ and a height equal to the width of $200 \pm 2\ \mu m$. Due to the fabrication process the height is constant over the complete chip. The curve radius is large enough to fulfill the assumption of a straight channel. The Dean Number ($Dn = Re\sqrt{d_h/R} = 3...70$, R is the radius of the curve) is small enough to prevent recirculation in the liquid slug due to centrifugal forces. The outlet equipped with a gas-liquid separator (Gunther et al.; 2005) reduces the pressure fluctuations compared to a common outlet of the gas and liquid phases by a factor of 10. The separator consists of 30 capillaries with a width of 20 μm orthogonal to the main channel, see section 4.3.1. Flow rates are in the range of $20-60\ \mu l/min$ for the liquid phase and $30-100\ \mu l/min$ for the gas phase, relevant for reactions with residence times in the order of minutes. The corresponding superficial velocities are $j_L = 0.008\ m/s - 0.025\ m/s$ and $j_G = 0.013\ m/s - 0.042\ m/s$. Physical properties of the fluids used are given in 3.2.

5.1.2 Slug length

The analysis of the slug lengths over the complete channel length showed a constant slug length, except for ethanol. In contrast to water and glyc-

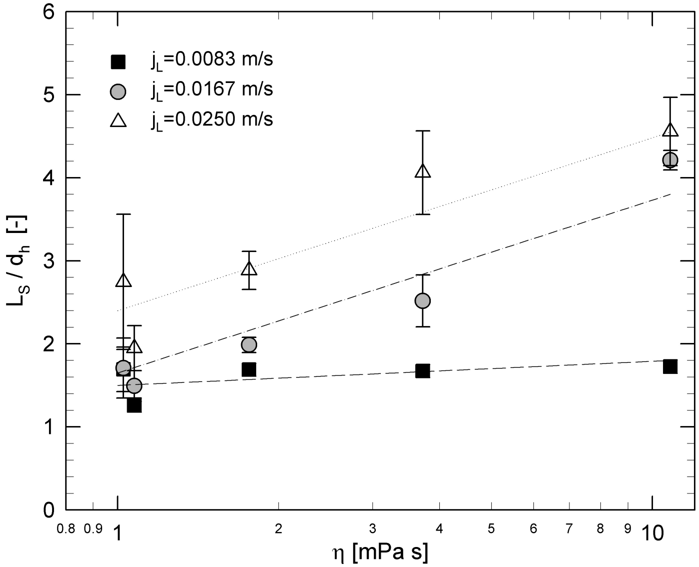

Figure 5.2: Measured slug lengths 105 *mm* behind the gas inlet. Superficial gas velocity was in all cases $j_G = 0.0416\ m/s$. Lines are best fit.

erol, the evaporation of ethanol was observed within the first 700 *mm* of the channel. For comparison reasons, we use the slug length measured 105 *mm* behind the gas inlet for the following considerations. The measured slug lengths are summarized in Fig.5.2; in general, the slug length increases with increasing superficial liquid velocity at a constant gas flow rate. At given liquid volume transport fraction values larger than 0.25 an increase in the viscosity will result in higher liquid slug lengths. Lower ε_L^*-values result in constant liquid slug lengths for increasing viscosity values. The slug lengths are not as stable as the gas bubble lengths: Standard deviations are in the range of 10%, for high liquid rates at a given gas flow rate even higher.

The viscosity of the liquid phase has a significant influence on the slug length. Higher viscosity values result in longer slugs. Since an increase of the slug length reduces the mass transfer in the slug (see section 2.3), and shorter slugs can be obtained by reducing the liquid transport fraction, the gas transport fraction should be increased for highly viscous liquids.

The long slug lengths for viscous liquids are caused by the enhanced pressure drop and the corresponding situation at the inlet: Since the pressure at the inlet section is increased, the gas is compressed. Therefore the liquid volumetric flow rate is higher than the gas volumetric flow rate at the inlet. As soon as a gas bubble is formed in the channel, a large amount of liquid is retained. After the bubble break occurs, the liquid restarts to flow and dams the gas until the pressure of the gas is high enough to interrupt the liquid flow. Due to the different volumetric flow rates, the time between gas bubble breakup and new gas bubble "growing" in the channel is longer than for less viscous liquids. Consequently longer liquid slugs are created.

5.1.3 Bubble length

The bubble length was analyzed over the complete channel length. Due to the pressure drop in the channel an elongation of the bubbles was observed. In order to verify the pressure drop as a reason for this elongation, the pressure was measured at the liquid inlet and at the liquid outlet. Note that due to the capillary at the outlet the pressure at the liquid outlet is not the atmospherical one. Assuming ideal gas behavior and neglecting turns and manifolds as pressure resistance, we calculated the gas bubble length according to the measured pressure drop and the gas bubble length close to the gas inlet:

$$p_1 \cdot V_1 = p_2 \cdot V_2 \Rightarrow p_1 \cdot L_{B,1} = p_2 \cdot L_{B,2} = p(l) \cdot L_B(l) \tag{5.1}$$

The subscripts 1 and 2 characterize an arbitrary position in the reactor. Assuming $\Delta p \sim l_R$ leads to

$$p(l) = \frac{\Delta p_{tot} \cdot l_R}{l} \tag{5.2}$$

In Fig.5.3 the measured gas bubble length L_B is plotted over the reactor length l_R for ethanol-nitrogen. Obviously the gas bubble length depends on the pressure and, for a constant superficial gas velocity of 0.042 m/s, on the superficial liquid velocity: an increase in the liquid flow rate results in a decrease of the gas bubble length. The gas bubble elongation is caused only due to the pressure drop, no coalescence was observed. The dotted lines with the calculated gas bubble length based on the measured pressure drop and eq.5.2 fit the measured bubble lengths with a correlation coefficient of 0.99. Evaporation of ethanol had no significant

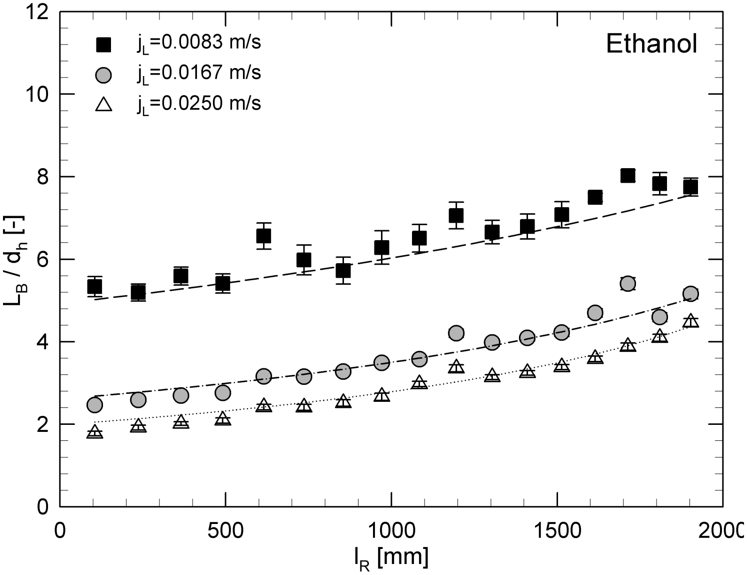

Figure 5.3: Measured gas bubble lengths for ethanol-nitrogen over the complete reactor. Lines are the expected bubble length based on eq.5.1

impact. For the other fluid pairs the same trend was observed.

In Fig.5.4 the dimensionless gas bubble length is plotted versus the viscosity at the gas inlet. An increase of the viscosity leads to decreasing bubble lengths. As discussed above the pressure drop for viscous liquids and therefore the slightly compressed gas can be considered as the main reason for the shortened bubble lengths at the gas inlet for high viscosity values. At a low liquid flow ratio, the gas bubbles are longer compared to high liquid flow rates. The measured standard deviation of the gas bubble length is in all cases around 5%, only for water as liquid phase standard deviations in the range of 10% were observed. The bubble length variation is influenced by the geometrical situation at the gas inlet. Additionally a non-pulsating liquid pump and a constant gas flow rate are the preconditions for a stable flow. The bubble breakup procedure at the gas inlet is very sensitive to small changes in the flow rate, to changes in the surface tension (Marangoni effects) and to the geometry including the wall roughness (Garstecki et al.; 2006). Since the geome-

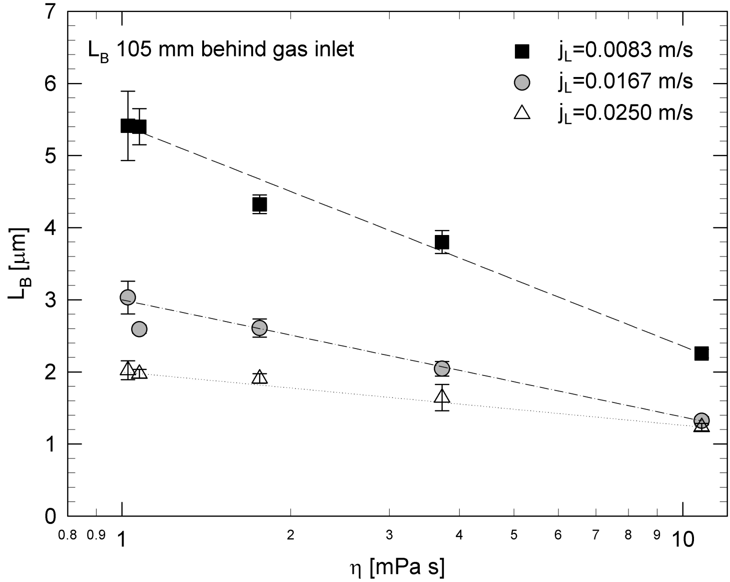

Figure 5.4: Gas bubble length versus viscosity 105 *mm* behind the gas inlet. Lines represent best fit.

try is kept constant for all experiments, the higher fluctuations for the gas bubble length for low-viscosity liquids indicate the sensitivity of the system.

In Fig.5.5. the calculated bubble length for atmospheric pressure is plotted versus the viscosity. This information is important, since the gas density at the outlet is identical for all experiments. The gas bubble length at the outlet is therefore an indication for the gas mass. It is important to note that increasing viscosity leads to an increasing gas bubble length at standard conditions. In other words, although the gas bubble length at the inlet decreases for given flow rates at increasing velocities, the mass of gas in the gas bubble increases. This is important for gas-liquid reactions.

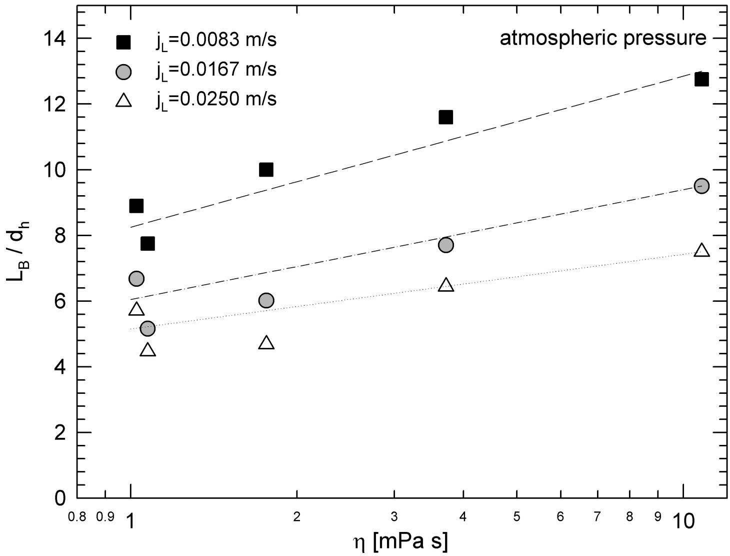

Figure 5.5: Gas bubble length versus viscosity at the reactor outlet. Lines represent best fit.

5.1.4 Pressure drop

As described in section 2.3.6, the pressure drop is caused by a) the acceleration, b) gravity and c) the surface tension. The acceleration forced pressure drop was for all measurements below 100 *Pa* (eq.2.22). The pressure drop due to gravity (eq.2.23) can be neglected due to the horizontal position of the microreactor. The pressure drop due to the surface tension (eq.2.24) is in the same range as the pressure drop due to acceleration. Therefore the pressure drop in our experiments was assumed to consist only of the frictional pressure drop (eq.2.25).

The overall pressure drop was measured between the liquid inlet and the liquid outlet. The results are shown in Fig.5.6, indicating that the pressure drop depends on the sum of the superficial velocities and on the fluid properties. Increasing the velocity leads to an enhanced pressure drop. The increase is linear to the square of the velocity. Less viscous fluids lead to smaller pressure drop values than fluids with a higher viscosity. An increase of the pressure drop is obtained by increasing the surface

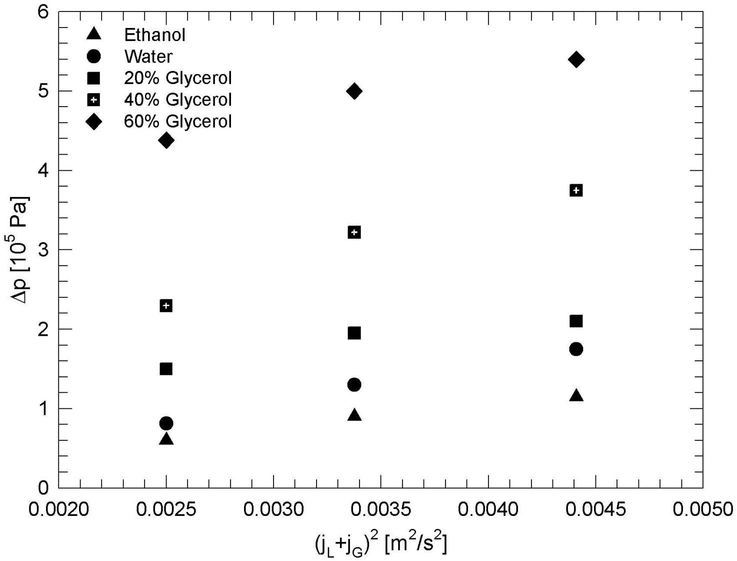

Figure 5.6: Measured pressure drop as a quadratic function of the total superficial velocity

tension. Note that these conclusions are only valid if all other parameters are constant. A change in surface tension and / or in viscosity varies the slug length, as shown in section 2.3. Due to the recirculation movement shorter liquid slugs lead to enhanced pressure drop per unit length. In Fig.5.7 the measured pressure drop values are compared with literature models, summarized in table 2.2: The homogenous model, where the friction factor is calculated by $f = 16/Re$ and the models by Bretherton (1961) and Kreutzer, Kapteijn, Moulijn, Kleijn and Heiszwolf (2005) that includes correction factors for the pressure drop due to the recirculation in the liquid slug. Obviously the one-phase model underpredicts the pressure, which is consistent with literature. The model of Bretherton (1961) describes the experimental results better than the model of Kreutzer, Kapteijn, Moulijn, Kleijn and Heiszwolf (2005). It should be noted, that the factor $\tau = 0.17$ in the model of Kreutzer, Kapteijn, Moulijn, Kleijn and Heiszwolf (2005) was found empirically for a round capillary with $d_h = 2.3\ mm$. We fitted this factor by the least square

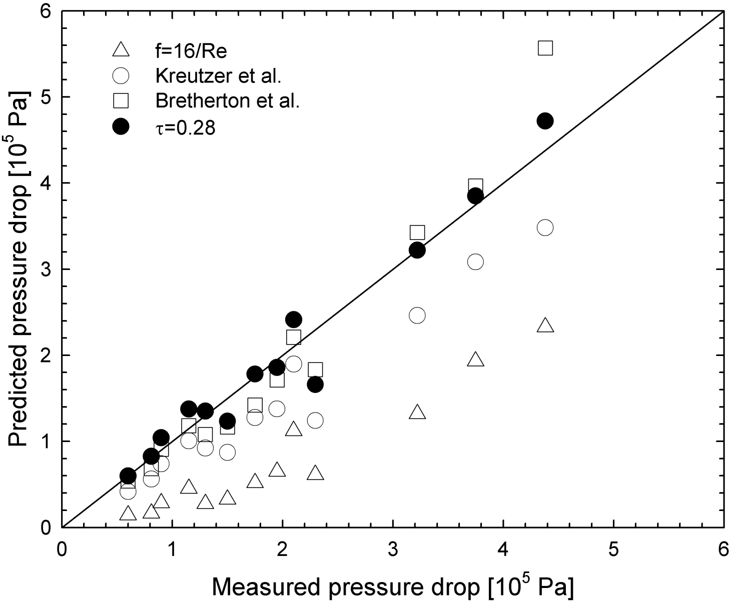

Figure 5.7: Comparison of the measured pressure drop from our experiments with models based on one-phase flow.

method and obtained the best result for $\tau = 0.28$. The underprediction of the model by Kreutzer, Kapteijn, Moulijn, Kleijn and Heiszwolf (2005) has two reasons: first, we use a rectangular channel with $d_h = 0.2\ mm$, whereas Kreutzer, Kapteijn, Moulijn, Kleijn and Heiszwolf (2005) used a circular capillary with a diameter of $d_h = 2\ mm$. The difference of the diameter by one magnitude should have no influence, as Bo is in both cases below 3 (see section 2.1.2). It is assumed that the non-constant film surrounding a bubble in a rectangular microchannel and the wall roughness, which is more important in microstructures, lead to an elevated pressure drop.

The models based on the Lockhart-Martinelli theory (eq.2.32, table 2.2) are depicted in Fig.5.8. A good fit for the models based on microchannels is observed, whereas the model developed for circular pipes in the macro scale overpredicts our measurements.

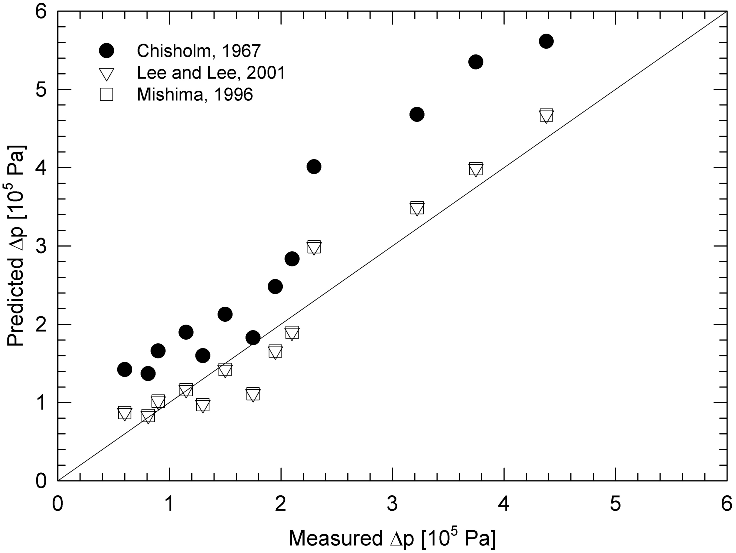

Figure 5.8: Comparison of the measured pressure drop with models based on Lockart-Martinelli.

5.1.5 Phase distribution

As can be seen in Fig.5.9, the liquid holdup at atmospheric pressure corresponds reasonably with the volumetric flow rate. The liquid holdup changes significantly when passing the reactor due to the pressure drop. The disagreement between ε_L and ε_L^* indicates a small slip which is characteristic for Taylor flow.

Additionally, the ratio of the gas bubble lengths and the liquid slug lengths can be used to characterize the flow. We consider the ratio of the gas bubble lengths to the liquid slug lengths at the reactor inlet, as illustrated in Fig.5.10. These results provide an information about the bubble breakup at the gas inlet. Due to different pressure drop values, the pressure at the inlet changes for different liquids and velocities. A clear tendency can be seen: the bubble-to-slug-length ratio depends strongly on the viscosity and the velocity rate, whereas increasing the viscosity leads to a decreasing bubble-to-slug-length ratio.

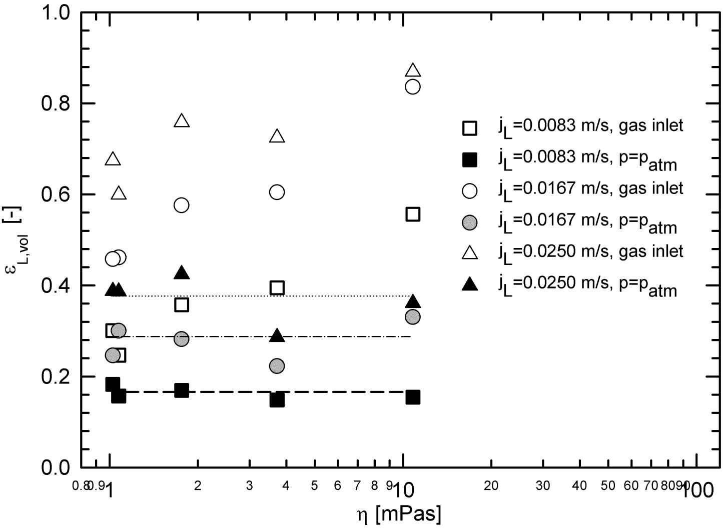

Figure 5.9: Liquid holdup versus the viscosity. The superficial gas velocity was in all experiments 0.0416 m/s. Lines indicate the liquid volume transport fraction ε_L^*.

5.1.6 Velocities

Bubble velocities were analyzed by high-speed recordings at a frequency of 3000 Hz. The results are plotted in Fig.5.11 versus the sum of the superficial inlet velocities at inlet conditions. Obviously the measured velocity gives slightly higher values than the corresponding superficial inlet velocity, indicating a small slip as mentioned above. An exception must be made for the flow of 60% glycerol for superficial liquid velocities of $j_L = 0.0167$ m/s and $j_L = 0.025$ m/s. As mentioned before, the flow properties for these two experiments were different to the experiments at lower viscosities. The higher measured bubble velocities compared to the superficial velocities indicate that the effective channel area available for the gas phase is smaller than the total channel area. This means that a liquid film with a lower velocity covers a part of the channel. The result indicates that the bubbles move faster than the liquid slugs.

Based on the measured gas bubble and liquid slug length and the velocity

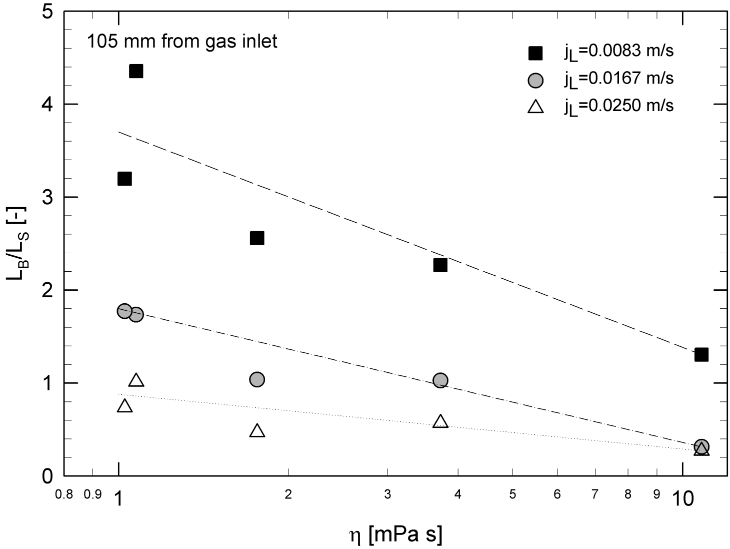

Figure 5.10: Bubble-to-slug ratio 105 *mm* behind the gas inlet for different velocity rates. The superficial gas velocity was in all experiments 0.0416 m/s. Lines are best fit.

values, the slip can be estimated based in eq.2.7:

$$s = \frac{u_L}{u_G} = \frac{t_L}{t_G} = \frac{\varepsilon_L^* \varepsilon_G}{\varepsilon_G^* \varepsilon_L} \tag{5.3}$$

This leads to the following estimation of the liquid residence time:

$$t_L = \frac{1}{l_R} u_G s \tag{5.4}$$

Let us consider a given volumetric flow ratio $(\varepsilon_L^* = 1 - \varepsilon_G^* = const.)$ for a given reactor length $(l_R = const.)$ with increasing liquid viscosity: The slip on the inlet will be in the range of $s \approx 0.1$ whereas the situation at the reactor outlet will not be affected significantly $(\varepsilon_L^* \approx \varepsilon_L$ and $s \approx 0.9...0.95)$. This means for long reactors, such as the investigated one, that for highly viscous liquids the average slip is much lower than 1 and therefore the residence times of the liquid phase are significantly lower than the mean residence time $t_{Res} = \dot{V}_L \varepsilon_L^* l_R$. Residence time measurements for viscous liquids in long microreactors are mandatory.

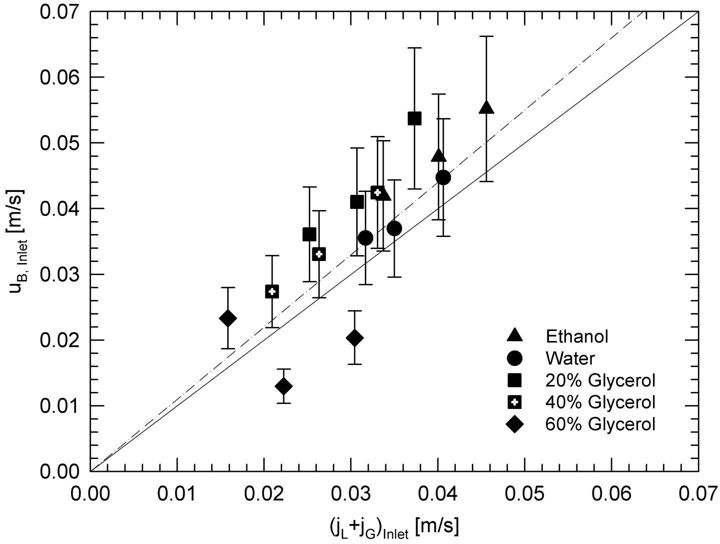

Figure 5.11: Measured bubble velocity versus the superficial inlet velocity. The straight line indicates $u_B = j_G + j_L$, the dotted line $u_B = 1.1\ (j_G + j_L)$.

5.2 Varying the gas density

Gas-liquid processes are often performed at higher pressure values to benefit from the increased mass transfer. Additionally, high pressure values are applied to shift the multiphase process to one phase either by applying supercritical conditions or by the changes of vapor pressure. To investigate the influence of pressure (and therefore of the gas density) on Taylor flow we used channels made of silicon-glass (see chapter 3.1.2). The experimental setup was built as described in section 3.2.2, flow characterization was performed by LIF-measurements.

5.2.1 Flow regimes

To identify the flow pattern transition areas, we recorded 200 LIF-pictures for every velocity combination in the range of $j_G = 0.08...1.04\ m/s$ and $j_L = 0.02...0.6\ m/s$. The flow regime map for the investigated system can be seen in Fig.5.12. The flow pattern for each velocity pair was

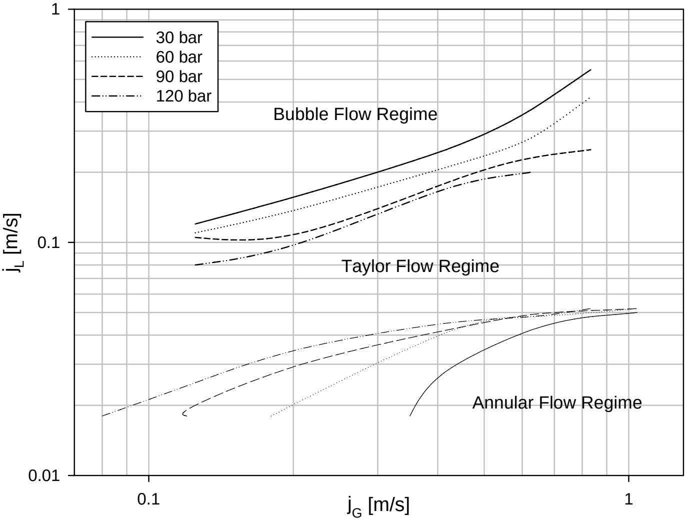

Figure 5.12: Flow regime map for the analyzed system (water-nitrogen).

assigned by the Matlab-programme:

- *Bubble flow regime:* more than 90% of all detected bubbles had a length of $L_B < 1.1\ w$.
- *Taylor flow regime:* Liquid slugs in the range of $0.5 < L_S < 5\ w$ were detected and the bubble length was $1.1 < L_B$. Since the FOV was limited, bubbles larger than $L_B > 1200\ \mu m$ were not detectable.
- *Annular flow regime:* No liquid slugs were observed. A gas bubble length could not be determined.

At increasing pressure values the Taylor flow regime gets smaller, whereas the bubbly flow regime occurs at lower liquid velocities at a given gas velocity. Potentially, at very high pressure values ($p > 200\ bar$) the Taylor flow may diminish. The annular flow regime transition shifts for a given liquid velocity to smaller gas velocity values. This result is surprising, since an increase of pressure effects only the gas density and therefore the inertia. Surface tension and viscosity of the liquid phase remain more or less constant, see table 3.3. Consequently Bo, Ca and We_L stay constant for increasing pressure values. We_G increases for given velocity values by a factor of 123 from atmospheric conditions to $p = 120$ bar.

Let us first consider the transition between Taylor flow and annular flow. As described above, the changes in gas bubble shape play a role in the formation of Taylor flow. For a given liquid superficial velocity of $j_L = 0.03$ m/s the increasing inertia of the gas phase at increasing pressure impedes the gas bubble to break up. The resulting gas bubbles are therefore elongated until the annular flow regime is achieved; the transition shifts towards lower gas velocities.

The same effect occurs at the transition between Taylor flow and bubble flow. The formation of gas bubbles has two steps: First the flow of the gaseous phase into the main channel and then the distortion of the growing bubble / droplet in flow direction. The first step can be facilitated by higher gas densities. For low gas velocities and high liquid flow rates the liquid phase is dammed and increases the pressure, resulting in a bubble breakup. Since at elevated pressure values the gas penetrates more easily into the main channel, the liquid pressure remains in the same range and the transition from Taylor to bubble flow will move to lower liquid velocities at a constant gas velocity.

5.2.2 Gas bubble length

An important parameter in the Taylor flow regime is the length of the gas bubbles. Fig.5.13 illustrates the measured gas bubble length divided by the channel width for different superficial liquid velocities at various pressure values. As known from investigations at atmospheric pressure, increasing the superficial liquid velocity at a constant superficial gas velocity results in decreasing gas bubble length. In the investigated range no bubbles shorter than three times the channel width were observed. This depends on the selected flow range as well as on the gas inlet design. For increasing pressure increasing gas bubble lengths were observed for constant flow conditions. Note that for $p = 120$ bar at the lowest liquid velocity no complete gas bubbles were recorded, indicating a gas bubble length larger than the FOV. As presented above (see Fig.5.12), the transition from the Taylor flow to the annular flow regime was reported to change to lower gas velocity values at a given liquid velocity. Hence the observed elongation of bubbles at given superficial velocity values and increasing pressure evidences this shift of the transition regime. Further increase of the liquid flow rate leads to bubble flow.

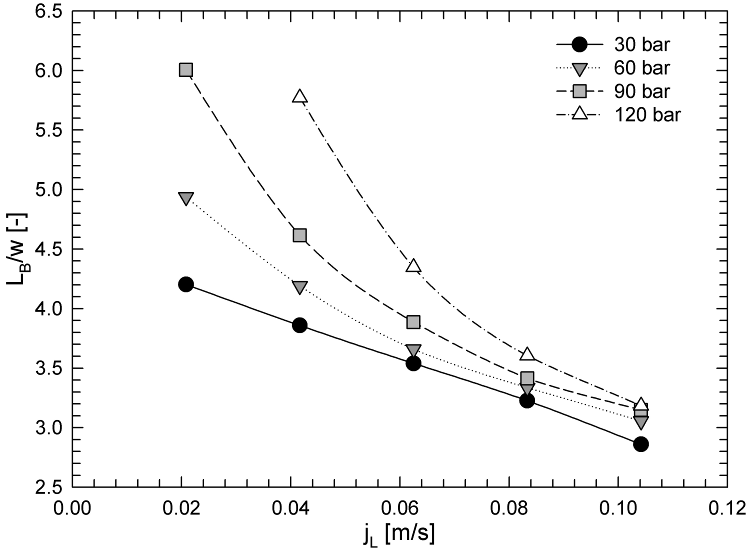

Figure 5.13: Bubble length versus superficial liquid velocity and system pressure at a constant gas velocity of $j_G = 0.125\ m/s$ for water-nitrogen.

The elongation of the gas bubbles at increasing pressure is mainly due the stronger influence of inertia: If the pressure increases at constant velocity rates, Re_G, calculated with the sum of both superficial velocities, will increase significantly (for $j_L = 0.02\ m/s$ and $j_G = 0.125\ m/s$, Re_G changes from 552 for $p = 30\ bar$ to 867 at $p = 120\ bar$). Since Ca increases as well (e.g. from 0.0022 to 0.0032 at $j_L = 0.02\ m/s$ and $j_G = 0.125\ m/s$), the surface forces diminish slightly compared to the viscous forces in the liquid phase. The dominating increase of gas inertia leads to a delay of the bubble breakup in the gas inlet zone. The influence of the thicker film at elevated pressure, resulting in a slight decrease of the cross sectional area and therefore in an elongation, can be regarded as marginal: since the film thickness increases from $f \approx 11\ \mu m$ at 30 bar to $f \approx 15\ \mu m$ at 120 bar, elongation of a 840 μm long gas bubble at 30 bar ($j_L = 0.02\ m/s$ and $j_G = 0.125\ m/s$) would lead to a gas bubble length of 880 μm.

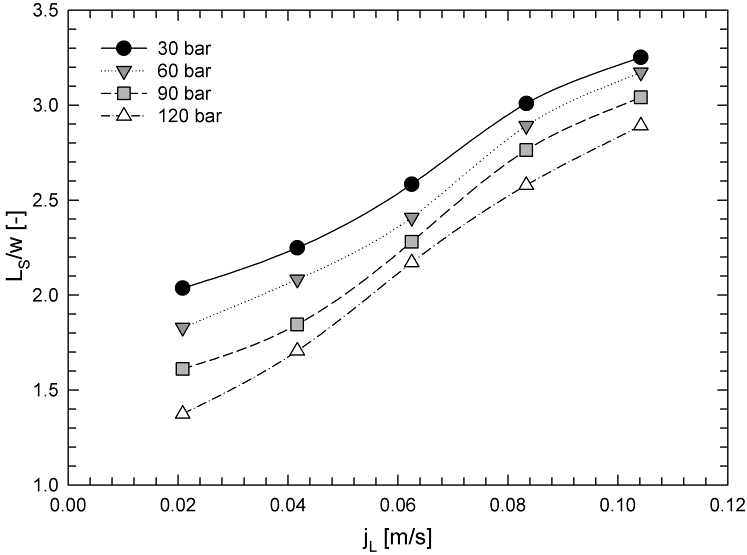

Figure 5.14: Slug length versus superficial liquid velocity and system pressure at a constant gas velocity of $0.12\ m/s$ for water-nitrogen flow.

5.2.3 Slug length

Equivalent to the gas bubble length we analyzed the length of the liquid slugs. In Fig.5.14 we present the liquid slug length divided by the channel width versus the superficial gas velocity and the pressure. The superficial gas velocity was kept constant at $j_L = 0.125\ m/s$. Corresponding to the experiments at atmospheric pressure, an increase of the superficial liquid velocity leads to an elongation of the liquid slug.

Concerning the influence of pressure, the opposite trend than observed for the gas bubbles appears: Increasing the pressure at constant flow rates leads to a decrease of the liquid slug length up to 65% of the value for $p = 30\ bar$. This effect is more pronounced for low liquid velocities. Note that for $p = 120\ bar$ and $j_L = 0.02\ m/s$ significantly less slugs were recorded than for the other experiments, which again indicates the transition to the annular flow regime.

Since ρ_L does not depend significantly on the pressure, no change in inertia occurs as observed for the gas phase. The slight decrease in

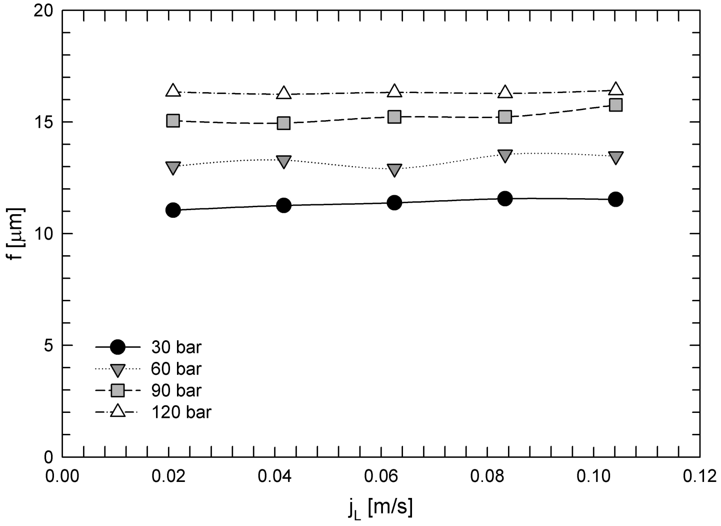

Figure 5.15: Film thickness between the gas bubble and the channel wall at a constant gas velocity of 0.12 m/s

surface force does not explain the shortening of the slugs. The shortening of the slugs can rather be explained by the mass balance: The increase of film thickness results in shorter slugs.

It is important to note that mass transfer in the slugs is more intense for shorter slugs. The antisymmetrical recirculation in the slugs provides faster mixing for shorter slugs (see section 2.3). In the range of $L_S/w < 10$ this effect is more pronounced for high Re.

5.2.4 Film thickness

Analyzing the liquid film thickness between the gaseous core and the channel wall resulted in a constant film thickness for all flow rates at a given pressure value. Increasing the pressure results in an increase of the film thickness, see Fig.5.15.

As discussed on page 17, the film thickness depends mainly on Ca. Since increasing the pressure results in increased viscosity and decreased surface tension, Ca increases as well. Since the influence of the wetting properties diminishes and viscosity effects are more important for high pressure values, the film thickness increases in this case. Note that an increased film thickness leads to an increase of the bubble velocity. Therefore Ca is slightly higher for high pressure values but stays in the order of $Ca = 0.002...0.004$. The increased influence of the inertia forces leads to the assumption that for high pressure microfluidics the film thickness is correlated not only to Ca as it was done in previous investigations for microfluidics at atmospheric pressure.

5.2.5 Phase distribution

An important parameter to compare the gas-liquid phase distribution is the ratio of the bubble length to the slug length. Fig.5.16 shows the ratio of the gas bubble length to the liquid slug length depending on the superficial liquid velocity for different pressure values. Note that the value for $p = 120\ bar$, $j_L = 0.02\ m/s$ is not plotted because no gas bubble lengths were recorded.

According to the results above, L_B/L_S increases with the pressure. In general, the ratio L_B/L_S is at its maximum at the transition from Taylor flow to annular flow for low liquid velocities. If the liquid velocity is close to the superficial gas velocity, the ratio L_B/L_S equals 1 and marks the transition to the bubble flow regime. In this range, the difference between the different pressure values is negligible. Note, that for $p < 120\ bar$ the ratio L_B/L_S is smaller than the one of the flow rates, indicating different velocities and residence times of the liquid and the gas.

Parallel to the ratio of the gas to the slug length, the sum of both can be considered. Investigations done by Sengupta (2006) and by our own group lead to the assumption that the sum of the gas and the liquid phase length ("unit cell length") is constant for a given reactor geometry. In Fig.5.17 the sum of the gas bubble length and the liquid slug length is plotted versus the superficial liquid velocities for different pressure values. For the Taylor flow regime a constant unit cell length of $\approx 6w$ was observed. As soon as the flow characteristics are close to annular flow, this is no longer valid. The unit cell length increases mainly due to the strongly elongated bubbles. This change occurs for high pressure values ($p = 120\ bar$) at relatively high liquid flow rates. The unit cell length is an important value, since it provides information on the frequency of the two-phase flow. It was explained for catalytic active walls that the selectivity of the catalyst depends on the wetting frequency. As shown in

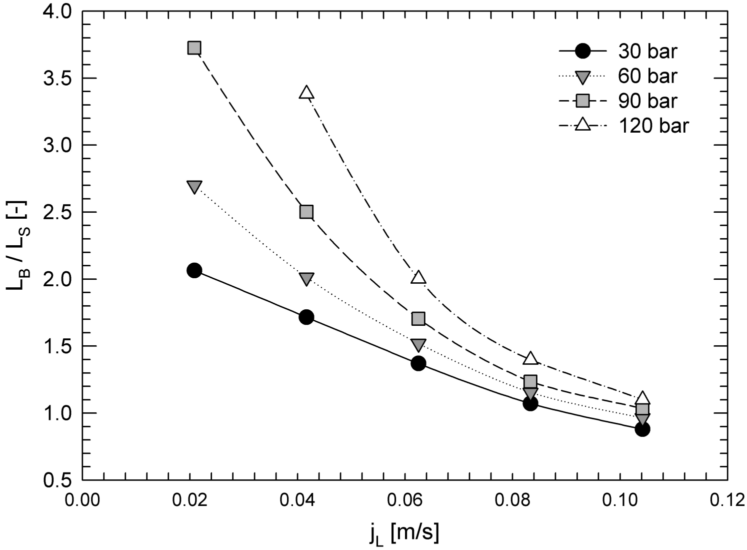

Figure 5.16: Ratio of bubble to slug length versus the superficial gas velocity for different pressure values

section 4.1 the unit cell length can be influenced by the inlet geometry. An important parameter in gas-liquid two-phase flow is the distribution of the phases. This can be expressed by the liquid holdup ε_L. Note that the liquid holdup consists of the liquid phase in the film and the liquid phase in the slug. In analogy to the termini in a packed bed, the liquid holdup in the film ε_F is called "static" holdup, whereas the liquid in the slug is named the "dynamic" holdup. Fig.5.18 illustrates the total liquid holdup, ε_L (black symbols), the "dynamic" liquid holdup in the slugs ε_S (grey symbols) and the "static" liquid holdup in the film, ε_F (dark grey symbols). The holdup values were calculated by analyzing the liquid film thickness using

$$\varepsilon_F = 2\frac{f}{d} \tag{5.5}$$

and the gas bubble and slug length by

$$\varepsilon_S = \frac{1-\varepsilon_F}{L_B/L_S+1} \tag{5.6}$$

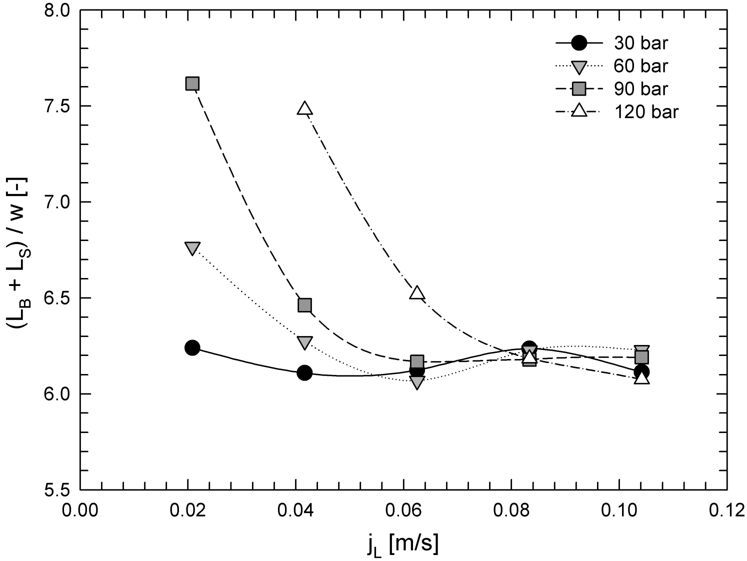

Figure 5.17: Sum of bubble and slug length versus the superficial gas velocity for different pressure values

and

$$\varepsilon_L = \varepsilon_F + \varepsilon_S \tag{5.7}$$

Since the gas bubble length is defined by the maximum elongation of the gas phase in the center of the channel, the gas holdup is slightly overestimated.

In general, the liquid holdup increases at increasing superficial liquid velocity. For all velocities, the total liquid holdup is higher than the volume flow ratio: For the liquid superficial velocity of $j_L = 0.021 m/s$ the total liquid holdup reaches a value of 0.35...0.4, whereas the volume flow ratio of liquid to gas phase is 1:6. This "high" holdup value leads to an increased residence time compared to the mean residence time calculated by

$$t_{Res} = \frac{V_{Reactor}}{\dot{V}_L + \dot{V}_G} \tag{5.8}$$

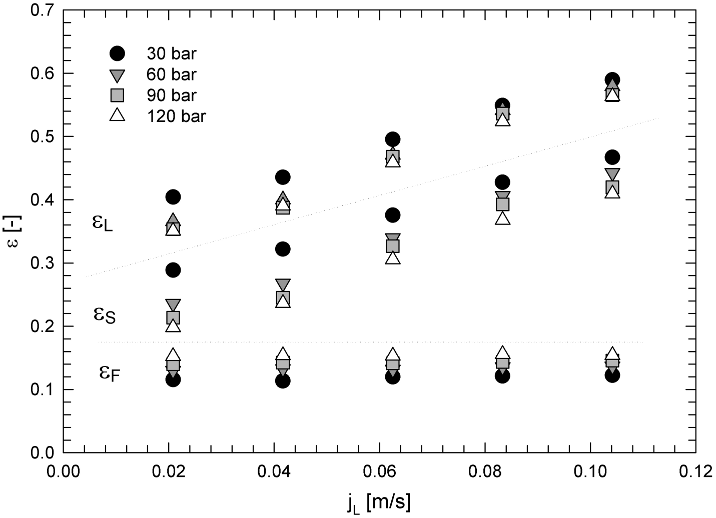

Figure 5.18: Holdup values for varying pressure values and superficial liquid velocities at a constant superficial gas velocity of 0.12 m/s

This means that the real gas velocity is higher than the superficial gas velocity, whereas the real liquid velocity is smaller than the superficial one. This can be observed for all investigated flow rates and is in consistence with the literature on Taylor flow, see section 2.3.
The "static" liquid holdup in the film shows no tendency when changing the liquid superficial velocity. This is consistent with the film thickness at varying pressure and velocity values, see Fig.5.15. Increasing pressure results in increased holdup in the film. As for the film thickness, the effect of pressure and therefore of the viscosity-to-surface tension-ratio is more pronounced than the effect of the velocity.
For the "dynamic" holdup in the slugs, the effect of pressure is in the same order as the effect of velocity. Increasing the velocity of the liquid phase results in increased "dynamic" holdup, but the effect is not as strong as it can be expected from the ratio of the superficial velocities of both phases. This was discussed for the total liquid holdup. Obviously an elevated pressure leads to a decrease of the dynamic holdup and thus to a shorter residence time of the liquid phase. This would have to be

proved experimentally in further studies.

5.2.6 Bubble velocity

An important parameter to characterize gas-liquid two phase flow is the real velocity of the gas bubble. In section 5.2.5, where the liquid holdup was investigated, we observed an increase of the gas holdup at increasing pressure. The analysis of the liquid holdup led to the assumption that the real velocity of the gas bubbles is larger than the sum of the superficial liquid and superficial gas velocity. Fig.5.19 illustrates the measured and the calculated gas bubble velocity. For the measured gas bubble velocity, two photographs with a time delay of 100 μs were analyzed. The movement of the gas bubble front and of the gas bubble tail were analyzed and divided by the time delay of the second exposure. The lines in Fig.5.19 are the sum of the superficial velocity values and some multiples of it.

The increase of the gas bubble velocity at elevated pressure is caused by the larger film thickness and therefore by the decreased width of the gas bubbles and by the transition to the annular flow regime. Shorter slugs and longer bubbles, as observed above, facilitate the velocity difference of both phases. Based on these results we state that the residence time distribution for the liquid phase has a wider shape for high pressures. The axial mixing is enhanced; improved ”communication” between the slugs occur. Liquid material of the slug is pushed into the film at the bubble front and leaves the film after the bubble has passed. To verify this hypothesis, residence time measurements should be performed.

5.2.7 Pressure drop

The measured pressure drop for a gas velocity of $j_G = 0.12\ m/s$ is depicted for all four pressure values and all liquid velocities in Fig.5.20. Note that the pressure drop was measured over the microreactor and the connection capillaries. The dominating effect is the liquid flow rate: increase of the superficial liquid velocity leads to an increase in pressure drop. This corresponds to the theory explained in section 2.3. Additionally, the pressure drop decreases for increasing pressure values.

As described in eq.4.4, the pressure drop depends on the velocity, the liquid holdup, Re, the liquid slug length and Ca. This equation is valid

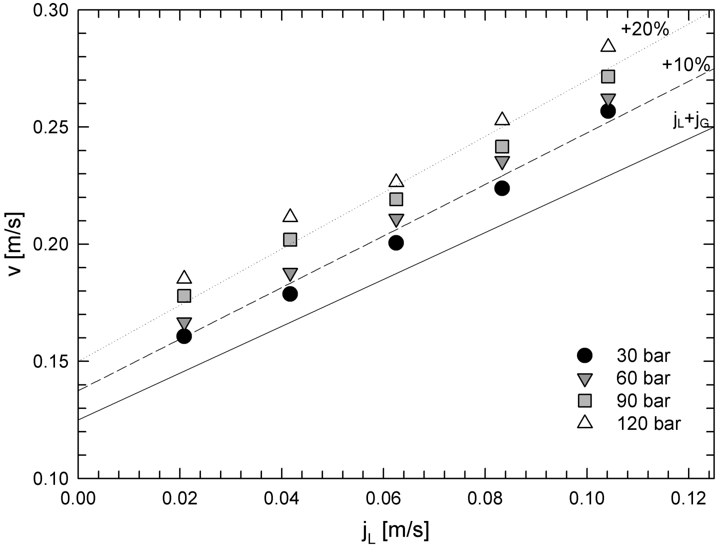

Figure 5.19: Measured bubble velocities at a constant gas velocity of $0.12\ m/s$. The straight line indicates the sum of the superficial velocities. Dotted lines are multiples as indicated.

for Taylor flow and, with some small faults, for the bubbly flow regime as well. For annular flow it is not valid, since both phases are continuous and the pressure drop due to the recirculation in the liquid slug is missing. Since at elevated pressure values the slug length decreases for given velocity values and the transition to annular flow shifts to higher liquid flow rates, the decreased pressure drop at higher pressure values is consistent with the theory.

5.3 Summary

We discussed the influence of fluid properties on hydrodynamics. The viscosity of the liquid phase was varied as well as the gas density. Reactors of silicon/glass were used.

The influence of liquid viscosity ($\eta = 1...10\ mPas$) was characterized for

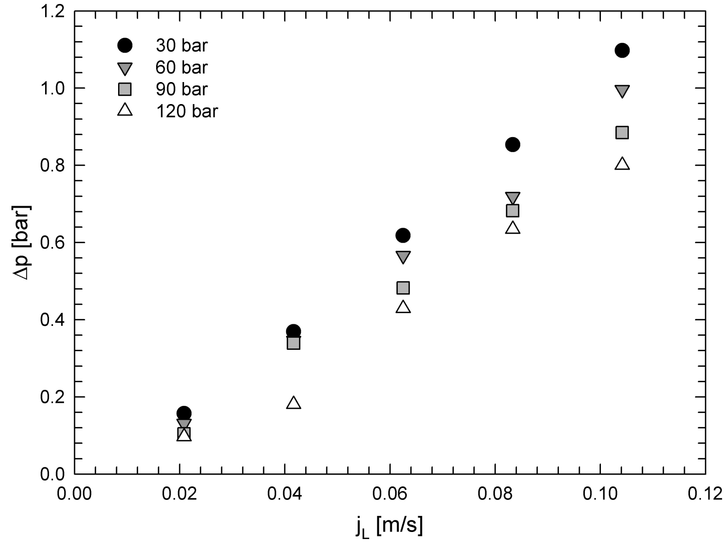

Figure 5.20: Pressure drop of the system for water-nitrogen flow at a constant gas velocity of 0.12 m/s.

the Taylor flow regime in a 2 m long rectangular microchannel using optical methods and pressure drop measurements. The microchannel was designed for minimal disturbance of the sensitive flow by the inlet and outlet.

The liquid slug length increases with increasing viscosity. This effect is more pronounced for higher liquid velocities at constant gas velocity. The slug length varies between $O(d_h)$ for low viscosity and velocity and $O(4d_h)$ for high viscosity and velocity.

At constant pressure the bubble length increases with increasing viscosity, whereas higher liquid velocities lead to decreasing gas bubble lengths. The pressure drop was correlated with different models. Best agreement was obtained with the correlation of (Bretherton; 1961). An adapted correlation for the friction factor based on the model of (Kreutzer, Kapteijn, Moulijn and Heiszwolf; 2005) was presented. The liquid holdup varies significantly along the channel length due to the pressure drop.

A long channel is required for slow chemical reactions as well as for ne-

glecting the effects of manifolds at the inlet and the outlet. A tradeoff between the pressure drop and the reactor length is mandatory.
The bubble velocity was found to be about 10% higher than the sum of the corresponding superficial velocities. This margin is due to the liquid film.

We investigated the flow regime for different gas densities and for Taylor flow the liquid slug length, gas bubble length and film thickness for pressures between 30 bar and 120 bar. The results can be summarized as follows:

- At elevated pressure and constant velocities, the pressure drop of the two-phase flow decreases.
- The gas bubble length increases at higher pressure values.
- The liquid slug length decreases at increasing pressure.
- The ratio of the gas bubble length to the liquid slug length increases at higher pressure values. At high liquid velocities (1 m/s) this effect is less pronounced than for low liquid velocities (0.2 m/s)
- The film thickness increases at higher pressure values.
- The bubble velocity increases for given flow rates at increasing pressure. This is caused by the increased film thickness and indicates an enhanced axial mixing.

These results allow in a further mass transfer analysis the determination of

- the degree of axial dispersion between neighboring liquid slugs through the film;
- the gas-liquid-interfacial area for gas-liquid mass transfer and
- the mass transfer through the liquid film to the wall in case of catalytic reactions.

Further investigations should focus on the velocity profile in the liquid film by μ-PIV and residence time measurements.

Chapter 6

Use of specified Flow Properties for intensified Mass Transfer

6.1 Absorption of CO_2 in alkaline solution

The verification of the influence of optimized hydrodynamics on gas-liquid mass transfer needed a suitable test reaction. To reduce the realization on engineering aspects, some specific properties were required: The reaction should take place without a catalyst to avoid both the challenges of creating a catalytically active wall (Waelchli; 2005) or a perturbance of the flow properties by the packed bed. The reaction had to be mass transfer limited. If possible, reactors made of PDMS were desired. This includes the matter of reaction condition (ambient temperature and pressure) and chemical properties (swelling by organic solvents, wetting properties or etching). Due to the precise documentation, absorption of CO_2 in alkaline solution was selected. As alkaline solution, ethanolamine and sodium hydroxide dissolved in water were found to be best documented and suitable.

First experiments were conducted with ethanolamine due to the fact of its solubility in a mixture of ethanol/water. Hence the liquid phase was expected to be the continuous one and therefore a flow pattern according to chapter 4 and chapter 5 was assumed. To increase the wettability and to achieve a stable flow, we used a mixture of water, ethanol and monoethanolamine. Since the kinetic data in literature were obtained for aqueous solution, they could not be conferred on our experiments. If the concentration of water was increased to literature values, the contact angle to PDMS increased to values of $\Phi > 90°$ and the flow was not as defined as expected. Additionally ethanolamine is a weak base and no direct conclusions could be drawn from the pH to the concentration of OH^-. In contrast, for aqueous solution of sodium hydroxide the relation between pH and OH^- and therefore of absorbed CO_2 is known. Hence, we used aqueous solution of sodium hydroxide to investigate the mass transfer in microchannels for gas-liquid flow.

6.1.1 Specific literature review and fundamentals

The absorption of CO_2 into an aqueous solution of sodium hydroxide had been chosen as a fast test reaction to investigate the gas-liquid mass transfer in microchannels. This chemisorption is well documented (Danckwerts and Sharma; 1966; Stumm and Morgan; 1995; Fleischer et al.; 1996). Depending on the pH, two different reactions steps were reported:

$$CO_2^L + OH^- \leftrightarrow HCO_3^- \tag{6.1}$$

$$HCO_3^- + OH^- \leftrightarrow CO_3^{2-} + H_2O \tag{6.2}$$

Both reactions are reversible and exothermic in the forward direction. In alkaline solution both reactions occur very fast, reaction 6.2 can be considered as instantaneous. The rate controlling step is the absorption of gaseous CO_2 into the liquid phase. The equilibrium of these reactions depends on the pH. With varying pH, the amount of carbonate and bicarbonate ions changes. The equilibrium has been summarized by Stumm and Morgan (1995) and Fleischer et al. (1996) and is depicted in Fig.6.1. For $pH > 11$ the equilibrium is for both reactions on the right side. Since reaction 6.2 occurs instantaneously, mainly carbonate ions exist in the liquid phase. For $pH < 11$ the equilibrium of reaction 6.2 shifts towards the left side. Consequently carbonate ions are oxidized to bicarbonate ions. At a $pH \approx 10.3$ carbonate and bicarbonate ions exist at equal amounts. For $pH < 7$ physisorption of CO_2 plays a significant role.

This chemisorption can be considered from a progressive point of view as well: In the beginning, an aqueous solution of sodium hydroxide is provided. The pH depends on the concentration and is for $c = 0.1\ M$ in the range of 12.8. As soon as gaseous CO_2 is brought into contact to the liquid phase and physically absorbed into the liquid phase, CO_2^L is available as educt for reaction 6.1. The generated bicarbonate ion acts as educt for reaction 6.2. The decrease of OH^- leads to a decrease of the pH and therefore of the equilibrium. Hence, the measured pH and the corresponding amount of consumed OH^- gives information of the

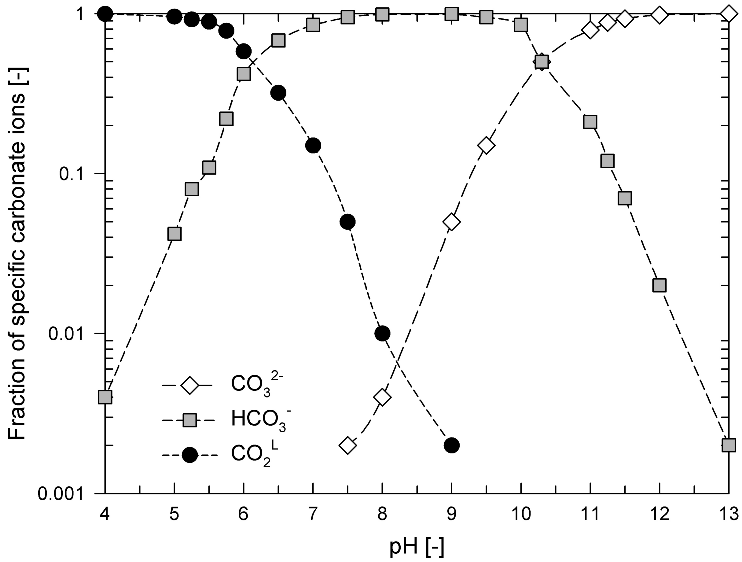

Figure 6.1: Equilibrium values of carbonate species in dependence of *pH* (Stumm and Morgan; 1995)

absorbed CO_2.

In preliminary batch experiments CO_2 was introduced by a capillary into a beaker filled with aqueous solution of sodium hydroxide. The *pH* was measured in dependence of the time. These experiments differed in the concentration of *NaOH* and in the flow rate of CO_2. Experiments were performed with and without magnetic stirrer. In all experiments the *pH* decreased, indicating two inflection points at $pH \approx 11.5$ and $pH \approx 8$. These *pH* values correspond with the change of reaction progress, see above. If turbulence was introduced by stirring, the changes in *pH* took place in a shorter time. Hence the chemisorption can be considered as mass transfer limited in this specific case. As expected, increase of the gas flow rate and decrease of the sodium hydroxide concentration resulted in a faster reaction progress.

Due to the well described reaction system and the fast kinetic, absorption of CO_2 in sodium hydroxide is a common test reaction for gas-liquid microreactors. Numerical and experimental results for a falling film microreactor were presented by Zanfir et al. (2005); Al-Rawashdeh et al.

(2008). Mass transfer coefficients in the range of $4 \cdot 10^{-4} ... 10^{-3}$ m/s and the dependence of overall volumetric mass transfer coefficients on the channel width were reported (Claudel et al.; 2005). For Taylor flow in rectangular microchannels, Yue et al. (2007) determined overall volumetric mass transfer coefficients in the range of $k_L a = 0.6...11$ $1/s$. The corresponding mass transfer coefficients of about 10^{-3} m/s are in the same range as those reported for a different flow regime in microreactors by Claudel et al. (2005).

6.1.2 Influence of flow pattern

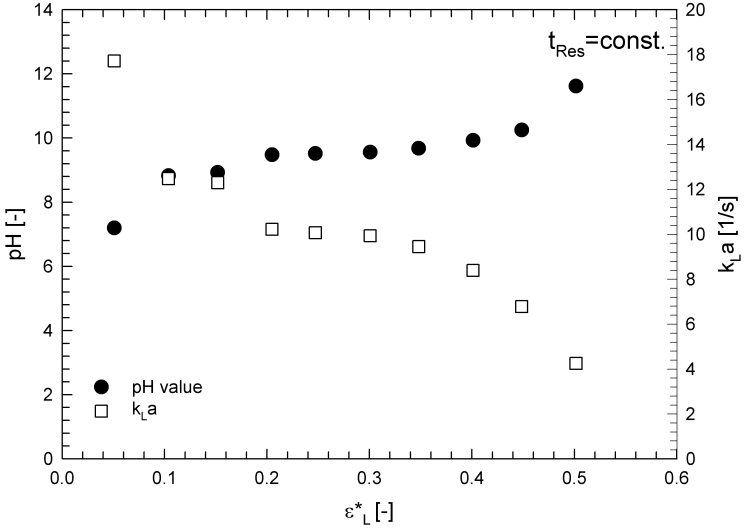

Figure 6.2: Measured pH and corresponding $k_L a$ values for a given mean residence time and varying ε_L^*.

The influence of the volume transport ratio and therefore of the flow pattern was investigated for a constant mean residence time of $t_{Res}^{Mean} = 0.1$ s. For $\varepsilon_L^* = 0.15...0.4$ Taylor flow with different gas bubble lengths was established at the reactor inlet. The length of the gas bubbles differed. At $\varepsilon_L^* = 0.5$ bubbly flow was detected; for $\varepsilon_L^* < 0.15$ stratified flow was observed. In these experiments the flow rate based mean residence time

may differ from the real residence time of the liquid phase.
The measured *pH* as well as the calculated overall mass transfer coefficient versus the volumetric transport ratio are illustrated in Fig.6.2. The *pH* values are given at the right axis and are symbolized by black circles whereas the $k_L a$ values are symbolized by white squares; The corresponding ordinate is the left one. Considering the *pH* value, two inflection points at $pH \approx 8$ and $pH \approx 11$ were detected in congruence with the batch experiments. Since these inflection points occur at the transition to a new flow pattern, the mass transfer from the gas to the liquid phase must depend on the interfacial area and on the flow pattern. For the Taylor flow regime in the range of $\varepsilon_L^* = 0.15...0.4$ increasing ε_L^* leads to a slight increase of *pH*. Since the residence time can be considered to be constant in this regime, elongation of bubble length and increasing excess of CO_2 lead to a decrease of *pH* and therefore to an increase of $k_L a$. The bubble flow regime seems to be the regime with the lowest mass transfer: The specific interfacial area is comparatively low and the mass transfer within the liquid phase is dominated by diffusion. Due to the gas consumption the flow pattern at the reactor outlet was in all experiments bubble flow regime.

6.1.3 Influence of mean residence time

In the Taylor flow regime the slip is close to one, both phases pass the microchannel with the same velocity. Hence the mean residence time calculated from the volumetric flow rates can be used as real residence time. We investigated the influence of the residence time on mass transfer for $\varepsilon_L^* = 0.2$ and $\varepsilon_L^* = 0.4$. In both cases, Taylor flow is created at the reactor inlet. The results are depicted in Fig.6.3. The first remarkable result is the coincidence of both curves. For a given flow pattern in the investigated range, the $k_L a$ value depends on the residence time and not on the gas amount. No effect of the resulting slug length and the secondary flow pattern in the liquid phase was observed in the investigated range.
A comparison of the data obtained in this study with literature values is given in Fig.6.4. In the work of Yue et al. (2007) aqueous solution of sodiumhydroxide is used in a microreactor with a cross section of $1000\ \mu m \times 500\ \mu m$. To visualize all important parameters, the $k_L a$ value is plotted versus the superficial gas velocity and the volume transport ratio ε_L^*. Yue et al. (2007) demonstrated that both, increasing the su-

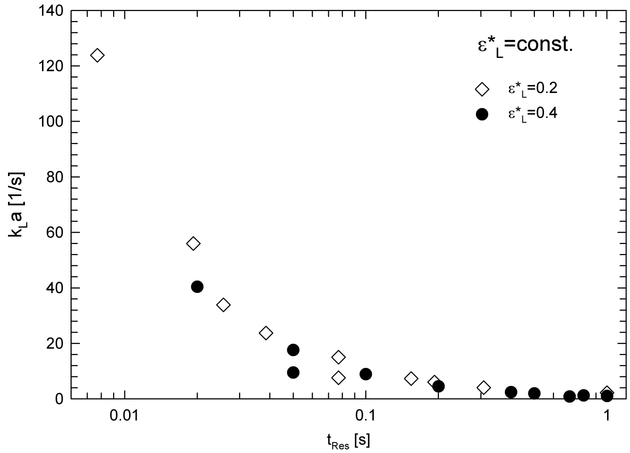

Figure 6.3: Measured $k_L a$ versus the mean residence time.

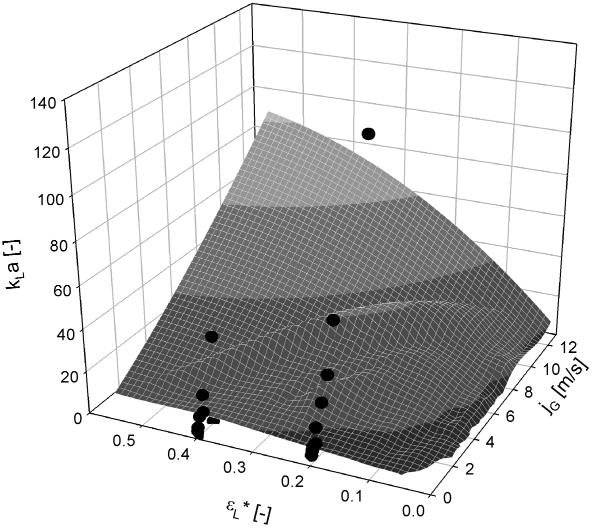

Figure 6.4: Comparison of literature values (mesh) and data of this study (dots). Experimental data were obtained for $\varepsilon_L^* = 0.4$ and $\varepsilon_L^* = 0.2$.

perficial gas velocity as well as the liquid volume transport fraction leads to an increase of the k_La-value. The influence of ε_L^* can be neglected for low gas velocities and is more pronounce at short residence times. At a given ε_L^*, the k_La-values of our experiments are approximately three times better than those of Yue et al. (2007). The reason for this mass transfer improvement is due the cross section: The cross section used in this work is 300 $\mu m \times$ 180 μm. Therefore the specific interfacial area is approximately three times larger compared to that in the work of Yue et al. (2007). In this range miniaturization leads to a mass transfer enhancement solely by the increase of specific interfacial area.

6.2 Extraction of vanillin for different flow pattern

In this section the extraction of vanillin dissolved in water with a suitable organic phase using microstructured devices made of PDMS is discussed. Two flow patterns, segmented and stratified flow, were compared. LIF- and μ-PIV measurements resulted in a laminar profile for stratified flow, whereas for segmented flow vortices in the slug end were detected. Additionally the influence of the channel width and therefore the surface-to-volume-ratio was investigated for the stratified flow regime.

6.2.1 Specific literature review

In recent years large efforts in realizing a "lab on a chip" were done. Fast mixing (Nguyen and Wu; 2005; Hardt et al.; 2005), chemical reactions (Losey et al.; 2001; Guenther, Khan, Thalmann, Trachsel and Jensen; 2004; de Mas et al.; 2003) and reactions including particle formation (Krishnadasan et al.; 2007; Khan et al.; 2004; Jeong et al.; 2005) were performed. To implement a complete process on the chip, phase separation of two immiscible liquids is one of the present challenges. We investigated a liquid extraction process in rectangular microchannels. This includes the creation of a stable interfacial area in the inlet zone, an extraction area and a phase separation zone. Since different flow patterns for liquid-liquid flow are known, we compared two of the most relevant ones, the segmented flow regime and the stratified flow regime. Kuban et al. (2003) investigated the formation of stratified flow in rectangular glass microchannels for different immiscible liquids experimentally and numerically. The channels had a height of 0.4 *mm* and a width of 2 *mm*. Due to the wetting properties the layer split was in the flat direction, providing a large interfacial area. For small velocities, segmented flow was observed, whereas a stable stratified flow occurred at higher velocities ($> 10\ mm/s$). Other important parameters are the surface tension and viscosity: moderate surface tension ($30\ldots50\ mN/m$) as well as low viscosity values ($< 1\ mPas$) of the organic phase (chloroform, hexane) gave only segmented flow with water. In a recent review paper, Shui et al. (2007) reported about segmented and stratified flow and their application. Due to ease of separation they performed the extraction only in stratified flow. For efficient separation, structured guidelines were reported. Nevertheless the advantages of segmented flow in reaction engineering due to narrow residence time distributions and large interfacial area are pointed out. In addition to the hydrodynamic studies reported above, extraction in micro channels was studied by various groups. Xiao et al. (2006) investigated the extraction of ephedrine from aqueous solution. The channel was made of PDMS/glass and had a cross section of $200\ \mu m \times 40\ \mu m$. The inlet was a conventional T-shaped design. The flow tended to form segmented flow with the aqueous phase as dispersed phase. Surface modification of the wall led to a stable stratified two-phase flow. A complete separation by a Y-shaped separator was not possible. Different solvents were tested. Each reactor was used one time; nothing is said about the swelling behavior. The group Kitamori (Tokeshi et al.; 2002, 2000; Tokeshi and Kitamori; 2005; Sato et al.; 2003a,b) investigated as one of the first extraction in microscale. The reactors were chemically etched and had ”guide structures” which enable an efficient separation. The flow pattern was limited to stratified flow. Due to the guidelines the interfacial area was reduced. In this study the large potential of continuous extraction in microscale had been demonstrated. In an industrial cooperation, Benz et al. (2001) used static mixers to perform liquid extraction of various compounds. The large interfacial area, originally designed for fast mixing, resulted in a very efficient extraction. Phase separation was reported to work well, but it is supposed that phase separation was done outside the device. Kashid et al. (2007) investigated extraction in segmented flow in circular capillaries. The microchannel consisted of a single capillary with an internal diameter of 0.5, 0.75 or 1 mm. The inlet as well as the outlet was made by a Y-shaped union. Separation was enabled by using different capillaries (PTFE and steel) to separate the phases by their surface properties. Kralj et al. (2005, 2007) performed the extraction of N,N-dimethylformamide (DMF) from an organic phase into water.

Phase separation was done by a porous fluoropolymer membrane. This device is very effective, but difficult to implement. Recently, Mary et al. (2008) reported about their online analysis of extraction in segmented flow: fluorescin and rhodamine respectively were dissolved in octan-1-ol and water to study both, purification and extraction of dispersed droplets. During droplet formation, fluorescent dye penetrated through the interfacial area at the junction. As soon as a steady moving droplet is created, fluorescent dye was transferred over the interfacial area and spread within the droplet by the streamlines. Concentration in the center of the vortex was low, because only diffusion mechanism transported material from streamline to streamline. Performing experiments in winding zigzag channels did not improve mass transfer. The velocity was in a range of $8.5 \pm 0.5\ mm/s$.

The overall volumetric mass transfer coefficient depends on the chemical system and on the reactor type. Whereas the mass transfer for an agitated vessel is very low ($k_L a \approx 0.1...20 \cdot 10^{-4}\ 1/s$), an enhancement of the mass transfer can be achieved by spray and packed columns ($k_L a \approx 1...10 \cdot 10^{-3}\ 1/s$). Further increase can be achieved by advanced reactor designs as the impinging stream ($k_L a \approx 1...300 \cdot 10^{-3}\ 1/s$). Due to the large interfacial area, microreactors provide high mass transfer values in the range of ($k_L a \approx 1\ 1/s$).

In this project, we focus on the comparison of two flow patterns. We chose the extraction of vanillin as an industrial relevant process (Patwardhan and Deshpande; 1979; Hocking; 1997) with an easily manageable analysis of both phases. The organic solvent was selected based on the distribution ratio and its compatibility to polydimethylsiloxane (PDMS). We compare stratified and segmented flow for different channel cross sections. The stable flow regime was created by the inlet design. By varying the volumetric flow rates, the influence of the residence time was characterized. To understand the differences in mass transfer between stratified and segmented flow, we made LIF- and μ-PIV measurements to characterize the flow. Finally we investigated the separation efficiency of both phases on the chip.

6.2.2 Extraction solvent

First a suitable organic phase, providing efficient extraction and being compatible to the PDMS-reactors, had to be found. An overview over literature data is given in table 6.1.

Table 6.1: Distribution ratios of vanillin for different solvents (Patwardhan and Deshpande; 1979).

Solvent	Hexane	Toluene	Benzene	Dichlorethane	Chloroform
D	0.2	4.1	6.3	20.2	26.5
Formula		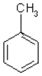		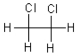	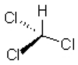

Although chloroform is the best suited extraction solvent, we choose toluene since the swelling behavior of chloroform in PDMS is unacceptable strong, see page 29. The equilibrium values for the extraction in toluene were verified in a batch experiment. For this purpose 50 *ml* toluene and 50 *ml* of water with a concentration of 1 g/l vanillin were put into a separating funnel. Intensive shaking for 10 minutes was performed. After phase separation due to gravity, both phases were analyzed concerning their vanillin content. An equilibrium value of $D = 4.14$ was found, in good agreement with the literature. After these preliminary experiments, we were interested in quantifying the effect of flow pattern on extraction efficiency.

6.2.3 Influence of flow pattern

Since segmented flow is one of the most promising flow patterns for good mass transfer (large interfacial area and secondary velocity profile in each segment) we designed a reactor to form droplets of constant size. Due to the equal volumetric flow rates, the ratio of the organic and aqueous segment is supposed to be equal. To compare the influence of the surface-to-volume ratio with the stratified flow, extraction was performed with different channel width. The height and the length of the channel was constant at $h = 140\ \mu m$ and $l = 44\ mm$. The residence time was varied by adjusting the volumetric flow rates. The flow pattern was adjusted by the geometry: For stratified flow a Y-junction was used as inlet and as outlet. Due to the rounded Y-junction design both phases did not change their flow direction at the merging and splitting point. An inlet as described in section 4.1 was used to generate segmented flow. Separation was done either by capillary forces as described in section 4.3.1 or by different wall properties (see section 4.3.2).

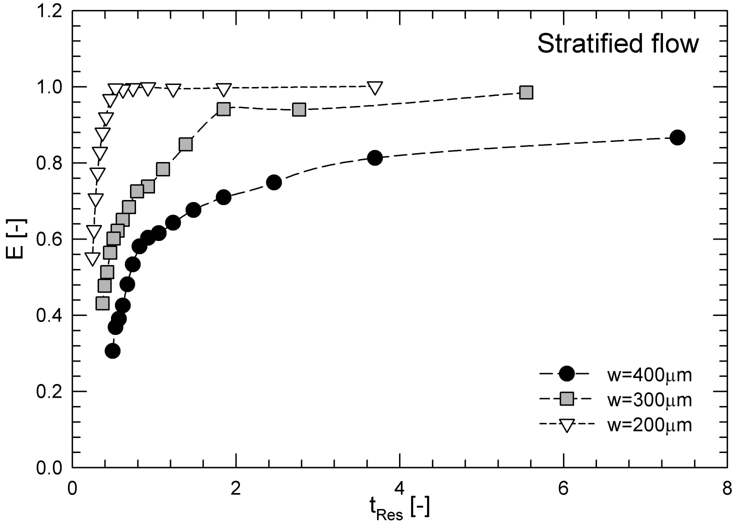

Figure 6.5: Extraction efficiency for stratified flow.

Stratified flow

The extraction efficiency for stratified flow is plotted in Fig.6.5. Phase equilibrium, which is equivalent to $E = 1$, was not achieved for the largest channel ($w = 400\ \mu m$) within the investigated residence time of below 8 s. Decreasing the channel width leads to an enhancement of the extraction efficiency: For a channel width of 200 μm equilibrium is achieved within 1 s, for the 300 μm channel within 4 s. The slope of the measured data for small residence times and before achieving the equilibrium is the steepest for $w = 200\ \mu m$ and decreases with the channel width. This means that for higher throughput values ($\dot{V}_{org} \approx 100 - 150\ \mu l/min$) small changes of the volumetric flow rate result in a significant change of the extraction efficiency.

The corresponding k_La-values are plotted in Fig.6.6. Decreasing the channel and therefore the diffusion paths results in a significant enhancement of the k_La-values. Since diffusion is the dominating mass transfer mechanism, a decrease of the lamellae width of factor 2 results in a decrease of the diffusion time of factor 4. Additionally, decreasing lamellae width results also in a increased surface-to-volume ratio. The occurrence

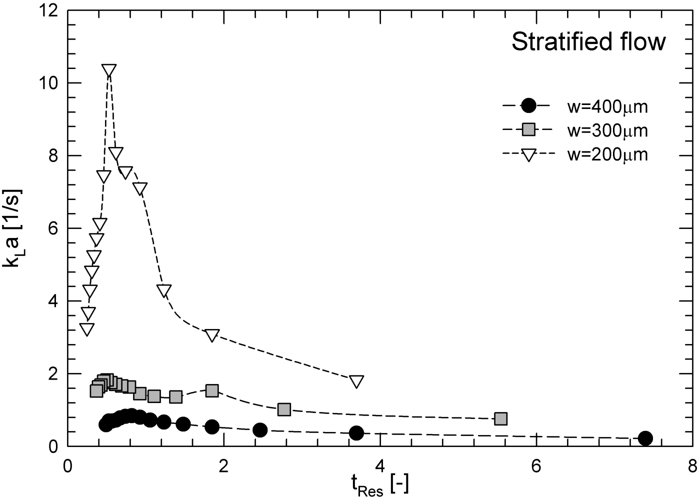

Figure 6.6: Mass transfer coefficient for stratified flow.

of a maximum in the k_La-value is due to equilibrium: as soon as $E = 1$ is achieved, longer residence times will not enhance mass transfer. Therefore the highest of the k_La-values needs to be considered. This can be used as design criteria, since longer residence times lead to a decrease of the throughput or, if the length of the microreactor is adapted, to a pressure drop increase.

Taylor flow

For segmented flow, which was investigated for a channel width of $w = 300\ \mu m$, extraction efficiency close to equilibrium is achieved within significant shorter residence times than in the corresponding stratified flow. The results for the efficency are depicted in Fig.6.7. Two different inlet designs leading to different sized slugs (see section 4.1). For high throughput values (volumetric flow rates $> 100\ \mu l/min$) the extraction efficiency for segmented flow is increased by a factor of 2 compared to stratified flow at the same channel width. Smaller slugs lead to larger efficiency values for given residence times. As for the extraction efficiency, the segmented flow in a 300 μm width channel shows increased

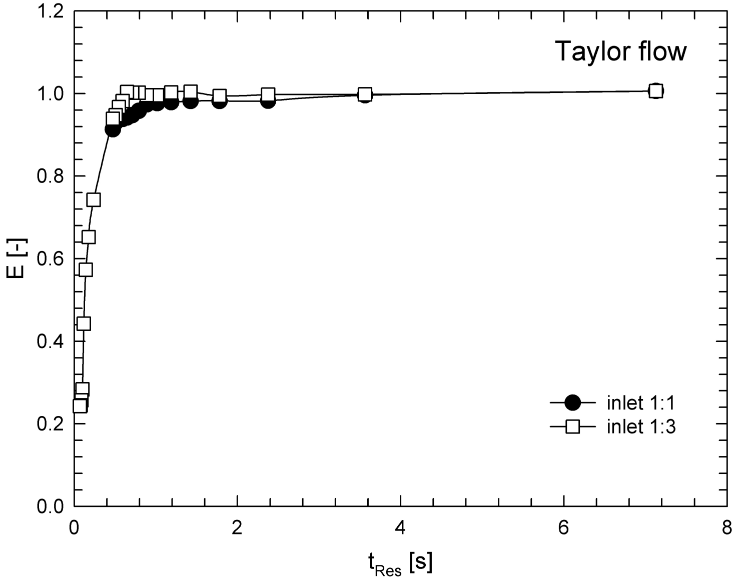

Figure 6.7: Extraction efficiency for segmented flow for a channel width of $w = 300\ \mu m$. Slug velocity varied between $u_S = 0.006...0.6\ m/s$.

mass transfer compared to the corresponding stratified flow, but the k_La-values for stratified flow in a very narrow channel (200 μm width) are slightly better, see Fig.6.8. All experiments in segmented flow were performed in a channel with a width of 300 μm and a height of 180 μm. The width of the aqueous inlet was equal to the width of the main channel (black dots) and one third of the main channel (white dots). For the investigated residence times ($t_{Res} = 0.5 \ldots 7\ s$), the efficiency was always very high. Even for the shortest residence time, an efficiency of 95% was observed. This is much better than the results for stratified flow. The k_La-values are in the range of 5 $1/s$, which is 2.5 times better than for the corresponding stratified flow channel. An increase of the efficiency, especially for low residence times, was observed using the small aqueous inlet. The mass transfer enhancement is based on two hydrodynamical effects: first, the droplet volume is smaller, therefore less material has to be brought to the interfacial area. Additional, the (specific) interfacial area itself is increased.

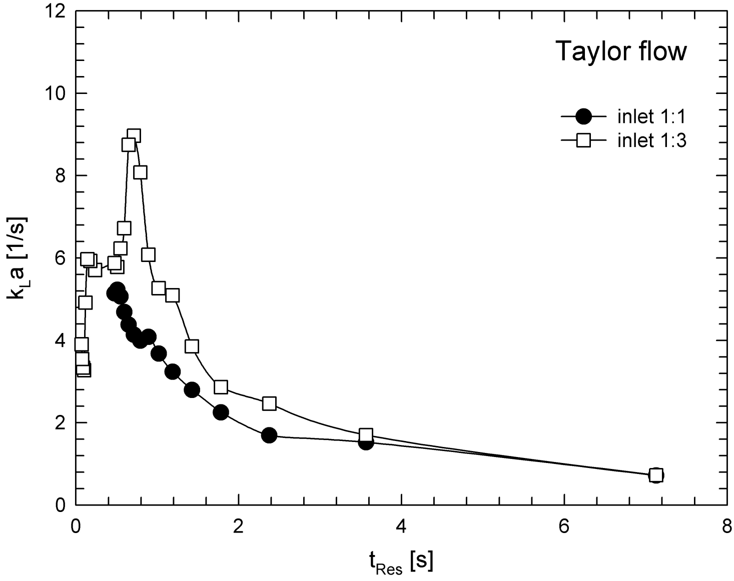

Figure 6.8: Mass transfer coefficient for segmented flow for a channel width of $w = 300\ \mu m$. Slug velocity varied between $u_S = 0.006...0.6\ m/s$.

Since the interfacial area is 1.8 times larger than in the stratified region, the k-value itself is higher for segmented flow. The surface to volume ratio varies for stratified flow from $10'000\ 1/m$ for a channel width of $200\ \mu m$ to $5'000\ 1/m$ for $w = 400\ \mu m$. Dividing the k_La value with the specific interfacial area characterizes the mass transfer. The values are in the range of $k_L = 2...4 \cdot 10^{-4}\ m/s$ for segmented flow and achieve a maximum of $10.8 \cdot 10^{-4}\ m/s$ for the stratified flow in the $200\ \mu m$ channel. Hence the layer thickness and the flow profile affect the mass transfer independent of the specific interfacial area.

Comparison of flow properties

To understand the results presented above, a hydrodynamic study was performed. Since Re is very small (1.2. . . 44.1) a laminar flow profile is expected. Therefore the radial mass transfer for stratified flow depends solely on diffusion. In Fig.6.9 (a) the LIF-pictures for stratified flow at

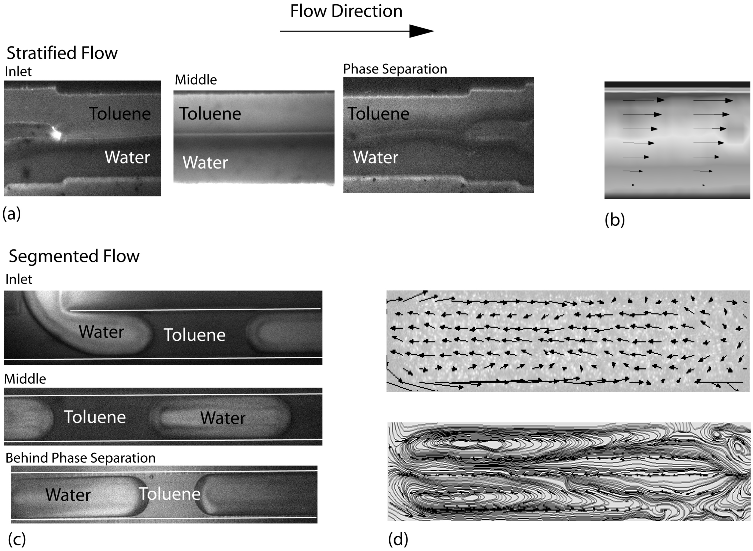
Flow Direction
Stratified Flow
Inlet
Toluene
Water
Middle
Toluene
Water
Phase Separation
Toluene
Water
(a)
(b)
Segmented Flow
Inlet
Water
Toluene
Middle
Toluene
Water
Behind Phase Separation
Water
Toluene
(c)
(d)

Figure 6.9: Comparison of the flow properties. All measurements were done for a channel width of $w = 300\ \mu m$. Volumetric flow rate for each liquid phase was in all cases 80 $\mu l/min$. (a) LIF-measurement for stratified flow. (b) Results for μ-PIV in the aqueous phase for stratified flow. (c) LIF-measurement for segmented flow at the reactor inlet, middle and behind the phase separation area. (d) Results for μ-PIV in the aqueous slug. Slug velocity was substracted to visualize the secondary flow pattern.

the inlet, middle and outlet of the channel are shown for stratified flow. The organic phase (toluene) was colored with rhodamine and reflects the light, whereas the water was not colored and is the black phase. Since the flow pattern was equal for all three investigated channel width and all investigated flow rates, we plot the results only for $w = 300\ \mu m$ and medium velocity. At the inlet, both phases were brought into contact and each phase covered 50% of the channel cross section. In the middle, the stratified flow is still existent and very stable. No interruptions can be seen at the interfacial area. The aqueous phase covers approximately 60% of the channel width, which can be explained by the higher viscosity (see table 3.2). The organic phase covers a smaller channel area and moves faster. This effect was observed for all investigated channel widths and velocities. At the outlet, which was designed like the in-

let, the phases were separated effectively. For small and medium flow rates the separation of both phases was perfect, although no guideline structures on the channel top were used. For high velocities some water swept into the organic outlet. The aqueous phase outlet was free of organic material. This easy way of phase separation worked very well. The μ -PIV results for stratified flow are shown exemplarily in Fig.6.9 (b). Vectors indicate the velocity profile, the background characterizes the velocity in flow direction. Note, that only the aqueous phase was analyzed. The laminar flow profile is well established.
LIF-measurements for segmented flow are presented in Fig.6.9 (c). The aqueous phase is colored with rhodamine. Due to the hydrophobic behavior of the PDMS toluene forms the continuous phase and covers the wall. The flow is very stable. The separator which was designed according to the experiences in gas-liquid flow removed approximately 85% of the organic phase. Some toluene stayed in the aqueous channel. To perform a perfect separation in liquid-liquid, some different designs, based on the wetting properties, should be developed. The secondary flow profiles obtained by μ-PIV are shown in Fig.6.9 (d). The slug velocity had been subtracted. The axisymmetric recirculation is clearly visible. Since the recirculation occurs only in the back half of the channel, shorter slugs will provide an enhanced mass transfer as described above.

6.2.4 High throughput extraction by bifurcation

Specific reactor design

For higher flow rates the residence time will be too short to achieve efficient mass transfer. To overcome this limitation, longer channels or an internal numbering up should be applied. Whereas the first solution is easy to implement, the pressure drop might get problematic, see section 5.1. Therefore we designed a microreactor with one wide main channel ($w = 1000\ \mu m$) which bifurcates into 8 microchannels ($w = 300\ \mu m$). A scheme of the device is given in Fig.6.10. Due to the low pressure drop over outlet 1 the separator did not work completely (see section 4.3). Formation of Taylor flow was instable at the inlet, in the most cases stratified flow was created. Stable two-phase flow was observed when locking inlet 2 and creating the two-phase flow outside the channel by a tee (Upchurch).

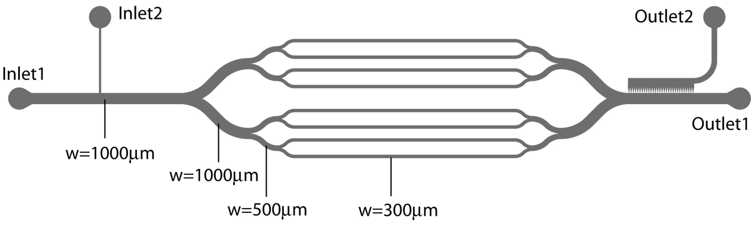

Figure 6.10: Microchannel for high flow rates.

Results

The different flow pattern had a significant impact on the extraction efficiency and the volumetric mass transfer. Both are plotted in Fig.6.11, whereas the extraction efficiency is marked with the black dots and the axis on the left side. The mass transfer coefficient is denoted by white symbols with the corresponding axis at the right side.
For stable Taylor flow by using the external tee, overall mass transfer coefficients of $k_La > 5\ 1/s$ were observed for volumetric flow rates between $\dot{V}_{aq} = \dot{V}_{org} = 900 - 2'200\ \mu l/min$. For lower flow rates equilibrium was achieved and the increased residence time had no effect on the mass transfer. The flow was stable for more than 3 hours. After this time the experiment had been canceled. Compared to the single channel device in section 6.2.3 the k_La-values are in the same range as those for the inlet ratio of 1:1. The droplets were generated at the external tee with a ratio of $d_{org} = d_{aq} = 509\ \mu m$. Since the aqueous droplets were not split at the bifurcation but were divided equal to the following channels, the droplets in the 300 μm section had a length in the range $2'000 - 2'500\ \mu m$. The interfacial area was therefore not as large as possible. An increase of the specific interfacial area can be achieved by droplet fission. Therefore the design of the bifurcation has to be changed to a T-like shape to allow droplet elongation (Link et al.; 2004; Teh et al.; 2008). As mentioned above, one major challenge for internal numbering up is the equal flow distribution and the stable two-phase flow. An example of unstable flow combined with imperfect flow distribution is given in Fig.6.11 with the diamond shaped dots: the multiphase flow using the second inlet was a stratified flow pattern. At the first bifurcation the flow was split in the same way as described in section 6.2.3 for stratified flow. Consequently, 4 of the 300 μm-channels were filled with aqueous phase, 4 with organic

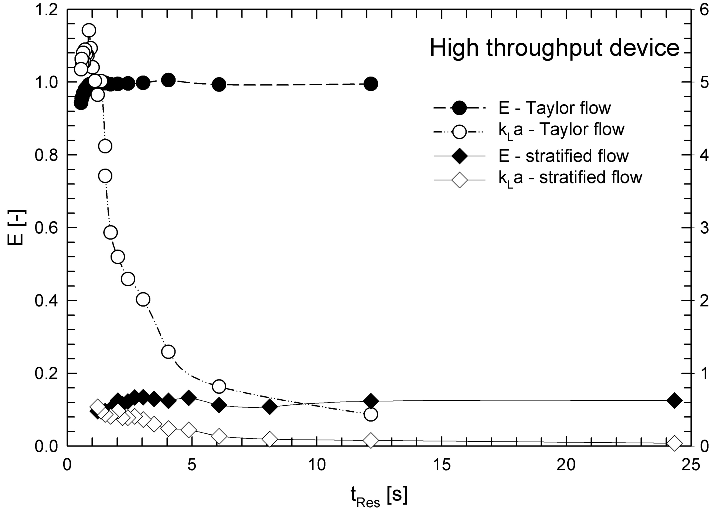

Figure 6.11: Extraction characteristics for high flow rates.

material. Mass transfer over the interfacial area occurred only at the first and the final 1000 μm channel. The contact time is much too short to achieve equilibrium by diffusive transport in these two sections. Therefore the extraction efficiency as well as the k_La-value are very poor.

6.2.5 Increased mass transfer by meandering channels

An increase of the mass transfer by enhancing the convective mass transfer within the slugs should be possible by meandering channels as described in chapter 4.2. Therefore we manufactured channels with the length of $l = 44$ mm, channel width of $w = 200$ μm and $w = 400$ μm and bend radii of $r = 1$ mm and $r = 2$ mm. To increase the number of bends at the given length, no straight section as it was done in chapter 4.2 was inserted between the bends.

Results

The results for the extraction performed with the four different channel designs are depicted in Fig.6.12 for the extraction efficiency and in

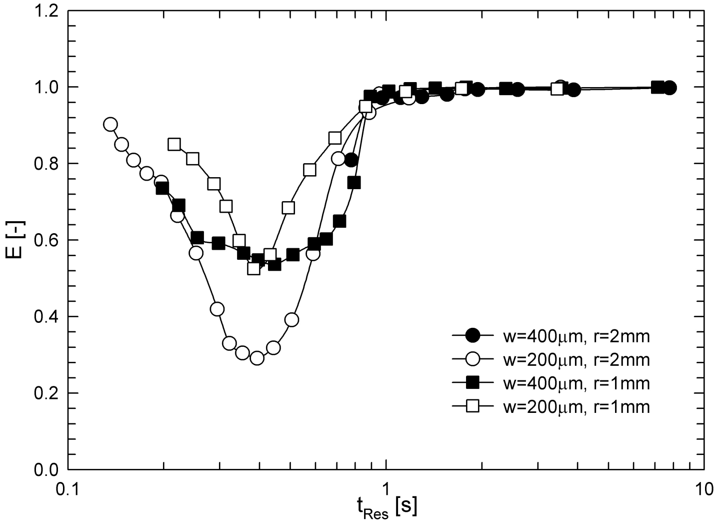

Figure 6.12: Extraction efficiency values for meandering channels versus the residence time. Minima mark the onset of efficient mass transfer by meandering microchannels.

Fig.6.13 for the k_La-value. The general tendency is for all investigated meandering designs similar: For high residence times ($t_{Res} > 1\ s$) and therefore at low volumetric flow rates equilibrium is achieved. In the range of $t_{Res} = 1\ s$ the efficiency decreases significantly. This corresponds to the observation done for straight channels, see section 6.2.3.

For residence times below 1 s and therefore high velocities, a remarkable difference compared to the experiments in the straight channel was observed: Decreasing residence time leads first to a decrease in extraction efficiency compared to the straight channel design. If the residence time decreases to values below 0.4 s, the efficiency and mass transfer coefficient will increase again to values close to equilibrium. This mimimal value in extraction efficiency is observed for velocities in the range of $u_S \approx 0.1\ m/s$. According to the velocity profiles in section 4.2.5 this velocity is the onset of a significant nonsymmetric secondary flow profile in the liquid slugs at the channel bend. This agrees within the experiments of Mary et al. (2008) where no influence of the zizag channel was

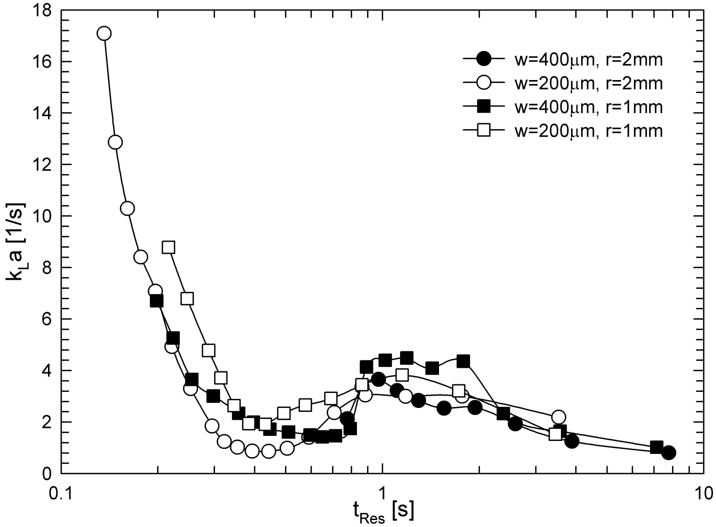

Figure 6.13: Volumetric overall mass transfer coefficient for meandering channels versus the residence time.

observed for velocity values of 8.5 mm/s.

The nonsymmetric profile itself is in this specific case not as important as the intensity and the rearrangement of the vortices, which enhance the convective mass transfer. The increased ”turbulence” leads to a faster renewing of the interfacial area. The intense mixing leads to a constant vanillin concentration in the bulk. Therefore the concentration close to the boundary layer is kept at a high level for the aqueous phase. The concentration difference at both boundary layers is therefore close to its maximum and the mass transfer coefficient is at a high level. The flow rates varied in these experiments between $\dot{V}_{org} = \dot{V}_{aq} = 25...900\ \mu l/min$ for the channels with $w = 400\ \mu m$ and for the channels with a width of 200 μm between $\dot{V}_{org} = \dot{V}_{aq} = 25...650\ \mu l/min$. At higher flow rates the reactor inlet failed.

6.3 Summary

The mass transfer over gas-liquid and liquid-liquid interfaces was investigated. As gas-liquid model process the absorption of CO_2 into an alkaline solution was chosen.
Since the gas phase consist of pure CO_2 and no transport step to the interfacial area is required, for the absorption of CO_2 into alkaline solution three mass transfer steps can be recognized:

1. Mass transfer of gaseous CO_2 over the interfacial area and dissolving in the liquid phase (CO_2^L).
2. Diffusive-based transport of dissolved CO_2^L across the liquid boundary layer.
3. Transport of carbonate ions into the liquid bulk.

As soon as CO_2^L is provided by physisorption, the chemisorption according to 6.1 and 6.2 takes place. Since the reaction equilibrium depends on the pH it is advantageous to avoid pH-differences in the bulk. This is realized by the short diffusion ways in microchannels as well as by the secondary flow pattern in the liquid slug, renewing the surface continuously. Investigations of different initial flow pattern and mean residence times gave the following results:

- The mass transfer is effected significantly by the flow pattern. Flow pattern with large specific interfacial area and enhanced convection in the bulk are advantageous.
- For a well defined flow pattern, the overall mass transfer coefficient depends mainly on the residence time.
- Even if no equilibrium-like conditions are achieved at the reactor outlet the mass transfer may increase with decreasing residence time. This depends mainly on the reaction system.
- No difference of the mass transfer coefficient were found for Taylor flow with two different liquid volume transport fraction.
- Decreasing channel size leads to increased mass transfer coefficients. Compared to literature values, our results indicate an improvement of the overall mass transfer coefficient by factor 3.

Since the flow was not very stable and the flow pattern itself changed due to gas consumption, an additional process to demonstrate the influence of the hydrodynamic properties was needed. The extraction of vanillin dissolved in water into toluene was selected to analyze the liquid-liquid mass transfer.

An overview over the results of extraction of vanillin is given in table 6.2. The maximum k_La value is divided by the approximated specific interfacial area (taken from the experiments) to obtain the maximum k_L value which gives more information on the mass transfer itself. The corresponding volumetric flow rate and the residence time is given as well. The table indicates that the best overall mass transfer is observed for stratified flow in a microchannel with $w = 200\ \mu m$. It should be noted, that the volumetric flow rate is very small. Increasing the interfacial area is an efficient tool to increase mass transfer. The use of meandering channels provides high mass transfer coefficients at high flow rates and short residence times. In addition to the results obtained by the absorption of CO_2 in alkaline solution, the following more specified results can be drawn from the extraction of vanillin:

Table 6.2: Maximum mass transfer coefficients for all reactor designs in the investigated range.

Flow	a $[1/m]$	k_La_{max} $[1/s]$	$k_{L_{max}}$ $[10^{-4} m/s]$	$\dot{V}$ $[\mu l/min]$	t_{Res} $[s]$
stratified, $w = 200\ \mu m$	10’000	10.8	10.8	70	0.52
stratified, $w = 300\ \mu m$	6’667	1.9	2.85	110	0.50
stratified, $w = 400\ \mu m$	5’000	1.1	2.20	90	0.82
segmented, inlet 1:1	20’000	5.3	2.65	140	0.51
segmented, inlet 1:3	24’444	8.9	3.67	100	0.71
segmented, bifurcating	18’778	5.8	3.09	1400	0.87
meandering $w = 200\ \mu m$	26’060	17.1	6.56	650	0.13
meandering $w = 400\ \mu m$	16’060	6.7	4.17	900	0.20

- For low flow ratios and therefore small channel width the stratified flow regime provides acceptable overall volumetric mass transfer coefficients with facile phase separation on the chip.
- In Taylor flow, small droplets are advantageous for an intensified mass transfer. This enhancement is caused by the enhanced recir-

culation motion in smaller droplets. Additional, the surface will be faster renewed for short droplets.

- Internal numbering up by bifurcating channels is possible to enhance the flow rates.
- For wide channels as well as for bifurcating channels a change in flow pattern (from stable Taylor flow to stratified flow) decreases the mass transfer coefficient drastically.
- At high velocities ($u_S > 0.3\ m/s$) meandering channels provide an enhanced mass transfer due to permanent rearrangement of the secondary flow pattern. The vanillin concentration in the bulk can therefore be considered as constant, providing maximum concentration gradient at the interfacial area.

Chapter 7

Summary and Conclusions

In this thesis we examined two-phase flow in microchannels. The influence of channel design and fluid properties on mixing and mass transfer was investigated. For the experimental analysis microstructure devices of PDMS/glass or Si/glass with a rectangular cross section were built. Focusing on Taylor flow, optical characterization methods, especially LIF and μ-PIV, were applied to investigate the flow characteristics and mixing within the liquid phase on the chip. The measured pressure drop values were compared to literature models with the results showing a good match between theory and experiment. The secondary recirculating velocity profile was determined experimentally. To expand the investigated velocity range numerical investigations were performed. For the absorption and extraction experiments the products were analyzed offline. In the following paragraphs we summarize the main findings.
Based on a wide knowledge on Taylor flow this thesis provides some important additional details for a ”tailored Taylor flow” such as the investigations to the bubble and slug lengths and the interplay between velocity rates, design and flow pattern. Investigations done on the bubble breakup, mixing in meandering channels, flow properties at high pressure and the interaction between flow properties and mass transfer in microchannels yield in new results and open new process windows.

Influence of the channel design

The geometry of the gas inlet has a major impact on the resulting unit cell length and thus on important parameters, such as the pressure drop, the specific interfacial area and the slug length. If the Laplace pressure, which is influenced by geometrical aspects of the bubble with surface tension forces, exceeds a certain value, the disperse phase breaks up. Hence a decrease of the unit cell length can be obtained by decreasing the width of the gas inlet as well as by injecting the disperse phase in the main flow direction.

The recirculating axisymmetric secondary flow pattern within the liquid slugs provides fast and efficient mixing. Meandering channels are suitable to enhance mixing between both recirculation areas. Mixing length could be decreased by geometrical adaptions down to 12% compared to the straight reactor design. For a given channel width, a smaller bend radius provides a more effective mass transfer over the channel center line. This effect is less pronounced for diminishing inertia, as it is the case for small velocity values and significantly smaller channel diameters. An interruption of the symmetrical recirculation profile which is characteristic for Taylor flow was observed. An increase of the inertia forces led to a more pronounced asymmetrical velocity profile. The inner vortex moves to the back of the slug and crosses the channel center line, while the outer vortex is splitted into two smaller vortices. Pressure drop measurements indicate a reduction of the pressure drop per mixing length by 70%.

Due to the dominating influence of surface forces in microchannels, the influence of the channel wall on flow properties enables efficient phase separation on the chip. For small dimensions ($d_h < 400\ \mu m$) separation based on capillary forces is a simple and efficient tool. Although different materials are involved, separation based on wetting properties may be preferred in case of larger dimensions and / or high velocities.

Influence of the fluid properties

Hydrodynamic properties are affected mainly by the fluid properties. Since fluid properties, such as liquid viscosity or gas density, are not always a matter of choice, the influence of these properties on Taylor flow was investigated.

The liquid slug length increases with increasing viscosity. This effect is more pronounced for higher liquid velocities at a constant gas velocity. The slug length varies between $L_S \approx d_h$ for low viscosity values and slow velocity to $L_S \approx 4d_h$ for high viscosity values and fast velocity. The liquid holdup varies significantly over the channel length due to the pressure drop. A long channel is required for slow chemical reactions which require long residence times and for neglecting the effects of manifolds. A tradeoff between pressure drop and reactor length is mandatory.

Increasing the gas density results in slight changes of the Taylor flow characteristics. If the pressure increases at constant velocities, the pressure drop of the two-phase flow will decrease: The gas bubble length increases, the liquid slug length decreases at increasing pressure. The ratio of the gas bubble length to the liquid slug length increases at higher pressure values. The total liquid holdup decreases slightly for high pressure values, whereas the amount of liquid in the film increases with increasing pressure. The decrease of holdup corresponds with an increase of the intrinsic velocity.

Interfacial mass transfer

The main advantage of enhanced interfacial mass transfer in microchannels is the specific interfacial area. Furthermore the secondary recirculating flow pattern in Taylor flow provides efficient renewal of the interfacial area. For small throughput values ($\dot{V} \approx 100 \mu l/min$) stratified flow with small channel dimensions provides efficient mass transfer combined with a smooth phase separation on the chip. For higher flow rates Taylor flow is the more advantageous regime. High throughput values are feasible using bifurcating channels and meandering channels at high velocity rates. A combination of both may provide a powerful device for effective extraction in the range of up to $\dot{V} \approx 10\ ml/min$.

Chapter 8

Outlook

This section outlines subsequent research topics to provide more detailed understanding for optimized application of multiphase microfluidic processes.

8.1 Hydrodynamic properties of Taylor flow

Whereas the hydrodynamic properties for multiphase flow in microchannels are well described for moderate conditions with the focus on Taylor flow, the effect of extreme conditions, such as high viscosity ($\eta > 0.1$ *Pas* at ambient temperature), non-Newtonian fluids or the change between sub- to supercritical conditions, remains unexplored. Such investigations should rather focus on the field of fundamental understanding and the definition of an acceptable range of fluctuations than on a detailed analysis for a specific case.

Besides the well understood formation of Taylor flow in rectangular microchannels with the generated bubble and slug lengths, the characteristics of the liquid film, which covers the channel wall, are still almost unexplored. Except first attempts in characterizing the film thickness by Confocal Laser Scanning Microscopy (LSM) (Fries et al.; 2007) and first simulation of the flow profile in the corners (Sousa et al.; 2007), nothing has been reported in literature concerning the film stability, shape and velocity. This is mainly due to limits of the experimental methods: Optical characterization of flowing material close to the wall with typical dimensions of a few micrometer is challenging. The μ-PIV technique applied in this work would fail since the size of the particles is in the range of the film thickness. Reducing the particle size may lead to sticking problems between the particles and the wall as well as between the particles. Using suitable materials can avoid this problem. Nevertheless,

illumination of the flow is not straight forward. Volume illumination of the complete channel reduces the signal significantly, whereas a "point-by-point" illumination, like in the case of confocal LSM, suffers from the temporal resolution.
Nano-PIV using evanescent-wave illumination might be a suitable measurement technique to investigate the non-steady flow in the liquid film. Li, Sadr and Yoda (2006) demonstrated the use of this technique for a plane Couette flow and obtained data in a distance of 80 *nm* from the wall. Another possibility to characterize the film is high-speed LSM with up to 2000 $frames/s$ as reported by Kinoshita et al. (2007).
Although both measurement techniques are very complex, the results might provide detailed answers to the open questions concerning the liquid film: What is the residence time in the liquid film? Is there a significant mass transfer of liquid material from the slug to the film and vice versa? How is the axial dispersion influenced by the wall roughness, by the fluid properties and by the velocity? In which range is the contact time between the gas bubble and the liquid material at the film? If the reaction takes place in the liquid/continuous phase (e.g. by use of a homogenous catalyst), these questions will mainly concern the residence time distribution. As soon as the channel wall is catalytically active, the mass transfer of liquid and gaseous material within the film and therefore the hydrodynamic properties of the film become a crucial issue in terms of process intensification.
The focus of further investigations has to switch from a phenomenological point of view based on a specific case to a fundamental understanding, including theoretical foundations for precise modeling. Numerical solutions as they were presented for the liquid film by Bretherton (1961); Wong et al. (1995) need to be extended to describe the two-phase flow.

8.2 Hydrodynamic properties for packed bed

Multiphase reactions demanding a solid catalyst are often performed using packed bed. Packing properties and the influence on hydrodynamic properties are well understood for large scale columns. Applications of packed bed in microreactors were already reported (Losey et al.; 2001; Trachsel; 2008; Tadepalli et al.; 2007). Investigation on multiphase flow in a micro packed bed would provide effective tools for process optimization and intensification. Differences to packed bed at the macro scale are expected due to the increased void fraction and the different inlet section.

If a stable and well defined Taylor flow enters a packed bed, characteristic parameters, such as the interfacial area, the secondary flow pattern or the limited axial dispersion will change completely. Hence investigating an empty microchannel provides only limited information on the flow properties in the packed bed.

For liquid rich ”pulses” (corresponding to the liquid slugs in Taylor flow) the residence time in the packed bed, the amount of dynamic and static holdup and the occurrence of micro-vortices as well as dead volumes in the empty space between the particles should be explored. These aspects are also important for the gas rich ”pulses” (corresponding to the gas bubbles in an empty channel): the wetting degree at the particles, the static liquid holdup as a function of the gas flushing time and the residence time are important aspects. Finally the interplay between the three phases is essential: the advantage of shortened diffusive paths in the packed bed has to be enhanced by an optimized gas-liquid frequency, resulting in an effective wetting degree at the catalyst surface, appropriate residence time distribution, reduced static liquid holdup and optimized selectivity.

These matters should be investigated experimentally and numerically. For an experimental approach online measurements might be performed by LIF/LSM with transparent particles or by XTM.

8.3 Multistage extraction

Considering the extraction in the microscale, two problems have to be solved in the future: an effective 100% continuous separation of the phases on the chip and the performance of multistage countercurrent continuous extraction should be realized.

A first concept of such an extraction process is given in Fig. 8.1. The maximum number of stages is N. It is important, that at each stage $n = 1 \ldots N$ the pressure at the inlet and at the outlet has to be equal for both phases. Otherwise no defined flow pattern can be formed and both phases will leave the reactor at the outlet, which provides the lower pressure drop. The realization of such a concept is not trivial. Either additional pumps have to be used to increase the pressure for the organic phase from stage to stage or the the pressure of each stage needs to be raised using back pressure regulators.

At least the organic outlet at stage 1 and the aqueous outlet at stage N have to be free from other material. To guarantee such a perfect

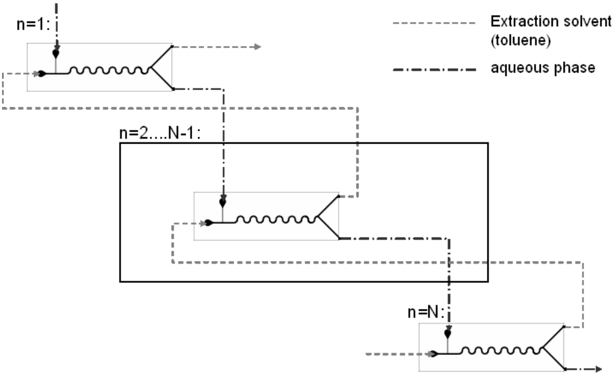

Figure 8.1: Concept of a multistage extraction in microscale.

separation, the outlet has to be designed either by using different wall properties (using different materials or wall coating) or by creating a stratified flow with the subsequent simple separation by a Y-junction. A combination of both principles might provide best separation. Therefore, first a stratified flow with a Y-junction outlet has to be created. In a second step the organic outlet will be separated by a Y-junction with different capillaries at the outlet, removing traces of aqueous material. Such a design would be suitable for a wide range of flow rates and different volumetric flow ratios of both phases.

Bibliography

Akbar, M. K. and Ghiaasiaan, S. M. (2006). Simulation of Taylor flow in capillaries based on the volume-of-fluid technique, *Ind. Eng. Chem. Res.* **45**(15): 5396–5403.

Al-Rawashdeh, M., Hessel, V., Löb, P., Mevissen, K. and Schönfeld, F. (2008). Pseude 3-d simulation of a falling film microreactor based on realistic channel and film profiles, *Chemical Engineering Science* **in press**.

Benz, K., Jaeckel, K. P., Regenauer, K. J., Schiewe, J., Drese, K., Ehrfeld, W., Hessel, V. and Loewe, H. (2001). Utilization of micromixers for extraction processes, *Chemical Engineering & Technology* **24**(1): 11–17.

Bercic, G. and Pintar, A. (1997). The role of gas bubbles and liquid slug lengths on mass transport in the Taylor flow through capillaries, *Chemical Engineering Science Gas-Liquid-Solid Reactor Engineering* **52**(21-22): 3709–3719.

Brandner, J. J., Bohn, L., Henning, T., Schygulla, U. and Schubert, K. (2007). Microstructure heat exchanger applications in laboratory and industry, *Heat Transfer Engineering* **28**(8): 761 – 771.

Bretherton, F. (1961). The motion of long bubbles in tubes, *Journal of Fluid Mechanics* **10**(2): 166–188.

Chisholm, D. (1967). A theoretical basis for the lockhart-martinelli correlation for two-phase flow, *International Journal of Heat and Mass Transfer* **10**(12): 1767–1778.

Claudel, S., Nikitine, C., Boyer, C. and Font, P. (2005). Gas-liquid mass transfer in a microstructured falling film reactor, *AIChE Spring National Metting, Conference Proceedings* .

Coleman, J. W. and Garimella, S. (1999). Characterization of two-phase flow patterns in small diameter round and rectangular tubes, *International Journal of Heat and Mass Transfer* **42**(15): 2869–2881.

Danckwerts, P. V. (1952). The definition and measurement of some characteristics of mixtures, *Appl. Sci. Research, Section A* **3**: 279–296.

Danckwerts, P. V. and Sharma, M. M. (1966). Absorption of carbon dioxide into solutions of alkalis and amines (with some notes on hydrogen sulphide and carbonyl sulphide), *Transactions of the Institution of Chemical Engineers and the Chemical Engineer* **44**(8): CE244–280.

de Mas, N., Günther, A., Schmidt, M. A. and Jensen, K. (2003). Microfabricated multiphase reactors for the selective direct fluorination of aromatics, *Ind. Eng. Chem. Res.* **42**(4): 698–710.

Ehrfeld, W., Golbig, K., Hessel, V., Löwe, H. and Richter, T. (1999). Characterization of mixing in micromixers by a test reaction: Single mixing units and mixer arrays, *Ind. Eng. Chem. Res.* **38**(3): 1075–1082.

Ehrfeld, W., Hessel, V. and Loewe, H. (2000). Microreactors.

Fairbrother, F. and Stubbs, A. E. (1935). Studies in electro-endosmosis part VI the "bubble-tube" method of measurement, *J Chem Soc* **1**: 527–529.

Fleischer, C., Becker, S. and Eigenberger, G. (1996). Detailed modeling of the chemisorption of CO_2 into NaOH in a bubble column, *Chemical Engineering Science* **51**(10): 1715–1724.

Friedel, L. (1978). Druckabfall bei der Stömung von Gas/Dampf-Flüssigkeits-Gemischen in Rohren, *Chemie Ingenieur Technik* **50**(3): 167–180.

Fries, D. M., Trachsel, F. and Rudolf von Rohr, P. (2007). Optical characterization of phase distribution in gas-liquid Taylor flow in rectangular microfluidic channels, *International Conference on Multiphase Flow* **ICMF07**: 479.

Fries, D. M., Waelchli, S. and Rudolf von Rohr, P. (2008). Gas-liquid two-phase flow in meandering microchannels, *Chemical Engineering Journal* **135**(Supplement 1): S37–S45.

Fujisawa, N., Nakamura, Y., Matsuura, F. and Sato, Y. (2006). Pressure field evaluation in microchannel junction flows through μPIV measurement, *Microfluidics and Nanofluidics* **2**(5): 447–453.

Garstecki, P., Fuerstman, M. J., Stone, H. A. and Whitesides, G. M. (2006). Formation of droplets and bubbles in a microfluidic T-junction-scaling and mechanism of break-up, *Lab Chip* **6**(3): 437–446.

Guenther, A., Jensen, K. F., Jhunjhunwala, M. and Schmidt, M. A. (2004). Fluid separation, *Patent Application Publication* p. US 2007/0144967 A1.

Guenther, A., Khan, S. A., Thalmann, M., Trachsel, F. and Jensen, K. F. (2004). Transport and reaction in microscale segmented gas-liquid flow, *Lab Chip* **4**(4): 278–286.

Gunther, A., Thalmann, M., Jhunjhunwala, M., Schmidt, M. A. and Jensen, K. F. (2005). Micromixing of miscible liquids in segmented gas-liquid flow, *Langmuir* **21**(4): 1547–1555.

Guo, J. and Al-Dahhan, M. (2004). Liquid holdup and pressure drop in the gas-liquid cocurrent downflow packed-bed reactor under elevated pressures, *Chemical Engineering Science ISCRE18* **59**(22-23): 5387–5393.

Hao, P. F., Yao, Z. H., He, F. and Zhu, K. Q. (2006). Experimental investigation of water flow in smooth and rough silicon microchannels, *J. Micromech. Microeng.* **16**(7): 1397–1402.

Hao, P.-F., Zhang, X.-W., Yao, Z.-H. and He, F. (2007). Transitional and turbulent flow in a circular microtube, *Experimental Thermal and Fluid Science* **32**(2): 423–431.

Hardt, S., Drese, K. S., Hessel, V. and Schönfeld, F. (2005). Passive micromixers for applications in the microreactor and microTAS fields, *Microfluid Nanofluid* **1**(2): 108–118.

Haverkamp, V., Ehrfeld, W., Gebauer, K., Hessel, V., Löwe, H., Richter, T. and Wille, C. (1999). The potential of micromixers for contacting of disperse liquid phases, *Fresenius J Anal Chem* **364**(7): 617–624.

Haverkamp, V., Hessel, V., Löwe, H., Menges, G., Warnier, M. J. F., Rebrov, E. V., de Croon, M. H. J. M., Schouten, J. C. and Liauw,

M. A. (2006). Hydrodynamics and mixer-induced bubble formation in micro bubble columns with single and multiple-channels, *Microfluid Nanofluid* **29**(9): 1015–1026.

Heiszwolf, J. J., Kreutzer, M. T., van den Eijnden, M. G., Kapteijn, F. and Moulijn, J. A. (2001). Gas-liquid mass transfer of aqueous Taylor flow in monoliths, *Catalysis Today* **69**(1-4): 51–55.

Hessel, V., Angeli, P., Gavriilidis, A. and Loewe, H. (2005). Gas-liquid and gas-liquid-solid microstructured reactors: Contacting principles and applications, *Ind. Eng. Chem. Res.* **44**(25): 9750–9769.

Hessel, V., Hardt, S., Loewe, H. and Schönfeld, F. (2003). Laminar mixing in different interdigital micromixers: I.experimental characterization, *AIChE Journal* **49**(3): 566–576.

Hocking, M. B. (1997). Vanillin: Synthetic flavoring from spent sulfite liquor, *Journal of Chemical Education* **74**(9): 1055–1059.

Irandoust, S. and Andersson, B. (1989). Liquid film in Taylor flow through a capillary, *Ind. Eng. Chem. Res.* **28**(11): 1684–1688.

Jähnisch, K., Baerns, M., Hessel, V., Ehrfeld, W., Haverkamp, V., Löwe, H., Wille, C. and Guber, A. (2000). Direct fluorination of toluene using elemental fluorine in gas/liquid microreactors, *Journal of Fluorine Chemistry* **105**(1): 117–128.

Jensen, K. F. (1999). Microchemical systems: Status, challenges, and opportunities, *AIChE Journal* **45**(10): 2051–2054.

Jensen, K. F. (2001). Microreaction engineering - is small better?, *Chemical Engineering Science* **56**(2): 293–303.

Jeong, W. J., Kim, J. Y., Choo, J., Lee, E. K., Han, C. S., Beebe, D. J., Seong, G. H. and Lee, S. H. (2005). Continuous fabrication of biocatalyst immobilized microparticles using photopolymerization and immiscible liquids in microfluidic systems, *Langmuir* **21**(9): 3738–3741.

Kao, J. T. F. and Kobayashi, R. (1967). Viscosity of helium and nitrogen and their mixtures at low temperatures and elevated pressures, *The Journal of Chemical Physics* **47**(8): 2836–2849.

Kashid, M. N., Gerlach, I., Goetz, S., Franzke, J., Acker, J. F., Platte, F., Agar, D. W. and Turek, S. (2005). Internal circulation within the liquid slugs of a liquid-liquid slug-flow capillary microreactor, *Ind. Eng. Chem. Res.* **44**(14): 5003–5010.

Kashid, M. N., Harshe, Y. M. and Agar, D. W. (2007). Liquid-liquid slug flow in a capillary: An alternative to suspended drop or film contactors, *Ind. Eng. Chem. Res.* **46**(25): 8420–8430.

Khan, S. A., Gunther, A., Schmidt, M. A. and Jensen, K. F. (2004). Microfluidic synthesis of colloidal silica, *Langmuir* **20**(20): 8604–8611.

King, C., Walsh, E. and Grimes, R. (2007). PIV measurements of flow within plugs in a microchannel, *Microfluidics and Nanofluidics* **3**(4): 463–472.

Kinoshita, H., Kaneda, S., Fujii, T. and Oshima, M. (2007). Three-dimensional measurement and visualization of internal flow of a moving droplet using confocal micro-PIV, *Lab Chip* **7**(3): 338–346.

Kockmann, N. (2006). *Micro Process Engineering - Fundamentals, Devices, Fabrication and Applications*, Wiley-VCH Verlag GmbH & Co. KGaA, Weinheim.

Kralj, J. G., Sahoo, H. R. and Jensen, K. F. (2007). Integrated continuous microfluidic liquid-liquid extraction, *Lab on a Chip* **7**(2): 256–263.

Kralj, J. G., Schmidt, M. A. and Jensen, K. F. (2005). Surfactant-enhanced liquid-liquid extraction in microfluidic channels with inline electric-field enhanced coalescence, *Lab on a Chip* **5**(5): 531–535.

Kreutzer, M. T., Guenther, A., Brian, K. H. Y. and Jensen, K. F. (2006). On-chip dispersion measurement in segmented flow through microchannels, *AIChE annular metting* **San Francisco**.

Kreutzer, M. T., Kapteijn, F., Moulijn, J. A. and Heiszwolf, J. J. (2005). Multiphase monolith reactors: Chemical reaction engineering of segmented flow in microchannels, *Chemical Engineering Science* **60**(22): 5895–5916.

Kreutzer, M. T., Kapteijn, F., Moulijn, J. A., Kleijn, C. R. and Heiszwolf, J. J. (2005). Inertial and interfacial effects on pressure drop of Taylor flow in capillaries, *AIChE Journal* **51**(9): 2428–2440.

Kreutzer, M. T., Wei, W., Kapteijn, F., Moulijn, J. A. and Heiszwolf, J. J. (2003). Pressure drop of taylor flow in capillaries: Impact of slug length, *First International Conference on Microchannels and Minichannels* pp. 519–526.

Kreysa, G. and DECHEMA (1995). *Microsystem technology for chemical and biological microreactors: papers of the Workshop on Microsystem Technology, Mainz, 20-21 February, 1995.*

Krishnadasan, S., Brown, R. J. C., deMello, A. J. and deMello, J. C. (2007). Intelligent routes to the controlled synthesis of nanoparticles, *Lab Chip* **7**(11): 1434–1441.

Kuban, P., Berg, J. and Dasgupta, P. K. (2003). Vertically stratified flows in microchannels. computational simulations and applications to solvent extraction and ion exchange, *Analytical Chemistry* **75**(14): 3549–3556.

Kumar, V., Vashisth, S., Hoarau, Y. and Nigam, K. D. P. (2007). Slug flow in curved microreactors: Hydrodynamic study, *Chemical Engineering Science* **62**(24): 7494–7504.

Laborie, S., Cabassud, C., Durand-Bourlier, L. and Laine, J. M. (1999). Characterisation of gas-liquid two-phase flow inside capillaries, *Chemical Engineering Science* **54**(23): 5723–5735.

Lee, J. H. and Lee, Y. S. (2001). Pressure drop correlations for two-phase flow within horizontal rectangular channels with small heights, *International Journal of Multiphase Flow* **27**(5): 783–796.

Lee, J. N., Park, C. and Whitesides, G. M. (2003). Solvent compatibility of poly(dimethylsiloxane)-based microfluidic devices, *Anal. Chem.* **75**(23): 6544–6554.

Lerou, J. J. and Ng, K. M. (1996). Chemical reaction engineering: A multiscale approach to a multiobjective task, *Chemical Engineering Science* **51**(10): 1595–1614.

Li, G., Tao, W., Li, Z. and Yu, B. (2006). Direct numerical simulation of rarefied turbulent microchannel flow, *Microfluidics and Nanofluidics* **2**(2): 106–116.

Li, H. F., Sadr, R. and Yoda, M. (2006). Multilayer nano-particle image velocimetry, *Experiments in Fluids* **41**(2): 185–194.

Link, D. R., Anna, S. L., Weitz, D. A. and Stone, H. A. (2004). Geometrically mediated breakup of drops in microfluidic devices, *Physical Review Letters* **92**(5): 054503.

Liu, H., Vandu, C. O. and Krishna, R. (2005). Hydrodynamics of Taylor flow in vertical capillaries: Flow regimes, bubble rise velocity, liquid slug length, and pressure drop, *Ind. Eng. Chem. Res.* **44**(14): 4884–4897.

Lockhart, R. W. and Martinelli, R. C. (1949). Proposed correlation of data for isothermal two-phase, two-component flow in pipes, *Chemical Engineering Progress* **45**(1): 39–48.

Losey, M. W., Schmidt, M. A. and Jensen, K. F. (2001). Microfabricated multiphase packed-bed reactors: Characterization of mass transfer and reactions, *Ind. Eng. Chem. Res.* **40**(12): 2555–2562.

Marchessault, R. N. and Mason, S. G. (1960). Flow of entrapped bubbles through a capillary, *Ind. Eng. Chem.* **52**(1): 79–84.

Mary, P., Studer, V. and Tabeling, P. (2008). Microfluidic droplet-based liquid-liquid extraction, *Analytical Chemistry* **80**(8): 2680–2687.

Matsuyama, K., Tanthapanichakoon, W., Aoki, N. and Mae, K. (2007). Operation of microfluidic liquid slug formation and slug design for kinetics measurement, *Chemical Engineering Science* **62**(18-20): 5133–5136.

McDonald, J. C., Duffy, D. C., Anderson, J. R., Chiu, D. T., Wu, H., Schueller, O. J. A. and Whitesides, G. M. (2000). Fabrication of microfluidic systems in poly(dimethylsiloxane), *Electrophoresis* **21**(1): 27–40.

Meinhart, C. D., Wereley, S. T. and Santiago, J. G. (1999). PIV measurements of a microchannel flow, *Experiments in Fluids* **27**(3): 414–419.

Merkel, T. C., Bondar, V. I., Nagai, K., Freeman, B. D. and Pinnau, I. (2000). Gas sorption, diffusion, and permeation in poly(dimethylsiloxane), *Journal of Polymer Science* **38**: 415–434.

Mishima, K. and Hibiki, T. (1996). Some characteristics of air-water two-phase flow in small diameter vertical tubes, *Int. J. Multiphase Flow* **22**(4): 703–712.

Natrajan, V. and Christensen, K. (2007). Microscopic particle image velocimetry measurements of transition to turbulence in microscale capillaries, *Experiments in Fluids* **43**(1): 1–16.

Nguyen, N.-T. and Wu, Z. (2005). Micromixers - a review, *J. Micromech. Microeng.* **15**(2): R1–R16.

Patwardhan, S. R. and Deshpande, D. P. (1979). Extraction of vanillin from its aqueous solution by some organic solvents, *Petroleum and Chemical Industry Developments* **13**(10): 9–12.

Rebrov, E. V., Warnier, M. J. F., Muraza, O., de Croon, M. H. J. M., Hessel, V. and Schouten, J. C. (2007). Advanced catalytic microstructured reactor for continuous chemical synthesis integrated with a separation step, *Proc. AIChE Spring Meeting* p. 95b.

Roberge, D. M., Ducry, L., Bieler, N., Cretton, P. and Zimmermann, B. (2005). Microreactor technology: A revolution for the fine chemical and pharmaceutical industries?, *Chemical Engineering & Technology* **28**(3): 318–323.

Santiago, J. G., Wereley, S. T., Meinhart, C. D., Beebe, D. J. and Adrian, R. J. (1998). A particle image velocimetry system for microfluidics, *Experiments in Fluids* **25**(5): 316–319.

Sato, K., Hibara, A., Tokeshi, M., Hisamoto, H. and Kitamori, T. (2003a). Integration of chemical and biochemical analysis systems into a glass microchip, *Analytical Sciences* **19**(1): 15–22.

Sato, K., Hibara, A., Tokeshi, M., Hisamoto, H. and Kitamori, T. (2003b). Microchip-based chemical and biochemical analysis systems, *Advanced Drug Delivery Reviews* **55**(3): 379–391.

Schönfeld, F. and Hardt, S. (2004). Simulation of helical flows in microchannels, *AIChE Journal* **50**(4): 771–778.

Sengupta, S. (2006). Universality in the size and space of slugs generated by converging immiscible flows at microfluidic junctions, *AIChE annular metting* **San Francisco**.

Shoji, S. and Esashi, M. (1994). Microflow devices and systems, *J. Micromech. Microeng.* **4**(4): 157–171.

Shui, L., Eijkel, J. C. T. and van den Berg, A. (2007). Multiphase flow in microfluidic systems - control and applications of droplets and interfaces, *Advances in Colloid and Interface Science* **133**(1): 35–49.

Sinton, D. (2004). Microscale flow visualization, *Microfluidics and Nanofluidics* **1**(1): 2–21.

Slowinski, E. J., Gates, E. E. and Waring, C. E. (1957). The effect of pressure on the surface tension of liquids, *Journal of Physical Chemistry* **61**(6): 808–810.

Sousa, F. S., Portela, L. M., Kreutzer, M. T. and Kleijn, C. R. (2007). Numerical simulation of slug flows in square channels using a front-tracking/front/capturing method, *International Conference on Multiphase Flow* **ICMF07**: 505.

Stumm, W. and Morgan, J. J. (1995). *Aquatic Chemistry: Chemical Equilibria and Rates in Natural Waters; Third Edition.*

Tadepalli, S., Halder, R. and Lawal, A. (2007). Catalytic hydrogenation of o-nitroanisole in a microreactor: Reactor performance and kinetic studies, *Chemical Engineering Science* **62**(10): 2663–2678.

Tanthapanichakoon, W., Aoki, N., Matsuyama, K. and Mae, K. (2006). Design of mixing in microfluidic liquid slugs based on a new dimensionless number for precise reaction and mixing operations, *Chemical Engineering Science The John Bridgwater Symposium: Shaping the Future of Chemical Engineering* **61**(13): 4220–4232.

Taylor, G. I. (1961). Deposition of a viscous fluid on the wall of a tube, *J. Fluid Mech.* **10**: 161–165.

Teasdale, D., Milanovic, V., Chang, P. and Pister, K. S. J. (2001). *Microrockets for Smart Dust.*

Teh, S.-Y., Lin, R., Hung, L.-H. and Lee, A. P. (2008). Droplet microfluidics, *Lab on a Chip* **8**(2): 198–220.

Thulasidas, T. C., Abraham, M. A. and Cerro, R. L. (1997). Flow patterns in liquid slugs during bubble-train flow inside capillaries, *Chemical Engineering Science* **52**(17): 2947–2962.

Tice, J. D., Song, H., Lyon, A. D. and Ismagilov, R. F. (2003). Formation of droplets and mixing in multiphase microfluidics at low values of the reynolds and the capillary numbers, *Langmuir* **19**(22): 9127–9133.

Tokeshi, M. and Kitamori, T. (2005). Continuous flow chemical processing on a microchip using microunit operations and a multiphase flow network, *Progress in Nuclear Energy* **47**(1-4): 434–438.

Tokeshi, M., Minagawa, T. and Kitamori, T. (2000). Integration of a microextraction system on a glass chip: Ion-pair solvent extraction of fe(ii) with 4,7-diphenyl-1,10-phenanthrolinedisulfonic acid and tri-n-octylmethylammonium chloride, *Anal. Chem.* **72**(7): 1711–1714.

Tokeshi, M., Minagawa, T., Uchiyama, K., Hibara, A., Sato, K., Hisamoto, H. and Kitamori, T. (2002). Continuous-flow chemical processing on a microchip by combining microunit operations and a multiphase flow network, *Anal. Chem.* **74**(7): 1565–1571.

Trachsel, F. (2008). Design of a microreactor for reactions using supercritical fluids as the reaction solvent, *PhD thesis, no. 17'681* pp. http://e–collection.ethbib.ethz.ch.

Trachsel, F., Guenther, A., Khan, S. and Jensen, K. F. (2005). Measurement of residence time distribution in microfluidic systems, *Chemical Engineering Science* **60**(21): 5729–5737.

van Steijn, V., Kreutzer, M. T. and Kleijn, C. R. (2007). μ-PIV study of the formation of segmented flow in microfluidic T-junctions, *Chemical Engineering Science* **62**(24): 7505–7514.

Vankayala, B. K., Löb, P., Hessel, V., Menges, G., Hofmann, C., Metzke, D., Krtschil, U. and Kost, H.-J. (2007). Scale-up of process intensifying falling film microreactors to pilot production scale, *International Journal of Chemical Reactor Engineering* **5**: A91.

Waelchli, S. (2005). Two-phase flow characterization in gas-liquid microreactors, *PhD thesis, no. 16'116* pp. http://e–collection.ethbib.ethz.ch.

Waelchli, S. and Rudolf von Rohr, P. (2006). Two-phase flow characteristics in gas-liquid microreactors, *International Journal of Multiphase Flow* **32**(7): 791–806.

Wagner, W., Cooper, J. R., Dittmann, A., Kijima, J., Kretzschmar, H. J., Kruse, A., Mares, R., Oguchi, K., Sato, H., Stocker, I., Sifner, O., Takaishi, Y., Tanishita, I., Trubenbach, J. and Willkommen, T. (2000). The IAPWS Industrial Formulation 1997 for the Thermodynamic Properties of Water and Steam, *Journal of Engineering for Gas Turbines and Power* **122**(1): 150–184.

Wammes, W. J. A., Mechielsen, S. J. and Westerterp, K. R. (1990). The transition between trickle flow and pulse flow in a cocurrent gas–liquid trickle-bed reactor at elevated pressures, *Chemical Engineering Science* **45**(10): 3149–3158.

Wille, C., Gabski, H. P., Haller, T., Kim, H., Unverdorben, L. and Winter, R. (2004). Synthesis of pigments in a three-stage microreactor pilot plant - an experimental technical report, *Chemical Engineering Journal* **101**(1-3): 179–185.

Williams, C. B. and Yates, R. B. (1996). Analysis of a micro-electric generator for microsystems, *Sensors and Actuators A: Physical* **52**(1-3): 8–11.

Wong, H., Radke, C. and Morris, S. (1995). The motion of long bubbles in polygonal capillaries. part 1. thin films, *J. Fluid Mech.* **292**: 71–94.

Wu, R., McCready, M. J. and Varma, A. (1995). Influence of mass transfer coefficient fluctuation frequency on performance of three-phase packed-bed reactors, *Chemical Engineering Science* **50**(21): 3333–3344.

Xiao, H., Liang, D., Liu, G. C., Guo, M., Xing, W. L. and Cheng, J. (2006). Initial study of two-phase laminar flow extraction chip for sample preparation for gas chromatography, *Lab on a Chip* **6**(8): 1067–1072.

Xiong, R., Bai, M. and Chung, J. N. (2007). Formation of bubbles in a simple co-flowing micro-channel, *Journal of Micromechanics and Microengineering* **17**(5): 1002–1011.

Yawalkar, A. A., Sood, R., Kreutzer, M. T., Kapteijn, F. and Moulijn, J. A. (2005). Axial mixing in monolith reactors: Effect of channel size, *Ind. Eng. Chem. Res.* **44**(7): 2046–2057.

Yaws, C. L. (1999). Chemical properties handbook, *McGraw-Hill* p. http://www.knovel.com/knovel2/Toc.jsp?BookID=49&VerticalID=0 checked:June2008.

Yue, J., Chen, G., Yuan, Q., Luo, L. and Gonthier, Y. (2007). Hydrodynamics and mass transfer characteristics in gas-liquid flow through a rectangular microchannel, *Chemical Engineering Science* **62**(7): 2096–2108.

Zanfir, M., Gavriilidis, A., Wille, C. and Hessel, V. (2005). Carbon dioxide absorption in a falling film microstructured reactor: Experiments and modelling, *Ind. Eng. Chem. Res.* **44**(6): 1742–1751.

Zhang, X., Cooper, J. M., Monaghan, P. B. and Haswell, S. J. (2006). Continuous flow separation of particles within an asymmetric microfluidic device, *Lab Chip* **6**(4): 561–566.

Zheng, D. and Che, D. (2006). Experimental study on hydrodynamic characteristics of upward gas-liquid slug flow, *International Journal of Multiphase Flow* **32**(10-11): 1191–1218.

List of publications

Journal Publications

1. Fries, D. M., Wälchli, S. and Rudolf von Rohr, Ph. (2008): "Gas-liquid two-phase flow in meandering microchannels", *Chemical Engineering Journal*, Volume 135, Supplement 1, January 2008, 37 - 45.

2. Fries, D. M., Voitl, T. and Rudolf von Rohr, Ph. (2008): "Liquid Extraction of Vanillin in Rectangular Microreactors", *Chemical Engineering & Technologyy*, Volume 31, Issue 8, 1182 - 1187.

3. Fries, D. M. and Rudolf von Rohr, Ph. (2008): "Impact of inlet design on mass transfer in gas-liquid rectangular microchannels", *Microfluidics and Nanofluidics*, ***in press***

4. Fries, D. M., Trachsel, F. and Rudolf von Rohr, Ph. (2008): "Segmented Gas-Liquid Flow Characterization in rectangular Microchannels", *International Journal of Multiphase Flow*, ***in press***

Conference Contributions

1. Fries, D. M., Wälchli, S. and Rudolf von Rohr, Ph. (2006): "Gas-Liquid Two-Phase Flow in Meandering Microchannels", *9th International Conference on Microreaction Technology (IMRET 9)*, Potsdam.

2. Fries, D. M., Trachsel, F. and Rudolf von Rohr, Ph. (2006): "Druckeinfluss auf Gas-Flüssig Zweiphasenströmungen im Mikroreaktor", *GVC/DECHEMA Jahrestagungen 2006*, Wiesbaden.

3. Trachsel, F., Fries, D. M. and Rudolf von Rohr, Ph. (2006): "Charakterisierung der Verweilzeitverteilung in einem Festbettmikroreaktor", *GVC/DECHEMA Jahrestagungen 2006*, Wiesbaden.
4. Fries, D. M., Waelchli, S. and Rudolf von Rohr, Ph. (2006): "Gas-Liquid Flow Characteristics in Microreactors", *Annual Meeting of American Institute of Chemical Engineers (06AIChE)*, San Francisco.
5. Fries, D. M., Trachsel, F. and Rudolf von Rohr, Ph. (2007): "Optical characterization of phase distribution in gas-liquid Taylor flow in rectangular microfluidic channels", *7th International Conference on Multiphase Flow (ICMF 2007)*, Leipzig.
6. Fries, D. M. and Rudolf von Rohr, Ph. (2007): "Gas/Flüssig-Strömung in Mikroreaktoren: Einfluss des Designs auf Hydrodynamik und Mischlänge", *ProcessNet Jahrestagung 2007*, Aachen.
7. Fries, D. M., Voitl, T. and Rudolf von Rohr, Ph. (2008): "Using Microreactors for Liquid-Liquid Extraction of Vanillin" *10th International Conference on Microreaction Technology (IMRET 10)*, New Orleans.
8. Fries, D. M., Voitl, T. and Rudolf von Rohr, Ph. (2008): "Extraktion und Phasentrennung in Mikroreaktoren", *ProcessNet Jahrestagung 2008*, Karlsruhe.

Curriculum Vitae

Donata Maria Fries

Date of birth: March 10, 1981
Place of birth: Dresden, Germany
Citizen of: Germany (D)

09/1987 - 07/1992	Primary school, Meißen, Germany
08/1992 - 07/1999	Secondary school, Meißen, Germany academic degree: Abitur
10/1999 - 12/2004	Graduate studies in Process Engineering Dresden University of Technology, Germany academic degree: Dipl.-Ing.
04/2004 - 09/2004	Diploma thesis, Université Laval Québec, Canada ”Hydrodynamics of induced pulsing flow in trickle-bed-reactors at elevated temperatures and pressures”, advisors: Prof. Ruediger Lange and Prof. Faical Larachi
01/2005 - 07/2008	Doctoral student (PhD) and teaching assistant, Institute of Process Engineering, Swiss Federal Institute of Technology (ETH) Zürich, Switzerland, advisors: Prof. Philipp Rudolf von Rohr, Prof. Volker Hessel

Zürich, 2008